THE UNIVERSITY OF CHICAGO

QUANTIFYING HOW SPATIOTEMPORAL STIMULANT BIOPHYSICS IMPACT THE INNATE IMMUNE RESPONSE

A DISSERTATION SUBMITTED TO THE FACULTY OF THE DIVISION OF THE BIOLOGICAL SCIENCES AND THE PRITZKER SCHOOL OF MEDICINE IN CANDIDACY FOR THE DEGREE OF DOCTOR OF PHILOSOPHY

COMMITTEE ON IMMUNOLOGY

BY
ALEXANDER RYAN GALLUPPI

CHICAGO, ILLINOIS

AUGUST 2024

Copyright © 2024 Alexander Ryan Galluppi All rights reserved

TABLE OF CONTENTS

List of Tables	v
List of Figures	vi
Acknowledgements	viii
Abstract	ix
Chapter 1: Introduction	1
1.1: Overview of Innate Immunity	1
1.2: Macrophages	2
1.3: Pattern Recognition Receptors and Pathogen Associated Molecular Patterns	4
1.4: Biomechanics of Innate Immune Activation via Toll-Like Receptors	6
1.5: Toll-Like Receptor 2	9
1.6: Chemically Conjugated Pattern Recognition Receptor Agonists	10
1.7: Biophysics in Host Pathogen Interactions and Gram-Positive Bacteria	11
1.8: Lattice Light Sheet Microscopy	13
1.9: Fluidic Force Microscopy	15
1.10: References	
Chapter 2: Receptor-Ligand Kinetics Influence the Mechanism of Action of Linked TLR	
Agonists	24
2.1: Summary	24
2.2: Introduction	25
2.3: Materials and Methods	26
2.3.1: Synthetic Procedures	27
2.3.2: Biological Procedures	32
2.4: Results	34
2.4.1: Design and Synthesis of TLR Agonist Heterodimers	34
2.4.2: NF-κB Activity of TLR Dimers	
2.4.3: Comparing Cytokine Secretion Profiles of Linked and Unlinked Agonists	38
2.4.4: Effect of Dose on TNF-α Secretion Over Time	39
2.4.5: NF-κB Translocation Kinetics	42
2.5: Discussion	46
2.6: References	49
Chapter 3: Developing a Fluorescent TLR2 Labeling System to Investigate Receptor Dyna	mics
in Live Microscopy	52
3.1: Summary	52
3.2: Introduction	52
3.3: Materials and Methods	53
3.4: Results	56
3.5: Discussion	62
3.6. References	64

Chapter 4: Lattice Light Sheet Microscopy Reveals a Role of Biophysical Stimulant D	iversity on
Macrophage TLR2 Responses	67
4.1: Summary	67
4.2: Introduction	67
4.3: Materials and Methods	69
4.4: Results	76
4.4.1: Single Ligand Stimulation Causes a Speed Increase in TLR2 Tracks	76
4.4.2: Bacterial Stimulation Causes a Speed Decrease in TLR2 Tracks	78
4.4.3: TLR Speed Changes Due to Different Bacteria Cause Distinct Functiona	l Changes
in Macrophages	82
4.5: Discussion	84
4.6: References	86
Chapter 5: Investigating Key Physical Parameters During Bacterial Stimulation of Mad	crophages
Using Fluidic Force Microscopy	89
5.1: Summary	89
5.2: Introduction	89
5.3: Materials and Methods	90
5.4: Results	93
5.4.1: FluidFM Stimulation of Macrophages with B. Subtilis	93
5.4.2: More Than One B. Subtilis is Required to Activate Macrophages During	Short-
Term FluidFM Stimulation	94
5.4.3: Increased Approach Speed of Single B. Subtilis Does Not Improve Macr	ophage
Responses	95
5.4.4: Dynamic Tapping of Single B. Subtilis on the Macrophage Does No	ot Improve
Macrophage Responses	97
5.5: Discussion	98
5.6: References	100
Chapter 6: Conclusions & Future Directions	102
6.1: Research Summary	102
6.2: Multi-Molecule Ligands as a Therapeutic Frontier	102
6.3: Probing TLR Activation Through Microscopy	104
6.4: Biophysical Manipulation of Host-Pathogen Interactions	106
6.5: References	110
Appendix: Supplemental Data	112
A.2: Data Supporting Chapter 2	112
A.4: Data Supporting Chapter 4	116

LIST OF TABLES

Table A.4.1: List of tracked parameters for TLR2.	116
Table A.4.2: Comparison of track parameters for tracks touching B. subtilis and those that do)
not	121
Table A.4.3: Comparison of track parameters for tracks touching S. griseus and those that do) not
	121

LIST OF FIGURES

Figure 2.1: Comparing mechanism of NF-kB migration and subsequent immune response after						
activation with linked agonist and unlinked agonist mixture						
						RAW-Blue activation <i>via</i> NF-κB stimulation after 24 h incubation at 37°C37
						Figure 2.3: In vitro cytokine production from BMDC cells measured by cytokine bead array
assay39						
Figure 2.4 : Kinetic profiling of cytokine TNF-α secretion						
Figure 2.5 : Single-cell analysis NF-κB migration studies						
Figure 2.6 : Effect of dose on NF-κB migration						
Figure 3.1: Reducing SDS-PAGE gel for TLR2 Fab purification						
Figure 3.2 : Characterizing binding of AF647-TLR2 Fab58						
Figure 3.3: Assessing TLR2 function in the presence of TLR2 Fab fragment59						
Figure 3.4: LLSM imaging of TLR2 on RAW 264.7 macrophages						
Figure 4.1: Percentage changes in track metrics from resting after stimulating with LTA77						
Figure 4.2 : Percentage changes in track metrics from resting after stimulating with 0.1 OD <i>B</i> .						
subtilis79						
Figure 4.3 : Percentage changes in track metrics from resting after stimulating with 0.1 OD <i>S</i> .						
griseus81						
Figure 4.4: Effect of TLR2 physical changes on cytokine secretion in primary macrophages83						
Figure 5.1 : Representative FluidFM stimulation with <i>B. subtilis</i>						
Figure 5.2 : Multiple <i>B. subtilis</i> are required for efficient macrophage stimulation95						
Figure 5.3 : High <i>B. subtilis</i> approach speeds do not improve macrophage stimulation96						
Figure 5.4 : Tapping during initial <i>B. subtilis</i> contact does not impact macrophage response97						
Figure A.2.1 : Standard curve to quantify CPG dimers relative to FAM absorbance at 495 nm						
112						
Figure A.2.2 : Gel electrophoresis of FAM labeled CpG_1826, and FAM labeled Pam_PEG ₁₃						
_CpG compounds visualized by 6 fluorescein amidite tag (495 nm laser excitation)112						
Figure A.2.3 : Concentration scan of Pam2CSK4 (2/6), Pam3CSK4 (2/1), CpG_1826 (9) indole						
(4) and imidazoquinoline (7/8), corresponding equimolar mixtures and linked agonists measured						
by RAW-Blue activation after 24 h incubation at 37 °C						
Figure A.2.4: Intensity vs particle size of lipopeptide and lipopeptide derive dimers measured by						
dynamic light scattering (DLS)						
Figure A.2.5 : Box graph showing distribution of single cells based on the nuclear/cytoplasm						
NFκB ratio						
Figure A.4.1: Stimulation of RAW G9 macrophages on the LLSM						
Figure A.4.2: Full distribution of LTA resting vs. stimulated data						
Figure A.4.3 : Full distribution of <i>B. subtilis</i> resting vs. stimulated data						

Figure A.4.4 : Full distribution of <i>S</i> .	griseus resting vs	s. stimulated data	120
---	--------------------	--------------------	-----

ACKNOWLEDGMENTS

This work is not possible without the support of countless family, friends, colleagues, and mentors who have propped me up. To all those who have believed in me courageously and unflinchingly, know that you also gifted me the courage to believe in myself: thank you.

ABSTRACT

The innate immune system is the first line of defense against pathogens and immunological threats. By engaging a large cassette of pattern recognition receptors (PRRs) that recognize conserved molecular motifs on pathogens, the cells of the innate immune system can robustly respond to many classes of threats, activate specific innate and adaptive immune programs, and coordinate the nature of immune protection. While prior work has begun to show that the physical basis of receptor-ligand engagement is important for effective innate immune signaling, the quantitative impact of PRR biophysics on the innate immune response are still poorly understood and characterized. Herein, we use three diverse strategies to quantify different elements of receptor-ligand biophysics during innate immune stimulation. Firstly, we use chemically linked, multi-PRR agonists to understand how ligand organization impacts innate immune signal kinetics. Then, we develop a lattice light sheet microscopy method to label and track Toll-like receptor 2 on the surface of macrophages during activation by biophysically different stimuli to quantify receptor motion parameters associated with different responses. Finally, we use fluidic force microscopy to control presentation of single bacteria to macrophages to quantify what biophysical aspects of host cell-pathogen contact are most impactful on a single-cell exposure level. Through ordered ligand structuring and direct observations of immune cell stimulation, we show that information processing in the innate immune system is ligand- and dose-dependent and that individual cells can alter their functional state in response to the physical basis of their stimulation. These observations open the door for novel stimulant design that take advantage of physical structure and behavior to model immune interactions more faithfully or program immune responses in desired ways.

CHAPTER 1: INTRODUCTION

1.1 Overview of Innate Immunity

Innate immunity is the host's first line of defense against harmful foreign pathogens and substances. As part of an innate immune interaction, many complementary systems and cell types spread across tissues work together to mount a protective response. These systems range from providing barrier protection, cellular phagocytic responses, cytokine and chemokine signaling, and presentation of threats to downstream adaptive immune system programming. Several immune cells typically participate in the innate immune response: including granulocytes (e.g. neutrophils, eosinophils, basophils), mast cells, monocytes/macrophages, NK cells, and dendritic cells.

The two hallmarks of innate immunity are that the response is rapid and generic; that is, the response begins within minutes of exposure to a foreign threat¹ and is generic towards different broad classes of pathogens or danger. After exposure, the body's innate immune sentinel cells initiate this generic response via signaling through pattern recognition receptors (PRRs), which recognize molecular motifs that are broadly conserved by different types of pathogens and/or that are indicative of cellular damage. The pathogen/damage-associated molecular patterns (P/DAMPs) that are present on a pathogen or in the environment dictate which PRRs become activated and what types of downstream responses are initiated.

To clear pathogenic infections, several acute inflammatory functions of innate immune cells are engaged post-PRR ligation. Cells resident to the infected tissue first secrete inflammatory mediators including chemokines, cytokines, eicosanoids, and vasoactive amines to attract leukocytes to the site of infection and to increase these cells' access from blood vessels to

the extravascular tissue². Upon arrival, these leukocytes attack pathogens via phagocytosis, release of toxic granules, and secretion of additional signal molecules.

After the inflammatory response, there is a coordinated and active resolution phase to avoid chronic and undue inflammatory damage to the host. This process involves synthesis of mediators that signal for cytokine depletion, lymphocyte apoptosis and clearance, and cellular reprogramming to reach immune homeostasis again^{3,4}. Failure to resolve innate immune inflammation can lead to or worsen a variety of chronic inflammatory disease states including rheumatoid arthritis, neurodegenerative disease, and type 2 diabetes, among others⁵.

Finally, innate immune cells play an important role in initiating downstream adaptive immune responses where relevant. As part of PRR signaling, dendritic cells and macrophages uptake pathogens and pathogen peptides and process them to present antigenic peptides and secondary signals to naïve adaptive immune cells to begin activation and expansion of these cells⁶. Cytokine secretion from the presenting cells also helps differentiate adaptive cells into functional phenotypes that are appropriate to the infection context⁷.

1.2 Macrophages

Macrophages are a type of phagocytic leukocyte found in all mammalian tissues. Briefly, their lineage arises in three waves of hematopoiesis. The first two are derived from erythromyeloid progenitors in the yolk sac during embryogenesis. These early macrophages seed and colonize the brain and fetal liver during development, and the latter become monocyte precursors that infiltrate developing tissue to become tissue-resident macrophages that are maintained during adult life through local proliferation. The third wave of development comes from fetal hematopoietic stem cells that give rise to some fetal and neonatal monocytes, although

this contribution to the developing monocyte/macrophage landscape is smaller than those of the first two waves⁸. After birth, hematopoietic stem cells from the bone marrow (and to a lesser extent in the spleen⁹) continue to differentiate into monocytes that enter circulation and can further differentiate into macrophages when recruited to inflammatory tissues.

In broad functional terms, tissue resident macrophages are involved in homeostasis of the tissue microenvironment and immune surveillance in their respective tissues. Precise roles and signals are tissue- and niche-dependent, but resident macrophage control and activation can be driven by multiple signal mediators—including M-CSF, TGF-β, glucocorticoids, and interleukins (e.g. IL-4, IL-13)—as well as by infection signals through PRRs and the like. Some of their roles include waste removal, regulation of metabolism, directing remodeling of bone and vasculature, wound repair, and resolution of inflammation 10, 11.

In addition to tissue-resident macrophages, circulating monocytes can also migrate to tissues to become macrophages in a context-dependent manner. In mice, circulating monocyte subsets are distinguished by Ly6C^{hi} and Ly6C^{lo} expression and differentiate into Ly6C^{hi} and Ly6C^{lo} macrophages, although phenoconversion of Ly6C^{hi} macrophages to Ly6C^{lo} macrophages is also an important source of the latter¹². Ly6C^{hi} monocytes migrate out of the bone marrow in a CC-chemokine receptor 2 (CCR2)-dependent manner and are recruited to inflamed tissues through expression of adhesion molecules such as L-selectin and CD34¹³. These cells are generally associated with antimicrobial phenotypes such as phagocytosis and pro-inflammatory signaling consistent with their recruitment by acute inflammatory environments. By contrast, the Ly6C^{lo} macrophages are characterized by expression of CX3C motif chemokine receptor 1 (CX3CR1) and are associated with anti-inflammatory, sentinel phenotypes more akin to tissue-resident cells. Human analogues to these macrophage subsets, while not precisely overlapping,

are generally characterized as "classical" macrophages (CD14⁺⁺CD16⁻CCR2^{hi}CX3CR1^{lo}) and "intermediate/non-classical" macrophages (CD14⁺⁺CD16⁺CX3CR1^{hi}CCR2^{lo}/CD14⁺CD16⁺⁺CX3CR1^{hi}CCR2^{lo}).

One of the most common *in vitro* models of mouse macrophages is the RAW 264.7 immortalized cell line, which is a monocyte/macrophage cell line derived from BALB/c mice. The cells express most PRRs and inflammatory machinery that primary macrophages have (notably absent is the apoptosis-associated speck-like protein containing a CARD domain (ASC) component of the inflammasome), and they exhibit macrophage-like function towards pathogens and other stimulus—including activation, phagocytosis, pinocytosis, and differentiation into other subsets (e.g. osteoclasts)¹⁴. It is also possible to grow primary macrophages for functional analysis by collecting mouse bone marrow and culturing the marrow cells with macrophage colony stimulating factor (M-CSF) as a stimulus for the bone marrow progenitors to differentiate into macrophages. Such cells are termed "bone marrow derived macrophages" (BMDMs).

1.3 Pattern Recognition Receptors and Pathogen Associated Molecular Patterns

Innate immune cells have five different classes of PRRs that help them sense a variety of PAMPs and DAMPs that work in consort to effect an immune response. These classes include Toll-like receptors, NOD-like receptors, RIG-I-like receptors, C-type lectin receptors, and AIM2-like receptors. PRRs can be membrane bound on the cell surface or in endosomal compartments, or they can be found in the cell cytoplasm—the localization of the receptors being directly tied to their function.

Toll-like receptors (TLRs) are perhaps the best characterized of the PRRs. Humans possess 10 TLRs that are membrane-bound on the cell surface or in endosomal compartments.

The repertoire of human TLRs is responsive to a wide variety of bacterial, viral, fungal, and protozoan epitopes—including lipopolysaccharides, di- and tri-acylated lipoproteins, mannans, and genetic material—as well as some host-derived danger signals such as heat shock proteins and fibrinogen¹⁵.

NOD-like receptors (NLRs) are cytoplasmic receptors that have common C-terminal leucine rich repeats and central nucleotide binding domains that respond to a wide variety of PAMPs such as microbial toxins and bacterial cell wall components. They can be further subclassified by N-terminal differences: notably, NLRCs with caspase recruitment domains and NLRPs with pyrin recruitment domains. Certain NOD-like receptors (e.g. NLRP1, NLRP3, NLRC4) have achieved prominence for their ability to form inflammasomes: structures that, upon PRR ligation, are recruited to the NLR to form an active caspase-1 complex that cleaves pro-IL-1β and pro-IL-18 into their active forms. These cytokines have wide-ranging, potent pro-inflammatory effects in the innate and adaptive immune landscapes 16.

RIG-I-like receptors (RLRs) are a family of three RNA sensing receptors located in the cytosol which are primary responsible for viral sensing. Upon ligation of RNA bearing 5' di- or triphosphate groups to the receptor, a signal cascade is initiated which terminates in interferon regulatory factor (IRF) 3, IRF7, and nuclear factor- κ B (NF- κ B)-mediated upregulation of type I interferons such as interferon α (IFN α) and IFN β^{17} . These effectors in turn stimulate interferon stimulated genes (ISGs) which exert many important antiviral effects—such as restriction of the viral life cycle and promotion of adaptive cell responses.

C-type lectin receptors (CLRs) are a very large, heterogeneous family of receptors that bind carbohydrates via a C-type lectin-like domain. CLRs are found in both membrane bound and cytoplasmic compartments and have many immune and non-immune functions. Some of

prominent CLRs with innate immune PRR activity include Dectin-1 and Dectin-2, DC-SIGN, macrophage mannose receptor, and DEC-205. These receptors are present on a variety of myeloid cells and have been implicated in the fungal response, for promoting cell adhesion and migration towards inflammatory sites, and trained immunity.

Finally, AIM2-like receptors (ALRs) are a recently classified subset of PRRs that participate in intracellular DNA sensing 18 . There are currently two known ALRs: AIM2, which promotes inflammasome formation by interacting with ASC upon ligation to DNA, and IFI16, which not only promotes inflammasome formation but is also cited to induce interferon γ production via the STING pathway. IFI16 has been subject to much recent study for its role in antiviral defenses as well and for its localization in both the cytoplasm and nucleus in some cells 19 .

1.4 Biomechanics of Innate Immune Activation via Toll-Like Receptors

All TLRs have a cytoplasmic Toll/interleukin-1-receptor (TIR) domain from which signaling initiates. Ligation of PAMPs induces TLR dimerization which brings two TIR domains together. These dimers can be homodimers (e.g. TLR4, TLR5, TLR9) or heterodimers (e.g. TLR2/6, TLR2/1, TLR7/8). Molecular machinery then assembles to the dimerized TIR domains to form a supramolecular organizing center (SMOC) and effect signaling. Most TLRs use the so-called "Myddosome" for signaling—with the exception of TLR3, which uses the "Triffosome," and TLR4, which can use both.

Myddosome formation begins with the recruitment of MyD88-adaptor-like (MAL) protein through paired interaction of TIR domains on the TLRs and MAL. MyD88 is then recruited to the MAL scaffold through additional TIR-TIR interactions, although some evidence

suggests that in certain circumstances MAL is not required for TLR signaling²⁰. X-ray crystallography has revealed that 6-8 MyD88 molecules are recruited to the signaling unit through their C-terminal TIR domains. MyD88 also contains N-terminal Death domains (DD) that are critical for sequential oligomerization of the rest of the Myddosome: four IRAK4 molecules first engage in DD-DD interactions with the assembled MyD88 molecules, then four IRAK2 molecules are recruited—again by DD-DD interactions—to form a helical Myddosome structure. Importantly, IRAK4 and IRAK2 are monomers in solution until exposed to oligomeric MyD88 and the MyD88:IRAK4 complex respectively, highlighting the importance of oligomerization and organized, sequential recruitment of the Myddosome structure for effective signalling²¹. The tight packing of the IRAK components of the Myddosome activates autophosphorylation activity the drives recruitment of Tumor necrosis factor receptor-associated factor 6 (TRAF6), which in turn finally stimulates the transforming growth factor β-activated kinase 1 (TAK1)-dependent pathway for NF-κB-, activator protein-1- (AP-1), and IRF3-dependent immune gene transcription.

Concerning the canonical view of the Myddosome, recent super-resolution microscopic and proteomic evidence from the Kagan group has suggested that the previously crystalized Myddosome structures molecules may actually be "proto-Myddosomes" that dissociate from plasma membrane TLRs and that larger Myddosome assembly occurs primarily in the cytosol⁵⁸. Kagan et al found that the earliest stage of TLR signaling after PAMP signaling includes proto-Myddosome formation at the TIR domain which dissociate after roughly 30 minutes before giving rise to much larger, long-lived, TLR-free Myddosome clusters in the cytosol. They also suggest that these large Myddosomes are primary scaffolds for the entire signaling TLR

pathway—as biochemical analysis showed effector proteins in pathways typically thought of as downstream of MyD88 associating with the Myddosome over several hours.

The Triffosome is an analogous signalosome used by TLR3 and endosomal TLR4 which differs from the Myddosome in scaffolding components. In TLR4 signaling, TRIF-related adaptor molecule (TRAM) serves a similar function to MAL in initiating signalosome formation at the TIR domains of TLR4. The TRAM adaptor does not seem to interact with TLR3, and the precise mechanism for TLR3-mediated Triffosome activation is unknown²⁰. TRIF binds to TRAM and recruits TRAF6 and TRAF3 to activate kinase activity for downstream immune signaling. A role for IRAK4, IRAK2, and IRAK1 in Triffosome formation has also been implicated, but their structure and necessity are less well understood than in the Myddosome²³. One key difference in the two signalosomes is the ability for the Triffosome to promote higher levels of IRF3-mediated IFN responses through TANK-binding kinase 1 (TBK1) than the Myddosome can. This may be due to a pLxIS motif on TRIF that interacts with IRF3 when phosphorylated²⁰.

TLR clustering has also been hypothesized as an important part of the biomechanics of their function. Research on TLR4 structure suggests that TIR-engaged MAL dimers can crosslink MyD88s across different Myddosomes, thereby tethering together multiple TLR4 dimers by their cytoplasmic tails²³. This mechanism may help provide signal amplification—especially with reduced TLR or ligand concentrations where it is helpful to integrate individual receptor signals as much as possible. It has also been hypothesized that regulation of the actin cytoskeleton provides support for TLR clustering and organization by altering membrane-embedded receptor mobility²⁴. Increased receptor mobility is presumably linked to higher

surveillance of the environment and more interactions between individual receptors to enhance cooperative signaling.

1.5 Toll-Like Receptor 2

TLR2 is a type-I transmembrane PRR that is ubiquitously expressed on lymphocytes as well as on endothelial and epithelial cells. Its molecular weight is approximately 95 kDa, and its undimerized dimensions are roughly 70Å by 70Å by 25Å²⁵. The repertoire of PAMPs and DAMPs TLR2 recognizes is vast²⁶, and it senses these ligands generally in heterodimeric structures with TLR1 or TLR6. Some oft cited examples include diacylated lipoproteins (TLR2/6), triacylated lipoproteins (TLR2/1), bacterial cell wall components (e.g. lipoteichoic acid (LTA, TLR2/6)), and many other proteins and polysaccharides associated with bacteria, viruses, fungi, and parasites. TLR2 ligand loading is also assisted by a variety of co-receptors depending on the ligand—commonly (but not exclusively) CD14 and/or CD36.

Ligation of TLR2 ligands engages the MyD88 signaling cascade described in section 1.4. The result in immune cells is transcription of NF-κB- and AP-1-related gene programs and is largely dependent on the type of ligands and biological niches involved. Notably, although TLR2 is canonically thought of as a cell surface receptor that stimulates pro-inflammatory responses, there is evidence that it participates in endocytosis of certain ligands in a clathrindependent manner and that endosomal signaling from TLR2 induces immune programs not usually associated with NF-κB- and AP-1 such as type I IFN signaling^{27,28}.

1.6 Chemically Conjugated Pattern Recognition Receptor Agonists

It has been previously shown that activating multiple PRRs during stimulation can cause combinatorial, synergistic, or antagonistic activation and modulation of downstream immune responses^{29,30,31}. Indeed, it has been hypothesized that naturally occurring multi-PAMP exposure from pathogens augments adaptive immune protection relative to vaccination³². It is of considerable interest, therefore, to combine different PAMPs into structures that integrate their signals. Two relevant examples of how to achieve this include chemically conjugating PAMPs together using linear linkers and tethering PAMPs to a core structure such as a microparticle.

One strategy for conjugating PAMPs to a chemical linker (e.g. a polyethylene glycol (PEG) linker) is to derive and synthesize PAMPs that include attached orthogonal groups that react with the PEG linker. A major advantage to synthesizing a linked agonist is precise control over the spatial arrangement of the combined signal: most prior work on PRR agonist synergies had focused on free mixtures of the stimulant PAMPs, which often does not faithfully mimic the biology of multi-PRR stimulation due to pathogen exposure, where the PAMPs are tethered to the pathogen and thus localize to the same area of the cell. A linear linker provides a specific and easily tunable distance between the stimulants to study how this distance may impact the integration of the total signal by a responding cell.

In considering that pathogens consist of many PRR agonists linked together by the core structure of the pathogen itself, a similar synthetic approach—e.g. with a microparticle—is another way to introduce multiple, structured PRR signals to immune cells for stimulation that may better mimic biological contexts. While this approach may offer somewhat less control of the spatial arrangement of the ligands themselves compared to a linear linker with a single point of attachment for each ligand, it is also much more adaptable—able to accommodate multiple

different ligand types on the same particle and offering more structural shapes and arrangements. Strategies between these two exist as well—for example, using a triazine molecule as a core with three attachment points for ligands. Prior work has shown that triazine cores conjugated with TLR2/6, TLR4, and TLR7 agonists in different combinations substantially alter cytokine secretion and adaptive immune cell programming relative to unlinked agonist mixtures and to each other³², emphasizing a role for structured stimulation for modulating immune responses.

1.7 Biophysics in Host-Pathogen Interactions and Gram-Positive Bacteria

The field of host-pathogen interactions is broadly concerned with how pathogens interact with an infected host from the time of entry to clearance or pathogen survival. On a host molecular level, the infection process offers numerous ways for a pathogen to interface with the host immune system to provoke or antagonize protective responses. Much of this interaction is a tug-of-war of sorts between the host system's desire for pathogen clearance versus the pathogen's desire for infectivity and immune evasion. As an example, several bacterial toxins are known to disrupt cellular immune functions to evade detection—e.g. by disturbing kinase activity in TLR pathways or halting NF-κB migration to the nucleus³³. At the same time, it has also been shown that such modifications can sometimes be activators of PRRs in their own right—e.g. NLR activation due to RhoGTPase modification, and it has been hypothesized that such activation might even lead to innate immune training³⁴. Evidently, the interplay between the host immune system and pathogens is very complex, and it is crucial to understand the mechanisms of interaction between host immune cells and pathogens to fully comprehend immune protection.

It has also been shown that the biophysical parameters underlying host-pathogen interactions influence immune activity. For example, since many functions of infectivity and innate immune detection rely on physical contact of a host cell and a pathogen—e.g. for receptor ligation or endocytosis—pathogen motility is an important determinant of how infection and clearance proceeds. Indeed, active matter modeling and microscopy have shown that *in vitro* estimations of infectivity depend on the search time it takes for a motile bacterium to reach a host cell, which is dependent on the diffusivity of the bacterium³⁵. While these experiments are lacking potential contextual drivers of infectivity *in vivo*, bacteria in these experiments do not exhibit biased movement toward host cells compared to their movement in the absence of a target, thus emphasizing the importance of the bacterial dynamics when considering host-pathogen interactions. Recent efforts have also been made to improve motility assaying in bacteria-host interactions to better simulate host conditions, including context simulation with soft agar, transcriptomic approaches linking gene expression to function, and using real-time light sheet microscopy to image host-pathogen dynamics in live zebrafish³⁶.

Gram-positive bacteria are a very broad class of bacteria of many different shapes, sizes, and biophysical characteristic that participate in host-pathogen interactions. The bacteria are named for their ability to retain the eponymous Gram stain owing to their thick peptidoglycan outer layer. This peptidoglycan layer also makes Gram-positive bacteria exciting model organisms with which to study PRR dynamics during host-pathogen interactions, as several PRRs participate in peptidoglycan sensing and in sensing of lipoproteins embedded in the bacterial cell wall. Lipoteichoic acid (LTA) in particular is an important agonist of TLR2 found exclusively in Gram-positive bacteria whose immunostimulatory capacities have been extensively studied^{37,38,39}. Prior work has also suggested TLR2 organizes into clustered

structures upon interaction with LTA to promote downstream internalization and trafficking of the activated receptor complex⁴⁰, again highlighting a role for spatial information processing during PRR responses.

1.8 Lattice Light Sheet Micropscopy

Traditional light sheet microscopy (LSM) is characterized by the use of a plane of excitatory light to image a thin slice of a fluorescent sample. Fluorescence emissions are collected perpendicularly to this plane of light, thus allowing for the fluorescence signal from the whole xy-imaging plane to be detected at once. It is also possible to collect three-dimensional images of the sample by scanning the sample or light sheet through the z-imaging plane. There are several advantages to LSM over more conventional fluorescence microscopy approaches: firstly, it generates very low out-of-focus signal owing to the selective illumination in the optical plane—as opposed to beam-based methods that illuminate more of the sample above and below the focal plane. This selectivity leads to high-quality optical sectioning and 3D image reconstruction. The lower total illumination also causes three to five orders of magnitude lower sample irradiation, inducing much less phototoxicity and photobleaching than in confocal microscopy, where optical sectioning is derived from filtering out-of-focus fluorescent emissions before they reach the detector⁴¹. Finally, LSM is considerably faster than other techniques with similar resolution and optical sectioning: image acquisition has been cited as at least ten times faster than fast confocal microscopy⁴². The speed—along with reduced phototoxicity—makes LSM especially suited for live microscopy contexts where samples can move at a fast rate, e.g. receptor imaging, and associated tracking applications. Selected examples of LSM imaging in recent years include 3D imaging of cleared whole mouse brain⁴², tracking of messenger

ribonucleoprotein particles in nuclei of *Chironomus tentans* larval cells⁴³, and imaging of tumor vascularization, CAR T cell infiltration, and immune cell composition⁴⁴.

Several methods in recent years have modified and improved upon the weaknesses of LSM. In the first modern iteration of LSM—selective plane illumination microscopy (SPIM)—the light sheet was generated as a static sheet with a cylindrical lens⁴⁵. While this technique first provided the optical sectioning and reduced photodamage required to image live fruit fly embryogenesis, the use of a cylindrical lens to form a static plane can cause refraction aberrations and exaggerated scattering in many optically dense biological contexts. Relatedly, the xy-distance through which the light sheet provides near uniform illumination is correlated with its thickness, which limits the axial (z) resolution of the image. Researchers have overcome this limitation by introducing scanning action to LSM: by scanning a beam through the xy-axis to create a virtual "light sheet," they can achieve more precisely intensity-controlled illumination that can be mobilized from different directions to increase lateral (xy) resolution and which is subject to fewer focusing aberrations—although this technique does sacrifice some speed and photodamage mitigation⁴⁶.

Researchers have also made efforts to improve the resolution of LSM. Typical SPIM lateral resolutions are no better than a standard widefield microscope (i.e. about 200nm in highly optimized cases) and axial resolution depends greatly on the size of the light sheet (~6µm in Huisken et al's 2004 paper introducing the technique⁴⁵). In general, to achieve an appropriately large field of view while maintaining high optical sectioning capability, a sufficiently thin light sheet must be projected over a wide area⁴⁷. Traditionally Gaussian shaped beams are limited in their ability to produce long (i.e. high field of view) light sheets while maintaining sub-micron thinness, so alternative, non-Gaussian beam shapes have been proposed to optimize field of view

and thinness. Among the most popular solution to this problem is the non-diffractive Bessel beam, which, when scanned, can maintain a thin light sheet owing to its narrow beam shape while projecting over a large area due to its non-diffractive properties.

Bessel beams, however, offer their own challenges in light sheet generation due to their shape: in a Bessel beam, concentric lobes of lower intensity light radiate out from the central beam. Because of this, when scanning a single Bessel beam, additional, off focus light sheets are created in addition to a thin central sheet. Lattice light sheet microscopy (LLSM) is a technique developed by a team led by Eric Betzig in 2014 to address this issue⁴⁸. Lattice light sheet microscopy uses a 2D array of Bessel beams in which the concentric side lobes of each beam destructively interfere with each other, reducing the total intensity of the array to that of the central Bessel beams. When dithered, this makes a light sheet that is very tightly confined to the focal plane without sacrificing field of view. Depending on the geometry of the lattice pattern, the resolution of LLSM can reach as low as 230nm lateral resolution and 370nm axial resolution⁴⁸.

1.9 Fluidic Force Micropscopy

Fluidic Force Microscopy (FluidFM) is a technique that combines atomic force microscopy (AFM) with a micropipette-cantilever assembly. The result is a microscope that can visualize cells whilst being able to approach, touch, and manipulate cells and dispense femtoliter volumes of liquids at the same time with the force sensing and liquid handling features of the cantilever⁴⁹. The FluidFM is a powerful and versatile tool for assaying nanoscale single-cell dynamics, performing biophysical manipulation of cells, and precisely delivering a variety of biomolecules to cells.

The basic operating principles of the FluidFM's AFM component are similar to those of traditional AFMs. Briefly, the cantilever is connected to a piezoelectric driver that controls the vertical movement of the probe. A laser beam is pointed towards the reflective cantilever tip, and the laser is deflected towards a position sensitive detector. As the cantilever is scanned through a sample and touches an object, it will bend, resulting in laser displacement that is read by the position sensitive detector. The position sensor converts these deflections into topographical information by relaying feedback to the piezoelectric element to move up and down to minimize deflection⁵⁰. AFM has broad applications in biomechanical sensing: selected recent examples include assaying changes in stiffness in tumor cells during metastasis⁵¹, performing topographical imaging of CD8+ T cell/perforin-mediated pore formation⁵², and measuring PRR/PAMP interaction kinetics in a single-molecule fashion⁵³.

FluidFM takes this concept one step further by adding a microchannel to the AFM cantilever. The microchannel is connected to a pressure-controlled pump that allows precision control of positive and negative pressure at the tip of the cantilever and for liquid handling through the probe. This pressure control heightens the FluidFM's ability to perform detailed manipulations of its environment over a standard AFM. For example, the FluidFM can apply negative pressure to pick up cells, bacteria, microparticles, and other objects larger than the channel, hold pressure to carry them to a different location, then release pressure to set them down. This allows the user to, for example, arrange environments to probe cell-cell interactions using the AFM functions of the instrument. Additionally, while it is possible to functionalize an AFM probe with small molecules⁵⁴, the liquid handling makes it significantly more straightforward to dose a single cell with a small number of biomolecules by moving the probe directly above a cell and dispensing them locally. Finally, the FluidFM is capable of puncturing

cells with certain shapes of cantilever tip: this function combined with liquid handling means it is possible to inject biomolecules directly into cells and to extract cellular contents from inside cells on a single-cell basis.

FluidFM techniques such as these have been used in a variety of novel investigations. Selected recent examples include using robotic enabled FluidFM to probe how the distribution of single-cell adhesion proteins changes during the cell cycle⁵⁵, direct injection of *Salmonella* bacteria into intestinal epithelial cells to study inflammasome activation and host-pathogen interactions in the cytoplasm of these cells while bypassing surface PRR engagement⁵⁶, and the dispensing of PRR ligands directly to macrophages with a fluorescent NF-κB reporters to probe how macrophage activation through PRRs depends on the local density of other macrophages within the signaling environment and indicating a role for cell-cell communication during macrophage activation⁵⁷.

1.10 References

- 1. Aristizábal B, González Á. Innate immune system. In: Anaya JM, Shoenfeld Y, Rojas-Villarraga A, et al., editors. Autoimmunity: From Bench to Bedside [Internet]. Bogota (Colombia): El Rosario University Press; 2013 Jul 18. Chapter 2.
- 2. Medzhitov, R. Origin and physiological roles of inflammation. *Nature* **454**, 428–435 (2008). https://doi.org/10.1038/nature07201
- 3. Ortega-Gómez, A., Perretti, M., & Soehnlein, O. (2013). Resolution of inflammation: an integrated view. *EMBOmolecular medicine*, *5*(5), 661–674. https://doi.org/10.1002/emmm.201202382
- 4. Serhan, C. N., & Savill, J. (2005). Resolution of inflammation: the beginning programs the end. *Nature immunology*, 6(12), 1191–1197. https://doi.org/10.1038/ni1276
- 5. Panigrahy, D., Gilligan, M. M., Serhan, C. N., & Kashfi, K. (2021). Resolution of inflammation: An organizing principle in biology and medicine. *Pharmacology & therapeutics*, 227, 107879. https://doi.org/10.1016/j.pharmthera.2021.107879
- 6. Janeway CA Jr, Travers P, Walport M, et al. Immunobiology: The Immune System in Health and Disease. 5th edition. New York: Garland Science; 2001.
- 7. Jain, A., & Pasare, C. (2017). Innate Control of Adaptive Immunity: Beyond the Three-Signal Paradigm. *Journal of immunology (Baltimore, Md. : 1950), 198*(10), 3791–3800. https://doi.org/10.4049/jimmunol.1602000
- 8. Hoeffel, G., & Ginhoux, F. (2018). Fetal monocytes and the origins of tissue-resident macrophages. *Cellular immunology*, *330*, 5–15. https://doi.org/10.1016/j.cellimm.2018.01.001
- 9. Pittet, M. J., Nahrendorf, M., & Swirski, F. K. (2014). The journey from stem cell to macrophage. *Annals of the New York Academy of Sciences*, *1319*(1), 1–18. https://doi.org/10.1111/nyas.12393
- 10. Davies, L. C., Jenkins, S. J., Allen, J. E., & Taylor, P. R. (2013). Tissue-resident macrophages. *Nature immunology*, *14*(10), 986–995. https://doi.org/10.1038/ni.2705
- 11. Zhao, J., Andreev, I., & Silva, H. M. (2024). Resident tissue macrophages: Key coordinators of tissue homeostasis beyond immunity. *Science immunology*, *9*(94), eadd1967. https://doi.org/10.1126/sciimmunol.add1967
- 12. Li, Y. H., Zhang, Y., Pan, G., Xiang, L. X., Luo, D. C., & Shao, J. Z. (2022). Occurrences and Functions of Ly6C^{hi} and Ly6C^{lo} Macrophages in Health and Disease. *Frontiers in immunology*, *13*, 901672. https://doi.org/10.3389/fimmu.2022.901672

- 13. Geissmann, F., Jung, S., & Littman, D. R. (2003). Blood monocytes consist of two principal subsets with distinct migratory properties. *Immunity*, *19*(1), 71–82. https://doi.org/10.1016/s1074-7613(03)00174-2
- 14. Taciak, B., Białasek, M., Braniewska, A., Sas, Z., Sawicka, P., Kiraga, Ł., Rygiel, T., & Król, M. (2018). Evaluation of phenotypic and functional stability of RAW 264.7 cell line through serial passages. *PloS one*, *13*(6), e0198943. https://doi.org/10.1371/journal.pone.0198943
- 15. Sameer, A. S., & Nissar, S. (2021). Toll-Like Receptors (TLRs): Structure, Functions, Signaling, and Role of Their Polymorphisms in Colorectal Cancer Susceptibility. *BioMed research international*, 2021, 1157023. https://doi.org/10.1155/2021/1157023
- 16. Platnich, J. M., & Muruve, D. A. (2019). NOD-like receptors and inflammasomes: A review of their canonical and non-canonical signaling pathways. *Archives of biochemistry and biophysics*, 670, 4–14. https://doi.org/10.1016/j.abb.2019.02.008
- 17. Rehwinkel, J., & Gack, M. U. (2020). RIG-I-like receptors: their regulation and roles in RNA sensing. *Nature reviews. Immunology*, 20(9), 537–551. https://doi.org/10.1038/s41577-020-0288-3
- 18. Caneparo, V., Landolfo, S., Gariglio, M., & De Andrea, M. (2018). The Absent in Melanoma 2-Like Receptor IFN-Inducible Protein 16 as an Inflammasome Regulator in Systemic Lupus Erythematosus: The Dark Side of Sensing Microbes. *Frontiers in immunology*, *9*, 1180. https://doi.org/10.3389/fimmu.2018.01180
- 19. Brubaker, S. W., Bonham, K. S., Zanoni, I., & Kagan, J. C. (2015). Innate immune pattern recognition: a cell biological perspective. *Annual review of immunology*, *33*, 257–290. https://doi.org/10.1146/annurev-immunol-032414-112240
- 20. Fitzgerald, K. A., & Kagan, J. C. (2020). Toll-like Receptors and the Control of Immunity. *Cell*, *180*(6), 1044–1066. https://doi.org/10.1016/j.cell.2020.02.041
- 21. Lin, S. C., Lo, Y. C., & Wu, H. (2010). Helical assembly in the MyD88-IRAK4-IRAK2 complex in TLR/IL-1R signalling. *Nature*, *465*(7300), 885–890. https://doi.org/10.1038/nature09121
- 22. Pereira, M., & Gazzinelli, R. T. (2023). Regulation of innate immune signaling by IRAK proteins. *Frontiers in immunology*, *14*, 1133354. https://doi.org/10.3389/fimmu.2023.1133354
- 23. Guven-Maiorov, E., Keskin, O., Gursoy, A., VanWaes, C., Chen, Z., Tsai, C. J., & Nussinov, R. (2015). The Architecture of the TIR Domain Signalosome in the Toll-like Receptor-4 Signaling Pathway. *Scientific reports*, *5*, 13128. https://doi.org/10.1038/srep13128
- 24. Li, M., & Yu, Y. (2021). Innate immune receptor clustering and its role in immune regulation. *Journal of cell science*, *134*(4), jcs249318. https://doi.org/10.1242/jcs.249318

- 25. Su, L., Wang, Y., Wang, J., Mifune, Y., Morin, M. D., Jones, B. T., Moresco, E. M. Y., Boger, D. L., Beutler, B., & Zhang, H. (2019). Structural Basis of TLR2/TLR1 Activation by the Synthetic Agonist Diprovocim. *Journal of medicinal chemistry*, 62(6), 2938–2949. https://doi.org/10.1021/acs.jmedchem.8b01583
- 26. Oliveira-Nascimento, L., Massari, P., & Wetzler, L. M. (2012). The Role of TLR2 in Infection and Immunity. *Frontiers in immunology*, *3*, 79. https://doi.org/10.3389/fimmu.2012.00079
- 27. Stack, J., Doyle, S. L., Connolly, D. J., Reinert, L. S., O'Keeffe, K. M., McLoughlin, R. M., Paludan, S. R., & Bowie, A. G. (2014). TRAM is required for TLR2 endosomal signaling to type I IFN induction. *Journal of immunology (Baltimore, Md. : 1950)*, *193*(12), 6090–6102. https://doi.org/10.4049/jimmunol.1401605
- 28. Maler, M. D., Zwick, S., Kallfass, C., Engelhard, P., Shi, H., Hellig, L., Zhengyang, P., Hardt, A., Zissel, G., Ruzsics, Z., Jahnen-Dechent, W., Martin, S. F., Nielsen, P. J., Stolz, D., Lopatecka, J., Bastyans, S., Beutler, B., Schamel, W. W., Fejer, G., & Freudenberg, M. A. (2024). Type I Interferon, Induced by Adenovirus or Adenoviral Vector Infection, Regulates the Cytokine Response to Lipopolysaccharide in a Macrophage Type-Specific Manner. *Journal of innate immunity*, *16*(1), 226–247. https://doi.org/10.1159/000538282
- 29. Kellogg, R. A., Tian, C., Etzrodt, M., & Tay, S. (2017). Cellular Decision Making by Non-Integrative Processing of TLR Inputs. *Cell reports*, *19*(1), 125–135. https://doi.org/10.1016/j.celrep.2017.03.027
- 30. Lin, B., Dutta, B., & Fraser, I. D. C. (2017). Systematic Investigation of Multi-TLR Sensing Identifies Regulators of Sustained Gene Activation in Macrophages. *Cell systems*, *5*(1), 25–37.e3. https://doi.org/10.1016/j.cels.2017.06.014
- 31. Gutschow, M. V., Mason, J. C., Lane, K. M., Maayan, I., Hughey, J. J., Bajar, B. T., Amatya, D. N., Valle, S. D., & Covert, M. W. (2019). Combinatorial processing of bacterial and host-derived innate immune stimuli at the single-cell level. *Molecular biology of the cell*, *30*(2), 282–292. https://doi.org/10.1091/mbc.E18-07-0423
- 32. Kawai, T., Ikegawa, M., Ori, D., & Akira, S. (2024). Decoding Toll-like receptors: Recent insights and perspectives in innate immunity. *Immunity*, *57*(4), 649–673. https://doi.org/10.1016/j.immuni.2024.03.004
- 33. Albin, T. J., Tom, J. K., Manna, S., Gilkes, A. P., Stetkevich, S. A., Katz, B. B., Supnet, M., Felgner, J., Jain, A., Nakajima, R., Jasinskas, A., Zlotnik, A., Pearlman, E., Davies, D. H., Felgner, P. L., Burkhardt, A. M., & Esser-Kahn, A. P. (2019). Linked Toll-Like Receptor Triagonists Stimulate Distinct, Combination-Dependent Innate Immune Responses. *ACS central science*, *5*(7), 1137–1145. https://doi.org/10.1021/acscentsci.8b00823

- 33. Woida, P. J., & Satchell, K. J. F. (2022). Bacterial Toxin and Effector Regulation of Intestinal Immune Signaling. *Frontiers in cell and developmental biology*, *10*, 837691. https://doi.org/10.3389/fcell.2022.837691
- 34. Torre, C., & Boyer, L. (2022). Effector-Triggered Trained Immunity: An Innate Immune Memory to Microbial Virulence Factors?. *Toxins*, *14*(11), 798. https://doi.org/10.3390/toxins14110798
- 35. Otte, S., Ipiña, E. P., Pontier-Bres, R., Czerucka, D., & Peruani, F. (2021). Statistics of pathogenic bacteria in the search of host cells. *Nature communications*, *12*(1), 1990. https://doi.org/10.1038/s41467-021-22156-6
- 36. Palma, V., Gutiérrez, M. S., Vargas, O., Parthasarathy, R., & Navarrete, P. (2022). Methods to Evaluate Bacterial Motility and Its Role in Bacterial-Host Interactions. *Microorganisms*, 10(3), 563. https://doi.org/10.3390/microorganisms10030563
- 37. Long, E. M., Millen, B., Kubes, P., & Robbins, S. M. (2009). Lipoteichoic acid induces unique inflammatory responses when compared to other toll-like receptor 2 ligands. *PloS one*, *4*(5), e5601. https://doi.org/10.1371/journal.pone.0005601
- 38. Nilsen, N. J., Deininger, S., Nonstad, U., Skjeldal, F., Husebye, H., Rodionov, D., von Aulock, S., Hartung, T., Lien, E., Bakke, O., & Espevik, T. (2008). Cellular trafficking of lipoteichoic acid and Toll-like receptor 2 in relation to signaling: role of CD14 and CD36. *Journal of leukocyte biology*, 84(1), 280–291. https://doi.org/10.1189/jlb.0907656
- 39. Percy, M. G., & Gründling, A. (2014). Lipoteichoic acid synthesis and function in grampositive bacteria. *Annual review of microbiology*, *68*, 81–100. https://doi.org/10.1146/annurevmicro-091213-112949
- 40. Triantafilou, M., Manukyan, M., Mackie, A., Morath, S., Hartung, T., Heine, H., & Triantafilou, K. (2004). Lipoteichoic acid and toll-like receptor 2 internalization and targeting to the Golgi are lipid raft-dependent. *The Journal of biological chemistry*, 279(39), 40882–40889. https://doi.org/10.1074/jbc.M400466200
- 41. Reynaud, E. G., Krzic, U., Greger, K., & Stelzer, E. H. (2008). Light sheet-based fluorescence microscopy: more dimensions, more photons, and less photodamage. *HFSP journal*, 2(5), 266–275. https://doi.org/10.2976/1.2974980
- 42. Ryu, Y., Kim, Y., Park, S. J., Kim, S. R., Kim, H. J., & Ha, C. M. (2023). Comparison of Light-Sheet Fluorescence Microscopy and Fast-Confocal Microscopy for Three-Dimensional Imaging of Cleared Mouse Brain. *Methods and protocols*, *6*(6), 108. https://doi.org/10.3390/mps6060108
- 43. Ritter, J. G., Veith, R., Veenendaal, A., Siebrasse, J. P., & Kubitscheck, U. (2010). Light sheet microscopy for single molecule tracking in living tissue. *PloS one*, *5*(7), e11639. https://doi.org/10.1371/journal.pone.0011639

- 44. Zhang, D., Cleveland, A. H., Krimitza, E., Han, K., Yi, C., Stout, A. L., Zou, W., Dorsey, J. F., Gong, Y., & Fan, Y. (2024). Spatial analysis of tissue immunity and vascularity by light sheet fluorescence microscopy. *Nature protocols*, *19*(4), 1053–1082. https://doi.org/10.1038/s41596-023-00941-5
- 45. Huisken, J., Swoger, J., Del Bene, F., Wittbrodt, J., & Stelzer, E. H. (2004). Optical sectioning deep inside live embryos by selective plane illumination microscopy. *Science (New York, N.Y.)*, 305(5686), 1007–1009. https://doi.org/10.1126/science.1100035
- 46. Keller, P. J., Schmidt, A. D., Wittbrodt, J., & Stelzer, E. H. (2008). Reconstruction of zebrafish early embryonic development by scanned light sheet microscopy. *Science (New York, N.Y.)*, 322(5904), 1065–1069. https://doi.org/10.1126/science.1162493
- 47. Gao L. (2015). Optimization of the excitation light sheet in selective plane illumination microscopy. *Biomedical optics express*, 6(3), 881–890. https://doi.org/10.1364/BOE.6.000881
- 48. Chen, B. C., Legant, W. R., Wang, K., Shao, L., Milkie, D. E., Davidson, M. W., Janetopoulos, C., Wu, X. S., Hammer, J. A., 3rd, Liu, Z., English, B. P., Mimori-Kiyosue, Y., Romero, D. P., Ritter, A. T., Lippincott-Schwartz, J., Fritz-Laylin, L., Mullins, R. D., Mitchell, D. M., Bembenek, J. N., Reymann, A. C., ... Betzig, E. (2014). Lattice light-sheet microscopy: imaging molecules to embryos at high spatiotemporal resolution. *Science (New York, N.Y.)*, 346(6208), 1257998. https://doi.org/10.1126/science.1257998
- 49. Li, M., Liu, L. & Zambelli, T. FluidFM for single-cell biophysics. *Nano Res.* **15**, 773–786 (2022). https://doi.org/10.1007/s12274-021-3573-y
- 50. Dufrêne Y. F. (2002). Atomic force microscopy, a powerful tool in microbiology. *Journal of bacteriology*, 184(19), 5205–5213. https://doi.org/10.1128/JB.184.19.5205-5213.2002
- 51. Li, M., Xi, N., Wang, Y. C., & Liu, L. Q. (2021). Atomic force microscopy for revealing micro/nanoscale mechanics in tumor metastasis: from single cells to microenvironmental cues. *Acta pharmacologica Sinica*, 42(3), 323–339. https://doi.org/10.1038/s41401-020-0494-3
- 52. Li, J., Liu, Y., Yuan, Y., & Huang, B. (2021). Applications of atomic force microscopy in immunology. *Frontiers of medicine*, *15*(1), 43–52. https://doi.org/10.1007/s11684-020-0769-6
- 53. Knoops, B., Becker, S., Poncin, M. A., Glibert, J., Derclaye, S., Clippe, A., & Alsteens, D. (2018). Specific Interactions Measured by AFM on Living Cells between Peroxiredoxin-5 and TLR4: Relevance for Mechanisms of Innate Immunity. *Cell chemical biology*, 25(5), 550–559.e3. https://doi.org/10.1016/j.chembiol.2018.02.006
- 54. Hu, K. H., Bruce, M. A., Liu, J., & Butte, M. J. (2019). Biochemical Stimulation of Immune Cells and Measurement of Mechanical Responses Using Atomic Force Microscopy. *Current protocols in chemical biology*, *11*(2), e63. https://doi.org/10.1002/cpch.63

- 55. Nagy, Á. G., Kanyó, N., Vörös, A., Székács, I., Bonyár, A., & Horvath, R. (2022). Population distributions of single-cell adhesion parameters during the cell cycle from high-throughput robotic fluidic force microscopy. *Scientific reports*, *12*(1), 7747. https://doi.org/10.1038/s41598-022-11770-z
- 56. Ernst, C., Andreassen, P. R., Giger, G. H., Nguyen, B. D., Gäbelein, C. G., Guillaume-Gentil, O., Fattinger, S. A., Sellin, M. E., Hardt, W. D., & Vorholt, J. A. (2024). Direct Salmonella injection into enteroid cells allows the study of host-pathogen interactions in the cytosol with high spatiotemporal resolution. *PLoS biology*, 22(4), e3002597. https://doi.org/10.1371/journal.pbio.3002597
- 57. Mulder, E. J., Moser, B., Delgado, J., Steinhardt, R. C., & Esser-Kahn, A. P. (2024). Evidence of collective influence in innate sensing using fluidic force microscopy. *Frontiers in immunology*, *15*, 1340384. https://doi.org/10.3389/fimmu.2024.134038456. Ernst, C.,
- 58. Fisch, D., Zhang, T., Sun, H. *et al.* Molecular definition of the endogenous Toll-like receptor signalling pathways. *Nature* (2024). https://doi.org/10.1038/s41586-024-07614-7

CHAPTER 2: RECEPTOR-LIGAND KINETICS INFLUENCE THE MECHANISM OF ACTION OF LINKED TLR AGONISTS

Reprinted with permission from ACS Chem. Biol. 2021, 16, 2, 380–388. Copyright 2021 American Chemical Society.

2.1 Summary

Toll-like receptors (TLRs) are among the most studied pattern recognition receptors (PRRs) that sense a variety of pathogens. Upon activation, they initiate a downstream signaling cascade that produces cytokines, chemokines, and costimulatory molecules. Targeting multiple TLRs through covalent conjugation of ligands has been known to produce synergistic, additive, and subtractive effects, which can uniquely tailor the downstream adaptive immune responses. In our continued efforts to move toward rational development of immune agonists that mimic their spatial distribution in a pathogen, we sought to investigate the mechanism of action of spatially controlled, covalently linked dual TLR agonists.

We report a mechanistic study comparing the immune activation of conjugated Toll-like receptor (TLR) agonists and their unlinked mixtures. Herein, we synthesized a set of 6 linked dual agonists with different ligands, molecular structures, receptor location, and biophysical characteristics. We ran a series of *in vitro* cell-based assays with these dimers, comparing initial and overall NF-κB (nuclear factor kappa-light-chain-enhancer of activated B cells) activation, cytokine expression profiles, and as time-resolved TNF-α (Tumor Necrosis Factor-alpha) expression. We show that initial activation kinetics, ligand specificity, and the dose of the agonist influence the activity of these linked TLR systems. These results can help improve vaccine design by showing how linked TLR agonists can enhance potency with the appropriate selection of key criteria.

2.2 Introduction

Whole-cell vaccines produce potent and prolonged immune responses against pathogens. The efficacy of whole vaccines is due to the simultaneous presentation of multiple pathogenassociated molecular patterns (PAMPs) to innate immune cells, often leading to a robust response and overall protection.^{1,2} Innate immune cells are activated by the recognition and binding of specific PAMPs to receptors such as Toll-like receptors (TLRs).³ This causes a complex signaling cascade that results in the production of inflammatory cytokines, chemokines, and costimulatory molecules which then modulate the magnitude and duration of antigenspecific adaptive responses. 4,5,6 In previous work, we have shown that linked combinations of TLR agonists can serve as a unique alternative to the traditional whole-cell vaccines through spatially constrained multi-TLR presentation and activation. Additionally, such constructs are immunomodulatory, allowing for fine-tuned responses against pathogens of interest.^{7–9} Multi-TLR agonists are therefore promising candidates for application as immunostimulants (adjuvants) in subunit vaccines and are currently included in several pre-clinical trials. 10, 11 We also found that covalently linked agonists induces synergistic responses by increasing inflammatory cytokines and promoting a T_H1-biased response compared to the unlinked agonist mixtures. We observed spatial inductions that change the cytokine and antibody profile as well as epitope affinity.⁷, ¹², ¹³ Others have shown that immune cell response to dual stimulation by a mixture of unlinked agonists and cytokines leads to distinct ligand and dose-dependent NF-κB dynamics. 14,15 Simultaneous activation of TLR 2 and 4 in a cell population using a mixture of Pam₃CSK₄ and LPS resulted in each cell's NF-κB dynamics resembling the response to one or the other ligand and not a combination of both. 14 In contrast, a mixture of TNF- α and LPS led to a combinatory response of NF-κB dynamics. 15 These results taken together suggest that cells

have a complex system of integrating and processing multi TLR signals that may be dependent on upstream events in the NF-κB activation pathway.

Most mechanistic studies of synergistic induction by multiple stimuli have been conducted using mixtures of agonists or cytokines. In our continued efforts to move toward rational development of immune agonists that mimic their spatial distribution in a pathogen, we sought to investigate the mechanism of action of spatially controlled, covalently linked dual TLR agonists. To achieve this, we synthesized a small library of six combinations of linked agonists—varying the size of the agonist, signaling adaptor involved and the location of the TLR. With these six dimers we ran a series of *in vitro* experiments on murine macrophages to define the structural and molecular mechanisms that influence immune responses of linked dual TLR ligands.

2.3 Materials and Methods

Unless otherwise noted, all reagents were purchased from commercial sources and used as received. DBCO-NHCO-PEG₁₃-NHS ester was purchased from BroadPharm. CPG ODN 1826 was purchased from Integrated DNA technologies. Azido acetic acid was purchased from Sigma Aldrich. Peptide reagents were purchased from CEM corporation. Nα-Fmoc-Nε-azide-L-Lysine was purchased from Chem-Impex. Automated solid-phase peptide synthesis was performed using Liberty BlueTM automated peptide synthesizer. Analytical reversed-phase HPLC was performed using Agilent Zorbax SB-C18 or C8 column (50 mm X 4.6 mm) with a flow rate of 1.0 mL/min on an Agilent 1260 Infinity LC system. Preparative reversed-phase HPLC purification was carried using Phenomenex Luna C18 or C8 Prep (150 X 21.2250 mm, 5 μm particle size) column with a flow rate of 21.2 mL/min on a Gilson 333/334 pump system and

GX-271 liquid handler system. UV detection (214 nm, 254 nm, and 260 nm) was used for analytical and preparative HPLC. Size exclusion chromatography was performed on a GE superdex G75 in DPBS, pH 7.4 at a flow rate of 1mL/min with a UV/Vis detector set to monitor at 495 nm and 260 nm. Gel electrophoresis was carried out using Any KD Mini-PROTEAN TGX precast protein gels in a Mini-PROTEAN tetra cell (BIO-RAD). Gel electrophoresis samples were analyzed using Azure biosystems imager. UV-Vis was measured on Thermo Scientific Nano Drop. Mass spectrum was obtained using Agilent LC/MSD. MALDI was obtained using Bruker Ultraflextreme MALDI-TOF/TOF. Cytometric bead array data was acquired on a NovoCyte Benchtop Flow Cytometer. Data was analyzed using student T-test or one-way ANOVA in Graph Pad Prism software. All values were reported as mean ± SD.

2.3.1 Synthetic Procedures

2/6_peg₁₃_9

Synthesis of Pam₂CSK₄GN₃: Rink amide resin (100-200 mesh, 0.55 mmole/g, 0.05 mg) was weighed out into a solid-phase peptide synthesizer reaction vessel. The peptide was constructed by coupling Fmoc-Cys((RS)-2,3-di(palmitoyloxy)-propyl)-OH, Fmoc-Ser(tBu)-OH, Fmoc-Lys-OH, Fmoc-Gly-OH, Nα-Fmoc-Nε-azide-L-Lysine (0.2 M in DMF) from the C terminus to the N terminus. Deprotection was done using 20% piperidine in DMF. Coupling was done after activation with diisopropylcarbodiimide (DIC) (0.5 M in DMF) in the presence of Ethyl cyanohydroxyiminoacetate (oxyma) (1M in DMF). Fmoc-Cys((RS)-2,3-di(palmitoyloxy)-propyl)-OH was coupled at 90°C for 10 min. All other couplings were done at 90°C for 5 min. All reactions and subsequent washes were performed in DMF. After the synthesis was completed, the resin was transferred into a Bio-Rad Poly-Prep chromatography column.

Deprotection and Purification: Global deprotection was done by agitating the resin in trifluoroacetic acid (TFA)/thioanisole/anisole/H₂O (8.5:0.5:0.5:0.5) for 2 hours. The peptide was precipitated by adding the cleavage cocktail filtrate to 30 mL diethyl ether in a 50 mL centrifuge tube pre-cooled to -78°C. The precipitate was collected by centrifuge (4000 XG for 5 min). The precipitate was dissolved in 20% CH₃CN in 0.1%TFA) and filtered through a 0.45 μm syringe filter. Purification was performed using reverse-phase HPLC C8 column (gradient elution with 30–90% CH₃CN /0.1% TFA over 15 min). Pure fractions were pooled together and the peptide was recovered through lyophilization. MALDI-TOF MS (m/z) 1482.38 [M+H] ⁺

Synthesis of 2/6_peg₁₃_9: 5'-FAM-tccatgacgttcctgacgtt-3'-NH2 (2.2 mg, 0.32 μmol) in 3 mL PBS pH 8 was incubated with DBCO-NHCO-PEG₁₃-NHS ester (7 mg, 6.70 μmols, 0.75 mg/ml in DMSO) overnight at 37°C with vigorous stirring while protected from light. The reaction mixture was purified with a centrifugal filter unit with a 3 kDa cutoff, washing (X6) with pH 7.4 PBS to remove unreacted DBCO-NHCO-PEG13-NHS ester. The resulting reaction mixture was diluted to 3 mL PBS pH 8 and incubated with Pam₂CSK₄GK-Azide (3.0 mg, 2.0 μmols, 5 equiv.) overnight at 37°C with vigorous stirring. The reaction mixture was first purified using a centrifugal filter unit with a 3 kDa cutoff washing (X6) with pH 7.4 PBS then purified passed through a 0.2 μm filter and directly purified by fast protein liquid chromatography (Superdex G75, DPBS, 0.2 mL/min). Elution of the heterodimer was confirmed by monitoring the elution absorbance at 495 nm. The dimers were quantified by UV/Vis and quantified via the local Abs_{max} at 495 nm using a standard curve generated by known concentrations of Fam-CPG (Figure A.2.1) before serial dilutions in PBS to relevant assay concentrations.

2/1_peg₁₃_9

Synthesis of Pam₃CSK₄GN₃: Rink amide resin (100-200 mesh, 0.55 mmole/g, 0.05 mg) was weighed out into a solid-phase peptide synthesizer reaction vessel. The peptide was constructed by coupling Palmitic acid, Fmoc-Cys((RS)-2,3-di(palmitoyloxy)-propyl)-OH, Fmoc-Ser(tBu)-OH, Fmoc-Lys-OH, Fmoc-Gly-OH, Fmoc-Lys-azide-OH (0.2M in DMF) from the C terminus to the N terminus. Deprotection was done using 20% piperidine in DMF. Coupling was done after activation with diisopropylcarbodiimide (DIC) (0.5M in DMF) in the presence of Ethyl cyanohydroxyiminoacetate (oxyma) (1M in DMF). Palmitic acid and Fmoc-Cys((RS)-2,3-di(palmitoyloxy)-propyl)-OH were coupled at 90°C for 10 min. All other couplings were done at 90°C for 5 min. All reactions and subsequent washes were performed in DMF. After the synthesis was completed, the resin was transferred into a Bio-Rad Poly-Prep chromatography column.

Deprotection and Purification: Global deprotection was achieved by agitating the resin in trifluoroacetic acid (TFA)/thioanisole/anisole/H₂O (8.5:0.5:0.5:0.5) for 2 hours. The peptide was precipitated by adding the cleavage cocktail filtrate to 30 mL diethyl ether in a 50 mL centrifuge tube pre-cooled to -78°C. The precipitate was collected by centrifuge (4000 XG for 5 min). The precipitate was dissolved in 20% CH₃CN in 0.1% TFA) and filtered through a 0.45 μm syringe filter. Purification was performed using reversed-phase HPLC C8 column (gradient elution with 30–90% Methanol /0.1% TFA over 15 min). Pure fractions were pooled together and the peptide was recovered through lyophilization. MALDI-TOF MS (m/z) 1719.28 [M+H] ⁺

Synthesis of 2/1_peg₁₃**_9:** 5'-FAM-tccatgacgttcctgacgtt-3'-NH2 (2.2 mg, 0.32 μmols) in 3 mL PBS pH 8 was incubated with DBCO-NHCO-PEG₁₃-NHS ester (7 mg, 6.70 μmols, 0.75 mg/ml in DMSO) overnight at 37°C with vigorous stirring. The reaction mixture was purified

with a centrifugal filter unit with a 3 kDa cutoff washing X6 with pH 7.4 PBS to remove unreacted DBCO-NHCO-PEG13-NHS ester. The resulting reaction mixture was divided into 3 equal fractions, diluted to 2 mL with PBS (pH 8.0) and incubated with Pam₃CSK₄GK-Azide (1.0 mg, 0.67 μmols, 5 equiv.,10 mg/ml, DMSO) overnight at 37 °C with vigorous stirring. The reaction mixture was first purified using a centrifugal filter unit with a 3 kDa cutoff washing X6 with pH 7.4 PBS then purified passed through a 0.2 μm filter and directly purified by fast protein liquid chromatography (Superdex G75, DPBS, 0.2 mL/min). Elution of the heterodimer was confirmed by monitoring the elution absorbance at 475 nm. The dimers were quantified by UV/Vis and quantified via the local Abs_{max} at 495 nm using a standard curve generated by known concentrations of Fam-CPG (**Figure A.2.1**) before serial dilutions in PBS to relevant assay concentrations.

2/6_peg₁₃_4

Cyclohexyl amine derivatized TLR 4 activating indole was synthesized as described in previous publications.⁸ To the indole (10 mg, 0.023 mmols) in 2 mL DMSO was added triethylamine (4.5 mg, 0.046 mmoles, 2 equiv.) and DBCO-NHCO-PEG₁₃-NHS ester (10 mg, 0.01 mmoles, 0.5 equiv.) and the mixture stirred at RT overnight. The reaction mixture was purified using reversed-phase HPLC C8 column (gradient elution with 30–90% CH₃CN /0.1% TFA over 15 min). Pure fractions were pooled together and lyophilized to obtain the product as a white powder. (6.2 mg, 40%) MALDI-TOF MS (m/z) 1400.85 [M+Na] ⁺

Synthesis of 2/6_peg₁₃**_4:** Pam₂CSK₄GN₃ (3.2 mg, 0.0021 mmols) and DBCO derivatized indole (3.6 mg, 0.0026 mmols) was incubated with agitation at 37°C for 12 hours. The reaction mixture was purified using reversed-phase HPLC C8 column (gradient elution with

30–90% CH₃CN /0.1% TFA over 15 min). Pure fractions were pooled together and lyophilized to obtain the product as a white powder. (5 mg, 67%) MALDI-TOF MS (m/z) 2860.55 [M+H]⁺ 2/1_peg₁₃_4

Pam₃CSK₄GN₃ (2.0 mg, 0.0015 mmols) and DBCO derivatized indole (2.8 mg, 0.002 mmols) was incubated with agitation at 37°C for 12 hours. The reaction mixture was purified using reversed-phase HPLC C8 column (gradient elution with 30–90% MeOH /0.1% TFA over 10 min). Pure fractions were pooled together and lyophilized to obtain the product as a white powder. (1.7 mg, 37%) MALDI-TOF MS (m/z) 3100.19 [M+H] ⁺

2/6_peg₁₃_7/8

Benzyl amine derivatized TLR 7/8 activating imidazoquinoline was synthesized as described in previous publications.⁷ To the imidazoquinoline (10 mg, 0.027 mmols) in 2 mL DMSO was added triethylamine (4.5 mg, 0.046 mmoles, 2 equiv.) and DBCO-NHCO-PEG₁₃-NHS ester (10 mg, 0.01 mmoles, 0.5 equiv.) and the mixture stirred at RT overnight. The reaction mixture was purified using reversed-phase HPLC C8 column (gradient elution with 30–90% CH₃CN /0.1% TFA over 15 min). Pure fractions were pooled together and lyophilized to obtain the product as a white powder. (7.3 mg, 43%) MALDI-TOF MS (m/z) 1312.34 [M+Na] ⁺

Synthesis of 2/6_peg₁₃_**7/8:** Pam₂CSK₄GN₃ (2.0 mg, 0.0013 mmols) and DBCO derivatized imidazoquinoline (2.0 mg, 0.0016 mmols) was incubated with agitation at 37 °C for 12 hours. The reaction mixture was purified using reversed-phase HPLC C8 column (gradient elution with 30–90% MeOH /0.1% TFA over 10 min). Pure fractions were pooled together and lyophilized to obtain the product as a white powder. (1.3 mg %, 37%) MALDI-TOF MS (m/z) 2772.68 [M+H]⁺

2/1_peg₁₃_7/8

Pam₃CSK₄GN₃ (2.0 mg, 0.0011 mmols) and DBCO derivatized imidazoquinoline (2.0 mg, 0.0016 mmols), in 2 mL DMSO was incubated with agitation at 37°C for 12 h. The reaction mixture was purified using reversed-phase HPLC C8 column (gradient elution with 30–90% MeOH /0.1% TFA over 10 min). Pure fractions were pooled together and lyophilized to obtain the product as a white powder. (1.1 mg, 32%) MALDI-TOF MS (m/z) 3011.68 [M+H] ⁺

2.3.2 Biological Procedures

Raw Blue NF-kB reporter assay

RAW-Blue cells were passaged and plated in a 96 well plate at a density of 100,000 cells/well in 180 μL DMEM containing 10% heat-inactivated FBS (HI-FBS) and selective antibiotics. The cells were stimulated with the conjugates and unlinked controls for 20 to 24 h at 37 °C and 5% CO₂. NF-κB activity was measured by a QUANTI-Blue (InvivoGen) assay and the absorbance was measured at 620 nm using a Multiskan FC plate reader (Thermo Scientific). Measurement of cytokine levels secreted by RAW macrophages and BMDCs stimulated with agonists or unlinked mixtures.

RAW 264.7 macrophages or BMDCs were plated at a density of 100,000 cells/well in 180 μL DMEM containing 10% HIFBS. The cells were stimulated with the conjugates and unlinked controls and supernatants were collected at the desired time points between 2 h and 24 h post stimulation and stored at -20 °C until further analysis. The IL-6 and MCP-1 levels were quantified was performed using Mouse Inflammation Cytokine Bead Arrays (BD, Cat. 552364). The TNF- α levels were measured using HEK-blue TNF-α reporter cell line as described below.

HEK-Blue TNF-α reporter assay

Stimulation of HEK-Blue TNF-α cells with TNF-α triggers a signaling cascade leading to the activation of AP-1/NF-κB and the subsequent production of SEAP. HEK-Blue cells were passaged and plated in a 96 well plate at a density of 100,000 cells/well in 180 μL DMEM containing 10% HI-FBS and selective antibiotics. The cells were stimulated with 20 μL of the stored cell culture supernatants collected at various time points. A standard curve was generated using incubation with recombinant mouse TNF-α. The cells were incubated for 24 h at 37 °C and 5% CO₂. SEAP levels was measured by a QUANTI-Blue (InvivoGen) assay and the absorbance was measured at 620 nm using a Multiskan FC plate reader (Thermo Scientific).

NF-κB Imaging

RAW 264.7 G9 macrophages³⁰ were plated at a density of 50,000-100,000 per well in 8-well microscopy plates in 200 μ L DMEM with 10% FBS and 1% antibiotic-antimycotic and incubated overnight in an incubator at 37 °C and 5% CO₂. The medium was then replaced with 180 μ L DMEM with 10% HI-FBS and incubated for an additional 2 hours. The cells were then stimulated with 20 μ L of the conjugates or unlinked controls for the desired time after which the media was removed and the cells were fixed with 200 μ L cold 3% formaldehyde in PBS for 10 min at room temperature, washed three times with PBS, and stained with HOECHST nuclear stain (0.5 μ g/mL, 200 μ L) for 20 mins at room temperature in the dark. The cells were then washed three times before imaging.

The cells were imaged on an Olympus spinning disc confocal microscope using a 40x water objective. Images captured included GFP NF-κB stain at 480 nm excitation, nuclear HOECHST stain at 405 nm excitation, and a brightfield image. The overlap of the GFP signal and HOECHST signal (indicating nuclear translocation of NF-κB) was determined using

CellProfiler. Briefly, each nucleus in the HOECHST stain was outlined, and then the outlines were slightly shrunken and expanded. In the GFP image, the area between the expanded and original outlines was taken to be cytoplasmic GFP signal, and the area inside the shrunken outline was taken to be nuclear GFP signal. The ratios of these numbers determined cellular activation for each cell. The activation state of each cell was then plotted as a histogram in R. Dynamic light scattering

Dynamic light scattering (DLS) measurements were performed by a Wyatt Mobius DLS instrument. Measurements were performed at 25°C using a laser wavelength of 532 nm.

Scattered light was collected at a fixed angle of 163.5°. The size distribution plots were obtained using the installed software from the instrument.

Endotoxin test

Endotoxin concentrations were determined with ToxinSensorTM Single Test Kit (GenScript) according to the manufacturer's instructions. No gelation occurred with any of the synthesized dimers which confirmed the absence of endotoxin.

2.4 Results

2.4.1 Design and Synthesis of TLR Agonist Heterodimers

TLRs recognize a varied set of PAMPs and can be further classified based on the ligands that activate the TLRs; TLR 1,2 and 6 recognize lipids, TLR 3,7,8 and 9 recognize nucleic acids, and TLR 4 recognizes diverse structural elements.³ To investigate the mechanism of action of the linked TLR agonists, we needed to synthesize a set of molecules sufficient to test (1) molecular variation, (2) receptor location variation, and (3) differences in biophysical characteristics of the ligand.

While the TLR system is limited in the available ligands, we selected five molecules of varying size and receptor identity to form six combinations. The six combinations were made up of synthetic lipopeptides Pam₂CSK₄ (TLR 2/6) and Pam₃CSK₄ (TLR 2/1), ¹⁶⁻¹⁸ synthetic oligonucleotides CPG_ODN 1826 (TLR 9)¹⁹, pyrimido[5,4-b]indole (TLR 4)^{20,21} and imidazoquinoline (TLR 7/8)²². To covalently link the agonists, we synthesized derivatives with orthogonal conjugatable handles and used a heterotelechelic polyethylene glycol (PEG) discrete linker. We installed azide groups on the lipopeptides and used amine-derivatized indole²⁵ and imidazoquinoline²⁷ and CPG for conjugation. With these agonists we made the following pairs: 2/6_peg13_4, 2/6_peg13_7/8, 2/1_peg13_4, 2/1_peg13_7/8, 2/6_peg13_9 and 2/1_peg13_9 (**Figure 2.1**). Based on previous work done by us and others²³, we did not synthesize homodimers (e.g. 4 4 or 9 9) as we were interested in inducing dual TLR stimuli. Similarly, 2/6 and 2/1 both target TLR2-containing receptor complexes rendering dimers of the two as possible antagonists of one or both pathways. Additionally, 7/8_9, dimer targeting endosomal receptors, never showed altered responses in our hands, and we have not reported on these molecules further. These rules left us with these six combinations to examine.

The synthesized dimers were purified by chromatographic techniques and spectroscopically characterized. Synthetic lipopeptides have been shown to self-assemble into micelle structures when studied at a concentration of 0.5 wt%. ²⁴ In this mechanistic study, we sought to rule out self-assembly of the dimers and the influence of secondary structure to immune response. We characterized the dimers by dynamic light scattering in PBS pH 7.4 at experimentally relevant concentrations to investigate possible particle formation and aggregation. At concentrations of 250 nM and above, we observed that the lipopeptide-small molecule dimers formed larger particles than of the parent lipopeptides (**Figure A.2.4**).

2/1_peg13_4, 2/1_peg13_7/8 dimers showed evidence of aggregation with no uniform distribution of particles. However, we did not observe particle formation by DLS at the lower concentrations that we used for *in vitro* analyses.

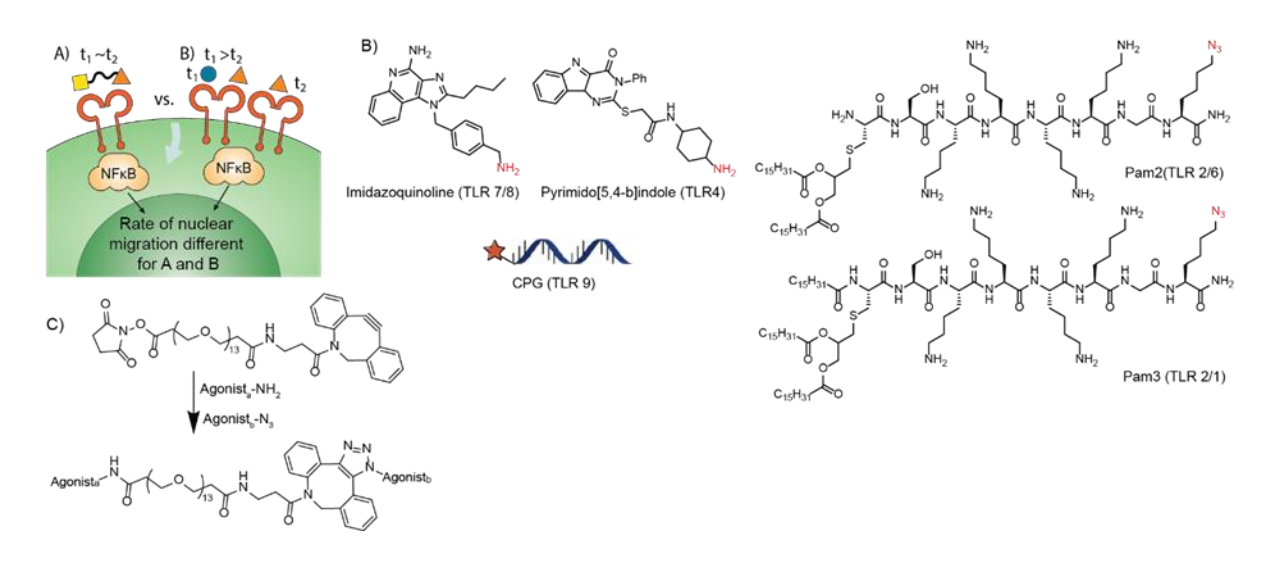


Figure 2.1. Comparing mechanism of NF-κB migration and subsequent immune response after activation with linked agonist and unlinked agonist mixture. (B) Molecular structures of agonist selected in this study. (C) Covalent site-specific linking strategy for synthesis of linked TLR agonist dimers.

2.4.2 NF-κB Activity of TLR Dimers

Initially, we sought to ascertain the differences in activity between these compounds. TLR activation by ligands or agonists activates MyD88 and TRIF pathways where the downstream effect is activation of transcription factors NF-κB and AP-1 (Activator Protein 1).²⁵ Using the RAW 264.7 macrophage reporter cell line, RAW-BlueTM, we profiled the overall transcriptional activity of the linked agonists by measuring the level of secreted embryonic alkaline phosphatase (SEAP) induced by both NF-κB and AP-1. The lipopeptide-CPG dimers, 2/1_peg13_9 and 2/6_peg13_9 showed significantly higher activity than the corresponding equimolar agonist mixtures (**Figure 2.2**). 2/6_peg13_9 was slightly higher compared to the agonist mixtures and the monomers while 2/1_peg13_9 showed an additive response at 10 nM

concentration. Surprisingly, the small molecule derived dimers of Pam₂CSK₄, 2/6_peg13_4 and 2/6_peg13_7/8 2/1_peg13_4 and 2/1_peg13_7/8 showed a subtractive response when compared to the individual and unlinked mixture of agonists. Reduction in activity for conjugated small molecule agonists such as the indole and the imidazoquinoline has been reported and could be attributed to a disruption in the receptor-agonist interactions.⁸ In some cases, the activity is either restored due to synergistic effects after conjugation or the dimer retains the activity of the more potent monomer. In this case, the small molecules conjugated onto the lipopeptide agonists did not increase the cellular response. However, the decrease in activity was not expected indicating a possible molecular change in the cellular immune response. The set of 6 dimers were representative of additive, subtractive and unaltered effects, which made it an ideal toolset to study.

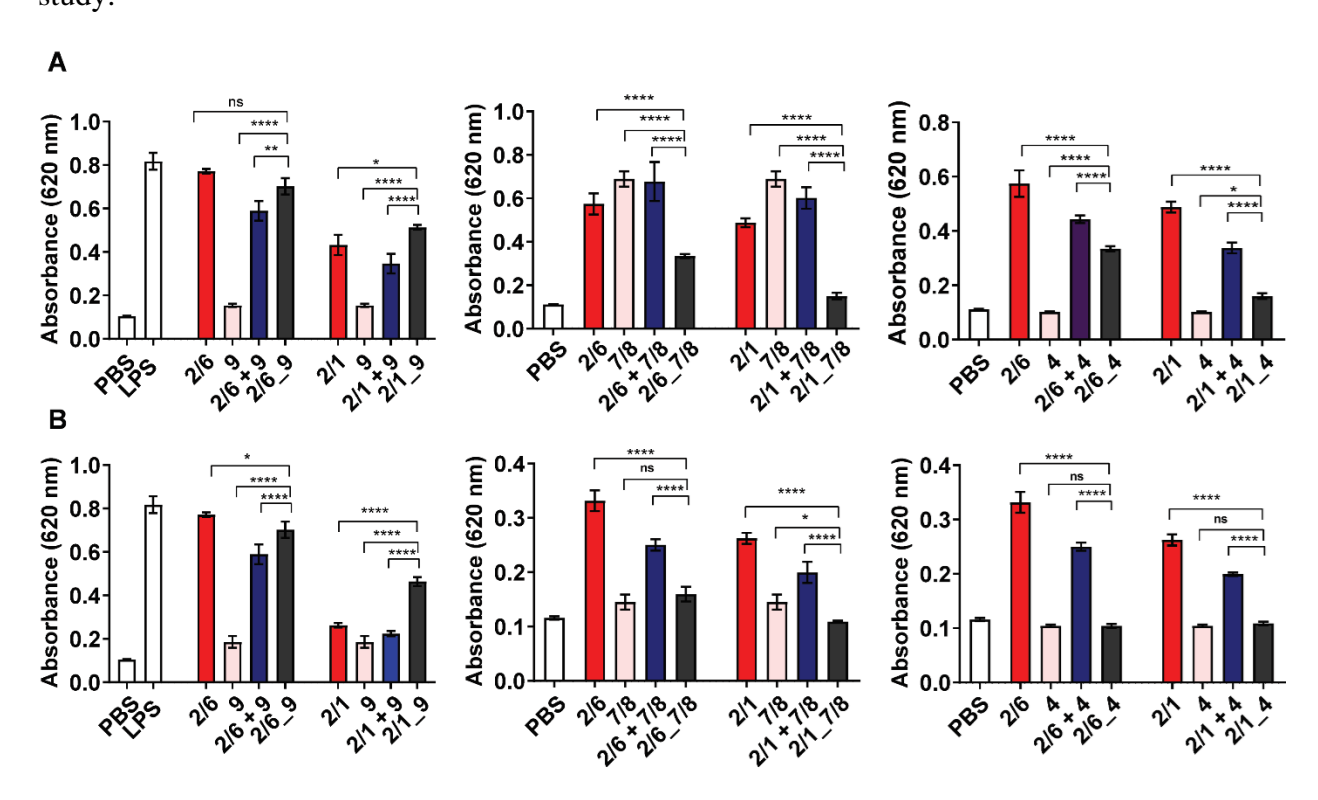


Figure 2.2. Immune activation of Pam₂CSK₄ (2/6), Pam₃CSK₄ (2/1), CpG_1826 (9) indole (4) and imidazoquinoline (7/8), corresponding equimolar mixtures and linked agonists measured by RAW-Blue activation *via* NF-κB stimulation after 24 h incubation at 37 °C. A) 50 nM, B) 10 nM. Samples run in

triplicate. Statistical significance is between the single, unlinked mixtures vs linked agonists, compared by the one-way ANOVA * $p \le 0.05$, **** $p \le 0.0001$.

2.4.3 Comparing Cytokine Secretion Profiles of Linked and Unlinked Agonists

After analysis of overall immune activation using RAW-BlueTM assay, we compared the cytokine profile of cells treated with linked and unlinked equimolar heterodimer agonists. Equimolar mixtures of agonists and ligands resulted in either synergistic or inhibitory cytokine responses. The downstream effects are governed by the interaction of the MyD88 and TRIF pathways. Upon recognition of PAMPs, TLRs initiate downstream signaling with the help of adaptor proteins, mainly MyD88 and TIR-domain-containing adapter-inducing interferon-β (TRIF). While all TLRs except TLR 3 activate MyD88, TRIF is only activated by TLR 3 and 4. MyD88 signaling leads to the activation of NF-κB thereby producing pro-inflammatory cytokines such as IL-6 and TNF-α. Signaling through the TRIF pathway results in the production of inflammatory cytokines and type 1 interferons. TLR4 activates both MyD88 and TRIF pathways.⁵ Inhibitory responses are caused by tolerance induced by sequential activation of multiple pathways. ²⁶⁻²⁸ By conjugating the agonists, we had more spatial and temporal control on the simultaneous activation of dual TLR receptors on a single cell. We incubated bone marrowderived dendritic cells (BMDCs) with 25 nM linked agonists and the corresponding equimolar single agonist. We measured the secreted cytokines after 24 h using an inflammatory panel cytokine bead array assay for IL-6, IL-10, MCP-1, IFN-γ, TNF-α, and IL-12p70. We detected measurable levels of TNF- α , MCP-1 and IL-6 levels at this concentration. We observed no significant differences in cytokine production between the lipopeptide-CPG dimers and the corresponding monomers and unlinked mixtures. Most lipopeptide derived indole dimers showed lower levels of TNF-α, IL-6 and MCP-1—except 2/6_peg13_4 which had higher levels of TNF- α (**Figure 2.3**). This cytokine secretion profile correlated results from the RAW-BlueTM assay,

indicating that for these dimers, the level of activation of NF- κ B was linked to the amount of cytokine secreted. On the other hand, we did not observe any synergistic or additive secretion of cytokines in cells treated with the 2/1_peg13_9 dimer which had shown higher immune response in the RAW-BlueTM assay. In addition, the 2/6_peg13_7/8 dimer induced similar cytokine secretion levels in contrast to the lower immune activity as shown by the RAW-Blue assay at the same concentration.

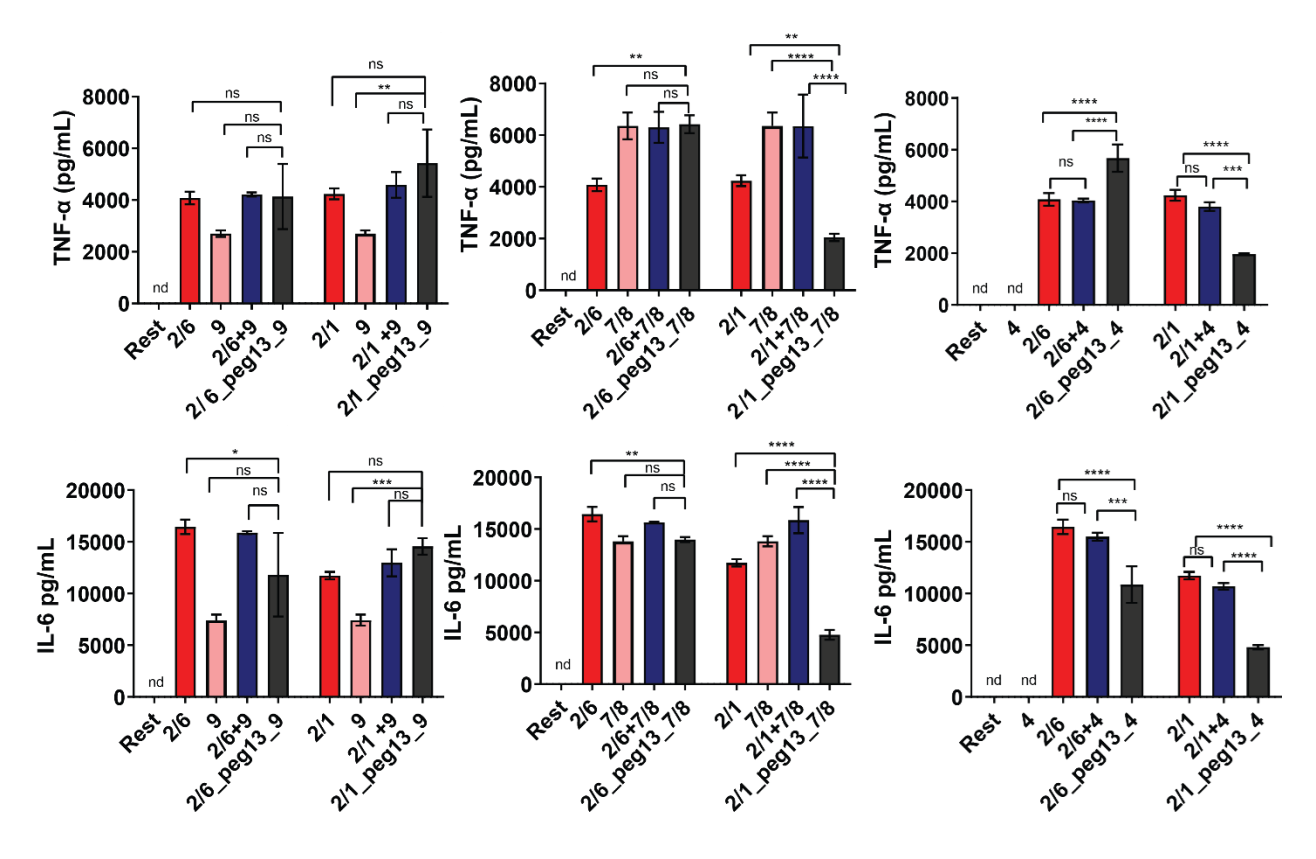


Figure 2.3 *In vitro* cytokine production from BMDC cells measured by cytokine bead array assay. Cells were incubated with 25 nM of Pam_2CSK_4 (2/6), Pam_3CSK_4 (2/1), CpG_1826 (9) indole (4) and imidazoquinoline (7/8), corresponding equimolar mixtures and linked agonists for 24 h at 37 °C, 5% CO₂. Samples run in triplicate. Statistical significance is between the single, unlinked mixtures vs linked agonists, compared by the one-way ANOVA *p \leq 0.05, **** p \leq 0.0001

2.4.4 Effect of Dose on TNF-α Secretion Over Time

After observing the differences in cytokines, we became curious as to why these differences appeared to contrast so much between different compounds and different agonist

sets. In these experiments, we noted that, while TNF- α levels appeared similar after 24 h, at earlier time points there were distinct differences, implying that kinetics of synergistic interactions are related to early time points. We decided to explore these kinetic differences further, as they seemed to show a potential explanation for clear distinctions between the agonists. Investigating TNF- α secretion could explain the differences observed in the other cytokines and provide a standard basis for comparison, as most agonist sets resulted in similar levels at 24 h. In previous reports, we have also observed that lowering agonist concentration can sometimes alter the synergistic response, so we conducted our kinetic screen with varying concentrations. Using RAW 264.7 macrophages, we measured the secretion of TNF-α from 0-24 hr at 2 and 4 h intervals after stimulating the cells with agonists at concentrations of 10, 25, and 50 nM. We observed dose- and time-dependent activity for the different agonist combinations. At lower concentrations (10 nM), treatment with 2/1_peg13_4, 2/6_peg13_4 and 2/1_peg13_7/8 dimers consistently produced lower cytokine secretion over 24 h. As the dose was increased, these dimers activated RAW 264.7 cells at comparable levels as the unlinked equimolar mixtures (**Figure 2.4**). This data suggests that activation of TLRs was modulated by the rate of receptoragonist interactions for these dimers, which increased as the dimer concentration increased. However, for the 2/1_peg13_9 dimer, we observed a significant increase in TNF-α secretion at lower concentrations, but this effect was not observed at higher concentrations. This correlated with the overall immune activity data measured by RAW-BlueTM assay (**Figure 2.2**) suggesting that a synergistic activation involving these specific 2/1 and 9 agonists is facilitated by conjugation.

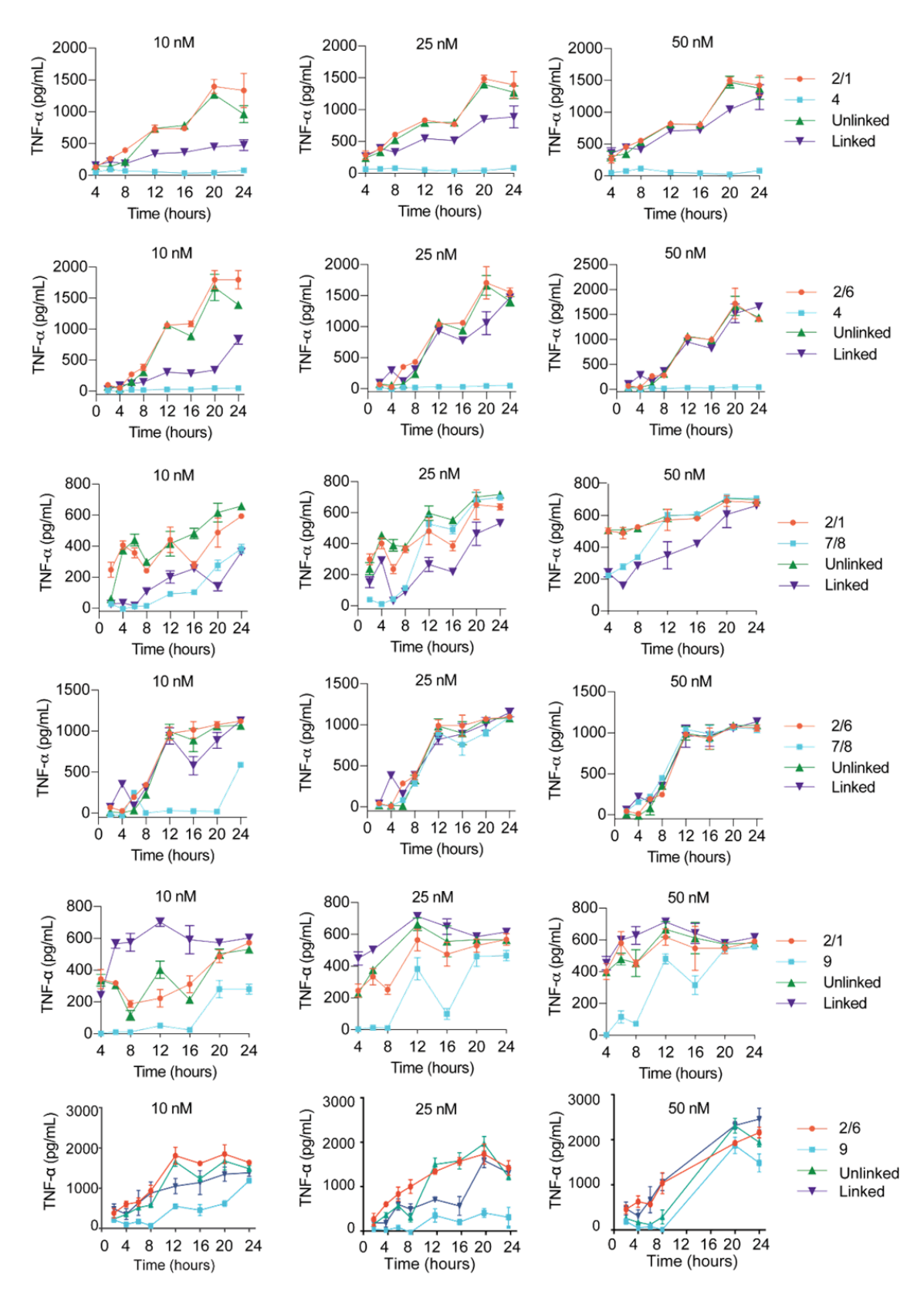


Figure 2.4. Kinetic profiling of cytokine TNF-α secretion. RAW macrophages were incubated with of Pam₂CSK₄ (2/6), Pam₃CSK₄ (2/1), CpG_1826 (9) indole (4) and imidazoquinoline (7/8), corresponding

equimolar mixtures and linked agonists at 10, 25 and 50 nM concentrations. Secreted TNF- α in the supernatant was measured at defined time intervals for 24 hours. The supernatant was incubated with HEK-Blue TNF- α reporter cell line for 20 to 24 h and quantified using TNF- α standards by measuring secreted SEAP levels.

2.4.5 NF-kB Translocation Kinetics

Upon observing the differences in cytokine production that did not uniformly correlate with the overall immune activity measured by RAW-BlueTM assay 24 h after activation, we hypothesized that initial transcription kinetics would give insight into the differences in activity. This hypothesis is based on mounting evidence that NF-kB activation and translocation from cytoplasm to the nucleus is a rapid response to TLR activation and the first step towards transcription of immune genes.²⁹ We expected that a synergistic response would correlate to higher rate of transcription and, conversely, that an inhibitory response would correlate to a lower rate of transcription. Using an engineered RAW 264.7 cell line with a stably expressed GFP-tagged fusion of the RelA NF-κB protein, we quantified and compared the rate of NF-κB translocation of the linked agonists and unlinked mixtures.³⁰ After treating the cells with the linked agonists and the corresponding single and unlinked mixtures, we used confocal microscopy to track GFP-tagged NF-κB translocation from cytoplasm to nucleus. A nuclear stain allowed us to calculate the ratio of nuclear to cytoplasmic NF-κB in each cell using CellProfiler. Using this technique, we resolved single-cell-level differences in NF-κB response dynamics. Comparing distributions of single-cell activation we observed distinct patterns of activation of the cells when treated with the dimers, equimolar mixtures or single agonists. The activation profiles of most of the unlinked mixtures resembled that of the monomers. Most of the dimers seemed to follow this trend and resemble the unlinked mixtures and the monomers in the activation profiles. In contrast the 2/1_peg13_4 dimer profile matched the TLR 4 agonist with the unlinked mixture resembling the TLR 2/1 agonist (Figure 2.5). Interestingly, this data

correlates closely with the difference we had observed in the RAW-BlueTM assay (**Figure 2.2**) where we saw significant differences in activity for the indole (TLR 4) activating dimers. These distinct profile patterns indicate that the linked agonists' activation of NF κ B is determined by specific ligand interactions.

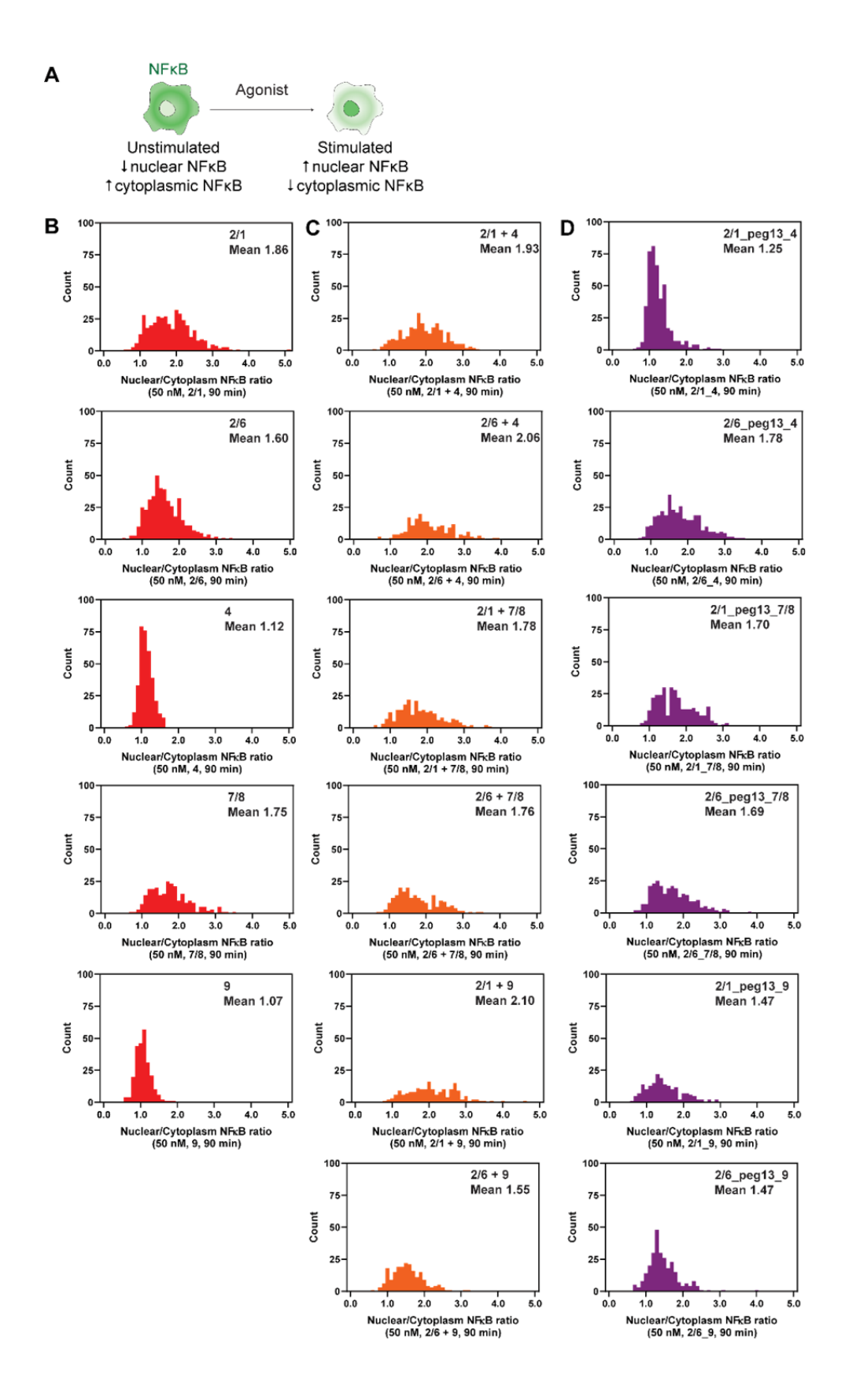


Figure 2.5. Single-cell analysis NF-κB migration studies. A) GFP- NF-κB migration from the cytoplasm to the nucleus. RAW-G9 cells containing NF-κB-GFP are imaged and the kinetics of NF-κB migration into the nucleus are quantified after 90 minutes of stimulation with 50 nM B) Pam₂CSK₄ (2/6), Pam₃CSK₄ (2/1), CPG (9) indole (4) and imidazoquinoline (7/8), C) corresponding equimolar mixtures and D) linked agonists. Each image contains a distribution the ratios for all cells in the field of view for multiple images. Mean values were calculated from all available data.

When we investigated the effect of dose on the NF-κB activation profiles we observed a change in the activation profile of the 2/1_peg13_4 dimer. At this lower concentration (10 nM) the dimer activated more cells to >2 nuclear/cytoplasm ratio. The profile also seemed to resemble the activation profile of the lipopeptide and the mixture of agonists (2/1 and 2/1 +4). However, the lipopeptide-CPG dimers had a similar NF-κB activation profile was similar to the lipopeptides and the agonist mixtures at both concentrations (**Figure 2.6**).

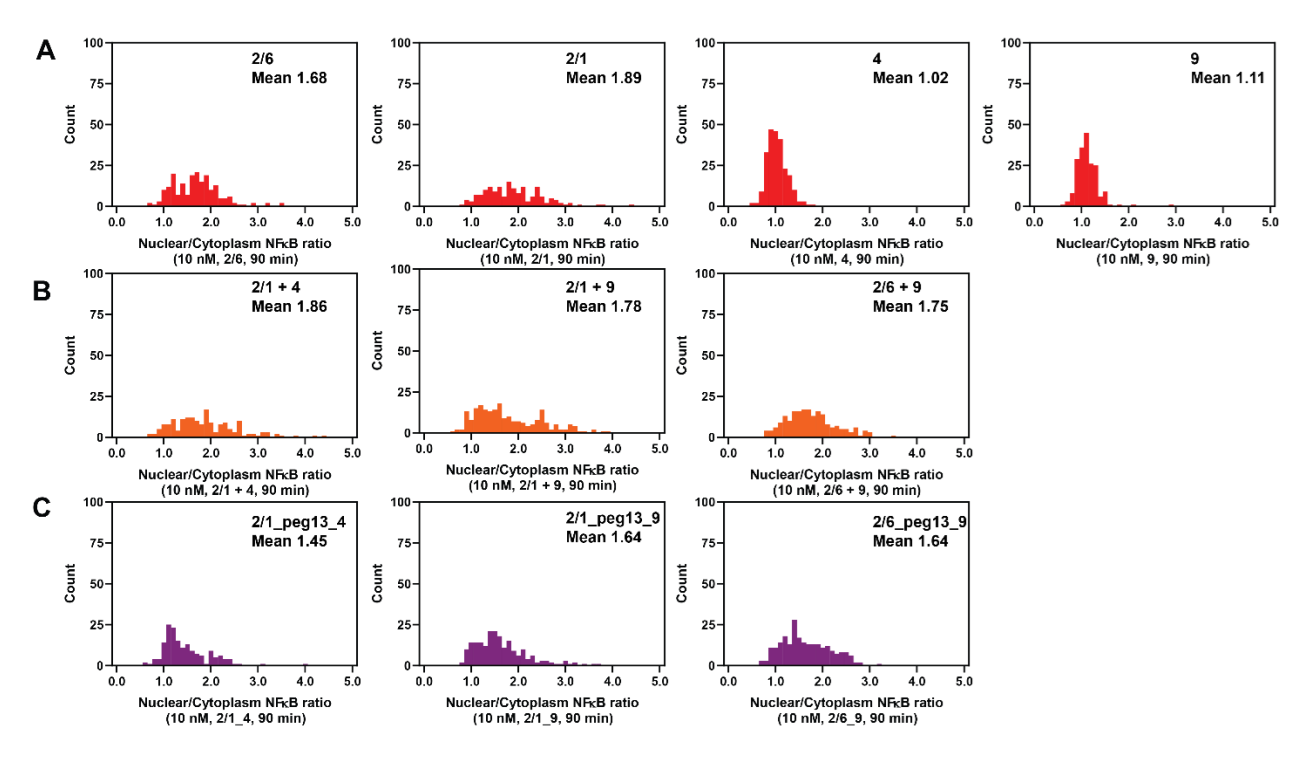


Figure 2.6. Effect of dose on NF-κB migration. RAW-G9 cells containing NF-κB-GFP are imaged and the kinetics of NF-κB migration into the nucleus are quantified after 90 min. of stimulation with 10 nM A) Pam₂CSK₄ (2/6), Pam₃CSK₄ (2/1), CPG (9) and indole (4) B) corresponding equimolar mixtures and C) linked agonists. Each image contains a distribution the ratios for all cells in the field of view for multiple images. Mean values were calculated from all available data.

2.5 Discussion

Linked TLR agonists elicit unique responses in both *in vitro* and *in vivo* systems. Understanding how these multi-activating systems works is key in the rational development of vaccine adjuvants. Combinatory responses to multiple stimuli by unlinked agonist mixtures is correlated to synergistic immune responses and distinct NF-κB activation profiles. Previous work has shown that cellular integration and processing of these multiple stimuli is specific to the type of NF-κB activating stimuli and processing capacity. ^{14,15} Our study on the mechanism of activation of linked dual TLR agonists suggests that ligand-receptor interactions influence initial transcriptional kinetics and thus downstream cytokine secretion profiles. The immune response is also dictated by specific single ligand interactions which can be attributed to the physical characteristics of the dimer constituents, the potency of the agonist pair, or the pathway (MyD88 and TRIF) that is activated by the agonist pair.

Overall NF-κB activity measured by RAW 264.7 cells showed significant differences in immune response when comparing between linked and unlinked agonists. These differences in activity were dose- and agonist-dependent with unaltered, additive, and inhibitory outcomes. Synthetic lipopeptides Pam₃CSK₄ and Pam₂CSK₄ both stimulate cell surface, membrane-bound TLR2 complexes. However, the dimers derived by conjugating these two agonists to small-molecule agonists—indole (TLR4) and imidazoquinoline (TLR7/8)—had different immune activity and cytokine secretion profiles. The dimers showed inhibitory NF-κB immune activity with lower downstream cytokine secretion compared to treatment with the lipopeptides and agonist mixtures. The lipopeptide-CPG dimers showed an increase in immune activity that was more pronounced at lower concentrations.

By evaluating single-cell NF-κB dynamics we observed that 2/1 peg13 4 had a similar profile as the cells stimulated with indole (TLR 4) suggesting that this dimer preferentially activates through TLR 4. The low potency of the TLR4 activating indole could explain the decrease in the immune activity of this dimer especially if the dimer preferentially activates through the TLR 4 receptor. This agonist biasing effect was not observed with the 2/1_peg13_7/8, 2/6_peg13_4, and the 2/6_peg13_7/8 which had a similar profile as the corresponding unlinked mixture and the single agonists. Additionally, the time course of TNF-α cytokine secretion over time further illustrates the dose and agonist specificity of the linked agonists. Ligand-receptor interactions depend on the dose of the agonist with the high immune response being attributed to increased interactions. In the TNF-α secretion data set, we observe that increase in the dose of 2/1_peg13_7/8 and 2/1_peg13_4 dimers from 10 nM to 50 nM led to similar levels of cytokine production as the unlinked agonist and the corresponding mixtures. However, in the case of 2/1_peg13_9 we observe synergy in the overall immune response as well as in TNF- α secretion in lower concentrations but not at higher concentrations, indicating that for this dimer the synergistic interaction is derived from the altered kinetics of NF- κB signaling. While we have not definitively concluded what physical phenomenon results in the altered kinetics, by contrasting TLR 2/1 and TLR 2/6 systems, we can conjecture that the difference may stem either from specific receptor pairings enhanced by linkage or by strong lipid interactions of the tri-palmitoylation of the TLR 2/1 agonist.

In this study, we show that the activity of dual linked agonists is both ligand- and dose-dependent. By observing the initial kinetics of activation, we observed distinct NF-κB dynamics that can be attributed to how the immune cells integrate and process two activation signals, which further informs the downstream immune response. Using this set of dimers, we show

ligand-dependent immune response with synergy being induced with only specific sets of dimers. We also observe a dependence of dose on the magnitude of the immune response, which indicates that kinetics of receptor activation by the ligands play a role in the mechanism of activation in linked systems.

2.6 References

- 1. Pulendran, B. & Ahmed, R. Immunological mechanisms of vaccination. *Nat Immunol* **12**, 509–517 (2011).
- 2. Ahmed, R. & Pulendran, B. Learning vaccinology from viral infections. *Journal of Experimental Medicine* **208**, 2347–2349 (2011).
- 3. Akira, S., Uematsu, S. & Takeuchi, O. Pathogen recognition and innate immunity. *Cell* **124**, 783–801 (2006).
- 4. Parker, L. C., Prince, L. R. & Sabroe, I. Translational Mini-Review Series on Toll-like Receptors: Networks regulated by Toll-like receptors mediate innate and adaptive immunity. *Clin Exp Immunol* **147**, 199–207 (2007).
- 5. Kawasaki, T. & Kawai, T. Toll-Like Receptor Signaling Pathways. *Frontiers in Immunology* **5**, (2014).
- 6. Tipping, P. G. Toll-Like Receptors: The Interface between Innate and Adaptive Immunity. *JASN* **17**, 1769–1771 (2006).
- 7. Tom, J. K. *et al.* Modulation of Innate Immune Responses via Covalently Linked TLR Agonists. *ACS Cent. Sci.* **1**, 439–448 (2015).
- 8. Albin, T. J. *et al.* Linked Toll-Like Receptor Triagonists Stimulate Distinct, Combination-Dependent Innate Immune Responses. *ACS Cent. Sci.* **5**, 1137–1145 (2019).
- 9. Gilkes, A. P. *et al.* Tuning Subunit Vaccines with Novel TLR Triagonist Adjuvants to Generate Protective Immune Responses against Coxiella burnetii. *J Immunol* **204**, 611–621 (2020).
- 10. Madan-Lala, R., Pradhan, P. & Roy, K. Combinatorial Delivery of Dual and Triple TLR Agonists via Polymeric Pathogen-like Particles Synergistically Enhances Innate and Adaptive Immune Responses. *Sci Rep* **7**, 2530 (2017).
- 11. Orr, M. T. *et al.* A Dual TLR Agonist Adjuvant Enhances the Immunogenicity and Protective Efficacy of the Tuberculosis Vaccine Antigen ID93. *PLOS ONE* **9**, e83884 (2014).
- 12. Mancini, R. J., Tom, J. K. & Esser-Kahn, A. P. Covalently coupled immunostimulant heterodimers. *Angew Chem Int Ed Engl* **53**, 189–192 (2014).
- 13. Ryu, K. A., Slowinska, K., Moore, T. & Esser-Kahn, A. Immune Response Modulation of Conjugated Agonists with Changing Linker Length. *ACS Chem Biol* **11**, 3347–3352 (2016).
- 14. Kellogg, R. A., Tian, C., Etzrodt, M. & Tay, S. Cellular Decision Making by Non-Integrative Processing of TLR Inputs. *Cell Reports* **19**, 125–135 (2017).

- 15. Gutschow, M. V. *et al.* Combinatorial processing of bacterial and host-derived innate immune stimuli at the single-cell level. *MBoC* **30**, 282–292 (2019).
- 16. Takeuchi, O. *et al.* Discrimination of bacterial lipoproteins by Toll-like receptor 6. *Int Immunol* **13**, 933–940 (2001).
- 17. Buwitt-Beckmann, U. *et al.* Toll-like receptor 6-independent signaling by diacylated lipopeptides. *Eur J Immunol* **35**, 282–289 (2005).
- 18. Aliprantis, A. O. *et al.* Cell activation and apoptosis by bacterial lipoproteins through toll-like receptor-2. *Science* **285**, 736–739 (1999).
- 19. Krieg, A. M. *et al.* CpG motifs in bacterial DNA trigger direct B-cell activation. *Nature* **374**, 546–549 (1995).
- 20. Chan, M. *et al.* Identification of substituted pyrimido[5,4-b]indoles as selective Toll-like receptor 4 ligands. *J Med Chem* **56**, 4206–4223 (2013).
- 21. Chan, M. *et al.* Structure-Activity Relationship Studies of Pyrimido[5,4-b] indoles as Selective Toll-Like Receptor 4 Ligands. *J. Med. Chem* 60, 9142–9161 (2017).
- 22. Shukla, N. M., Malladi, S. S., Mutz, C. A., Balakrishna, R. & David, S. A. Structure-activity relationships in human toll-like receptor 7-active imidazoquinoline analogues. *J Med Chem* **53**, 4450–4465 (2010).
- 23. Shukla, N. M. *et al.* Toll-Like Receptor (TLR)-7 and -8 Modulatory Activities of Dimeric Imidazoquinolines. *J. Med. Chem.* **55**, 1106–1116 (2012).
- 24. Hamley, I. W. *et al.* Toll-like receptor agonist lipopeptides self-assemble into distinct nanostructures. *Chem. Commun.* **50**, 15948–15951 (2014).
- 25. Takeda, K. & Akira, S. TLR signaling pathways. Semin Immunol 16, 3–9 (2004).
- 26. Napolitani, G., Rinaldi, A., Bertoni, F., Sallusto, F. & Lanzavecchia, A. Selected Toll-like receptor agonist combinations synergistically trigger a T helper type 1-polarizing program in dendritic cells. *Nat Immunol* **6**, 769–776 (2005).
- 27. Trinchieri, G. & Sher, A. Cooperation of Toll-like receptor signals in innate immune defence. *Nat Rev Immunol* **7**, 179–190 (2007).
- 28. Liu, Q. & Ding, J. L. The molecular mechanisms of TLR-signaling cooperation in cytokine regulation. *Immunol Cell Biol* **94**, 538–542 (2016).
- 29. Karin, M. & Ben-Neriah, Y. Phosphorylation meets ubiquitination: the control of NF-[kappa]B activity. *Annu Rev Immunol* **18**, 621–663 (2000).

30. Ernst, O., Vayttaden, S. J. & Fraser, I. D. C. Measurement of NF- κ B Activation in TLR-Activated Macrophages. *Methods Mol Biol* **1714**, 67–78 (2018).

CHAPTER 3: DEVELOPING A FLUORESCENT TLR2 LABELING SYSTEM TO INVESTIGATE RECEPTOR DYNAMICS IN LIVE MICROSCOPY

3.1 Summary

Adaptive immune research has benefited greatly from efforts to image and track receptor complexes and components during immune signaling; however, the biophysical dynamics of pattern recognition receptors in innate immunity are not well understood owing to limited methods suitable for labeling and tracking these receptors. Here, we develop and characterize a Fab fragment-based TLR2 label for live microscopy tracking applications. We demonstrate that it is specific for TLR2 and has minimal impact on macrophage signaling and no cross-reactivity with stimulatory Gram-positive bacteria of interest. Our label can be used to assay TLR2 dynamics in live macrophages to elucidate the biophysical underpinnings of innate immune stimulation and responses.

3.2 Introduction

The features of cellular receptors' physical dynamics are critical to their function—and often, characterizing receptor dynamics can lend crucial understanding to cellular systems and processes. In immunology, for example, much research has been conducted describing T cell receptor microcluster dynamics and the structural nature of T cell activation in adaptive immunity^{1,2}. In these studies, researchers find that actin-dependent structuring of T cell receptors with other proteins happens within minutes³ of ligand activation and is critical for signal amplification⁴ for the T cell. Some of the most illustrative work on the matter has involved visualization of the microcluster complexes and ligand-receptor interactions with microscopy—including single-molecule imaging of the ligand-receptor complex⁵, tracking of

receptor synapse formation under constrained geometry⁶, and observing the presence of and characterizing the pre-formed microclusters on T cells independent of stimulation⁷.

Despite the utility of these findings in understanding the mechanisms of adaptive immunity, similar care has not been used to date to assay the biophysical dynamics of innate immune receptors. Though PRR organization and clustering has been sparingly shown^{8,9,10} and theorized about^{11,12}, direct observation of TLRs on live macrophages and the effects of stimulation on their biophysics has been limited due in part to the need to develop suitable imaging platforms to measure and track TLRs. Here, we describe the development of an antibody Fab fragment based TLR2 label capable of illustrating TLR2 dynamics in live lattice light sheet microscopy (LLSM). Our system uses bright, photostable, and conjugable Alexa Fluor 647 to easily label membrane-bound TLR2 in macrophages and allows for robust tracking of the resulting labeled receptors with high signal-to-noise ratio and little-to-no impact on the cell's immune signaling efficacy. LLSM has been shown capable of imaging resting and stimulated adaptive immune cell receptors in three dimensions to better understand the cells and their signaling states¹³, and we hope to approach innate immune cell understanding in similar ways using our system.

3.3 Materials and Methods

TLR2 Antibody Digestion

Whole anti-TLR2 antibodies (clone 6C2, eBioscience) were digested via papain digestion using a Pierce Fab Preparation Kit (Thermo Scientific). 600 µg of antibody was spin concentrated in 10 kDa MWCO microcentrifuge spin filters (Millipore). The concentrated sample was brought up to 500 µL in the cystine-HCl Fab digestion buffer provided with the Fab

preparation kit. This sample was desalted using the kit spin desalting column protocol and then incubated with the kit immobilized papain resin for four hours at 37°C with end-over-end mixing. The digested sample was spun out of the column and stored for downstream purification. Digestion was confirmed using SDS-PAGE gel electrophoresis.

TLR2 Fab Purification

Fab purification was carried out using an AminoLink Plus Immobilization Kit (Thermo Scientific) conjugated with anti-Rat IgG Fc antibodies (Sigma-Aldritch). Conjugation was accomplished following the kit protocol with pH 10 Coupling Buffer and overnight incubations where relevant. Affinity purification was also carried out per protocol with the digested antibody sample being incubated in the affinity column for 45 minutes. Purification was confirmed using SDS-PAGE gel electrophoresis.

TLR2 Fab Fragment AlexaFluor 647 Labeling

The purified Fab fragments were spin filtered and brought up to 1 mg/mL concentration in PBS via NanoDrop (ND-2000c, Thermo Scientific) reading. The Fabs were then labeled using an Alexa Fluor 647 Microscale Labeling Kit per kit instructions with MR = 15, MW = 50,000 Da, and a 30-minute incubation in with end-over-end mixing in the AF 647 reaction mixture. Degree of labeling was assessed using NanoDrop measurements per kit instructions. The Fabs were finally passed through a $0.22~\mu m$ syringe filter to sterilize them after the cutting and labeling procedure.

Immortalized Cell Culture

HEK-Null and HEK-Blue hTLR2 (Invivogen) cells were maintained in DMEM (Life Technologies) supplemented with 10% fetal bovine serum (FBS) (Life Technologies) and 1% antibiotic-antimycotic (Life Technologies) at 37°C and 5% CO₂ in T75 cell culture flasks.

HEK-Blue hTLR2 Assay

HEK-Blue hTLR2 cells (Invivogen) were scraped from their flasks and resuspended in DMEM supplemented with 10% HI-FBS and 1% antibiotic-antimycotic. 50,000 HEK-Blue hTLR2 cells per well were added to a 96 well plate at 200 μL per well and let to incubate overnight at 37°C and 5% CO₂.

The next day, the medium in the HEK-Blue cells was aspirated and replaced with 50 µL per well of medium in the presence or absence of TLR2 Fab label and left to incubate for 1 hour at 37°C and 5% CO₂. Medium was then aspirated, and the cells were washed three times in fresh medium. The medium in the HEK-Blue cells was then replaced with 200 µL per well of LTA supplemented medium at 100ng/mL and left to incubate for overnight at 37°C and 5% CO₂. The next day, the cells were tested for SEAP activity in the supernatant using a QUANTI-Blue (InvivoGen) assay per protocol with absorbance measured at 620 nm using a Multiskan FC plate reader (Thermo Scientific).

Confocal Microscopy

Cells were imaged on an Olympus spinning disc confocal microscope using a 40x water objective (UAPON-340) and EMCCD camera (Teledyne Evolve). To image HEK cells labeled with TLR2 Fab, 50,000 cells per well were plated in an 8-well tray with glass coverslip (Nunc, Thermo Fisher) in DMEM + 10% HI-FBS and left to incubate overnight at 37°C and 5% CO₂. The next day, the cells were incubated with labeled TLR2 Fab at 1:50 concentration for 1 hour. Cells were then washed three times in fresh medium before imaging.

3.4 Results

Antibody staining has long been a standard for fluorescent microscopy; however, antibodies lend a couple problems for molecular tracking applications in macrophages. Firstly, Fc receptors are among the PRRs present on macrophage surfaces—which bind and are immunologically responsive to the Fc portion of antibodies¹⁴. This binding can lead to undesired non-specific staining and immune responses. Additionally, because antibodies have two binding sites for their antigen, it means that two antigen molecules can be constrained together using a single antibody label. Since this artificially alters the organization and interactions between tracked objects, monovalent labels are preferable. To navigate both these problems, we first used papain digestion to fragment a TLR2 antibody (clone 6C2) to into the Fc and Fab fragments. To purify the Fabs, we used an affinity column immobilized with anti-Rat IgG antibodies before concentrating the purified Fab for use. We confirmed the purification of the Fab fragments using SDS-PAGE (Figure 3.1). We then labeled the Fab fragments using succinimidyl ester-conjugated Alexa Fluor 647 (AF 647) to react with primary amines naturally present on the Fab fragment. We checked degree of labeling for the Fab fragments by checking absorbance of the sample at 280 nm and 650 nm.

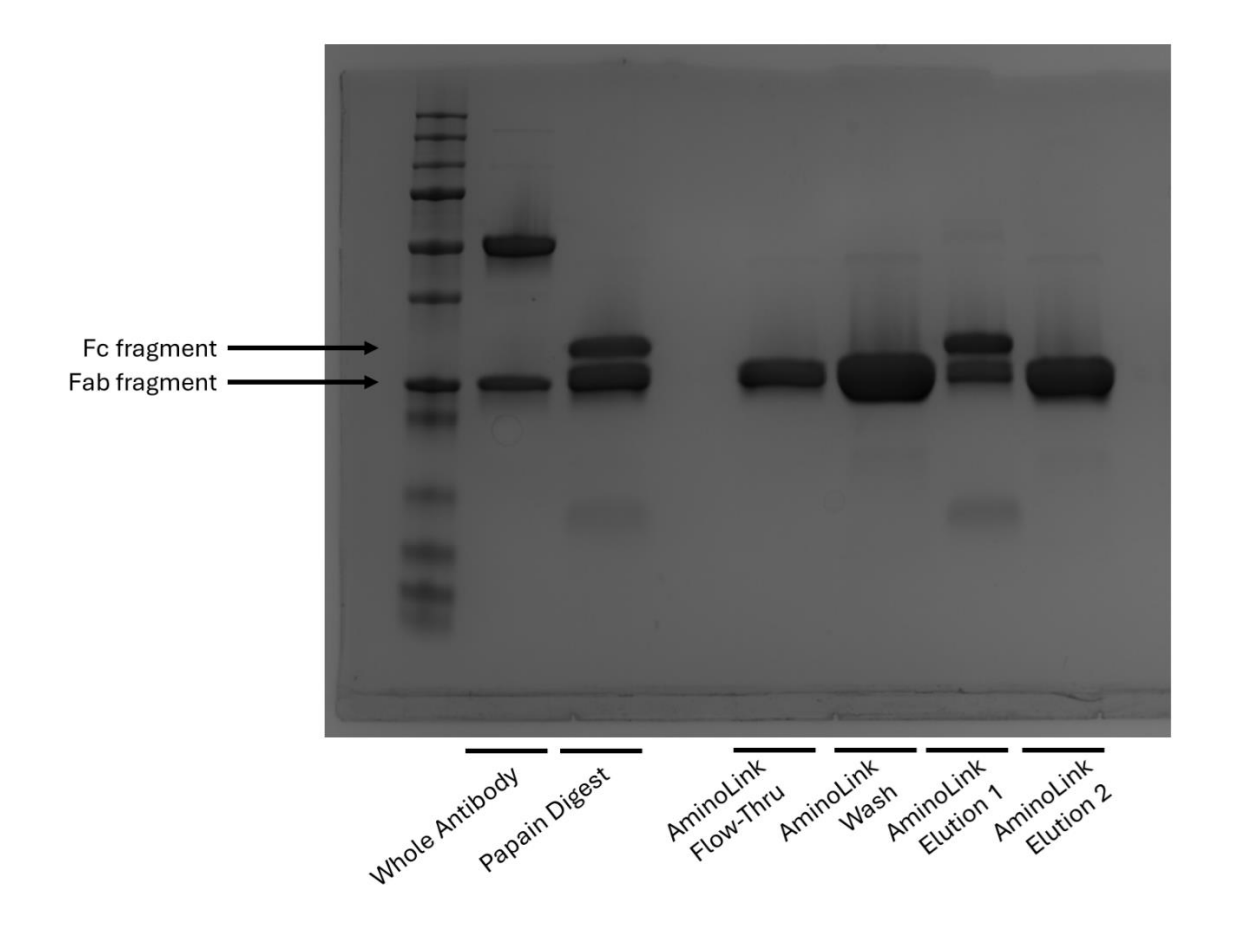


Figure 3.1. Reducing SDS-PAGE gel for TLR2 Fab purification. Whole antibody is shown being reduced into heavy and light chain fragments. Papain digestion fragments antibodies into Fc and Fab fragment portions. The AminoLink purification column has immobilized anti-Fc antibodies that remove the Fc fragments from the column flowthrough, and captured Fc is eluted using acid washing.

To characterize the Fabs functionally, we first determined that they bind to TLR2 using HEK 293 cells that were transfected to express human TLR2. We labeled both wild-type HEK 293 cells (which do not bear TLR2 natively) and HEK-Blue hTLR2 cells with our Fabs and used confocal microscopy to confirm only cells expressing TLR2 were labeled (**Figure 3.2**). For downstream applications, we also wanted to confirm the Fabs do not cross-react and bind to the Gram-positive bacteria *B. subtilis* and *S. griseus*. We incubated the Fabs with the bacteria for one hour before spinning the bacteria down, washing out the Fabs, and then used 650 nm

absorbance readings to confirm the 647 absorbance was not higher in the Fab-labeled samples (**Figure 3.2**).

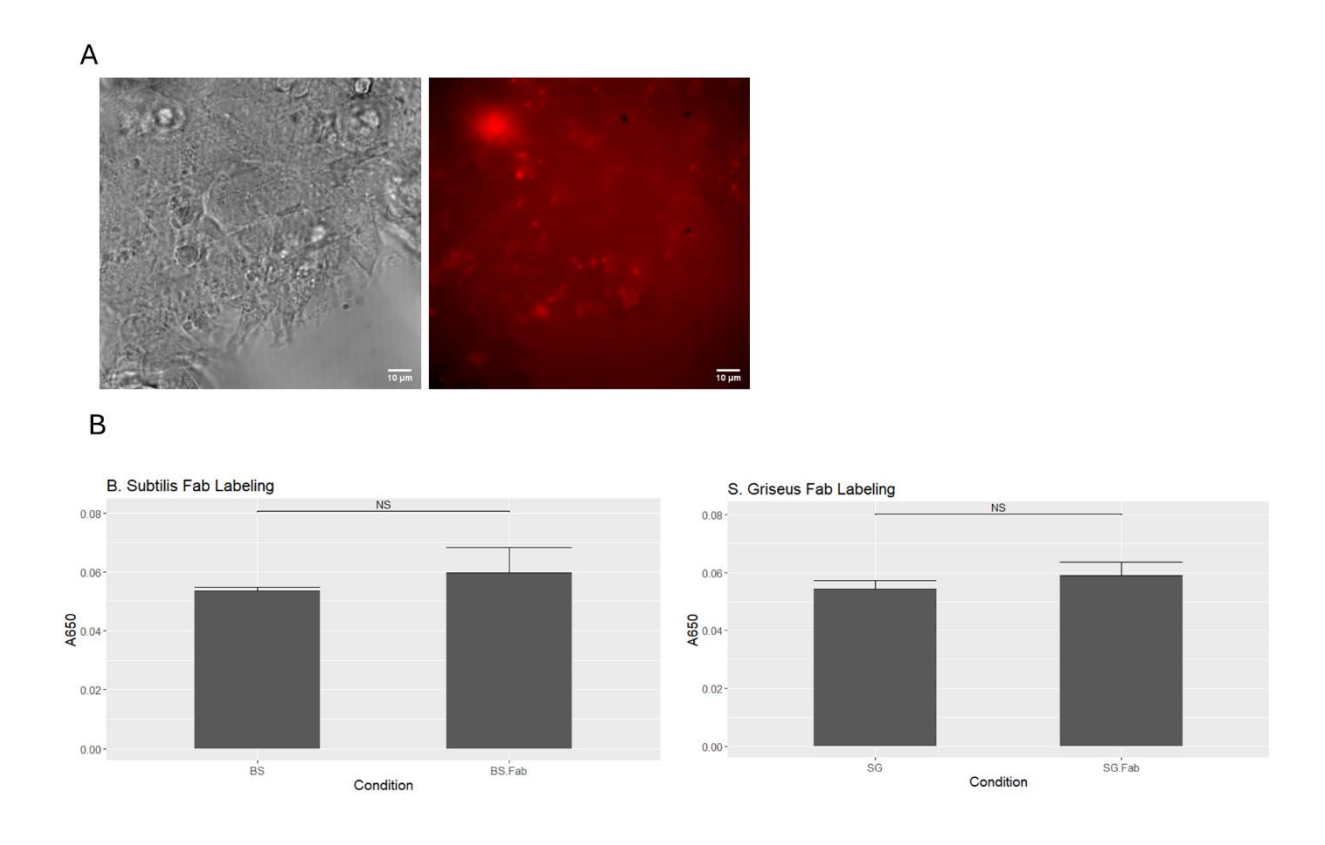


Figure 3.2. Characterizing binding of AF647-TLR2 Fab. (A) Fab fragment labeling of HEK-Blue hTLR2 cells at 1:50 dilution for 1 hour. (B) Fab fragment labeling of *B. subtilis* and *S. griseus* at 1:50 dilution for 1 hour shows no significant light absorbance at 650 nm.

We also used HEK-Blue hTLR2 cells to assess whether TLR2 signaling in cells is impacted by Fab labeling. After we incubated the HEK-Blue hTLR2 cells with Fab for an hour, when testing SEAP secretion from overnight incubation with 100 ng/mL LTA, there was no significant reduction in the ability for TLR2 to signal relative to unlabeled cells (**Figure 3.3**).

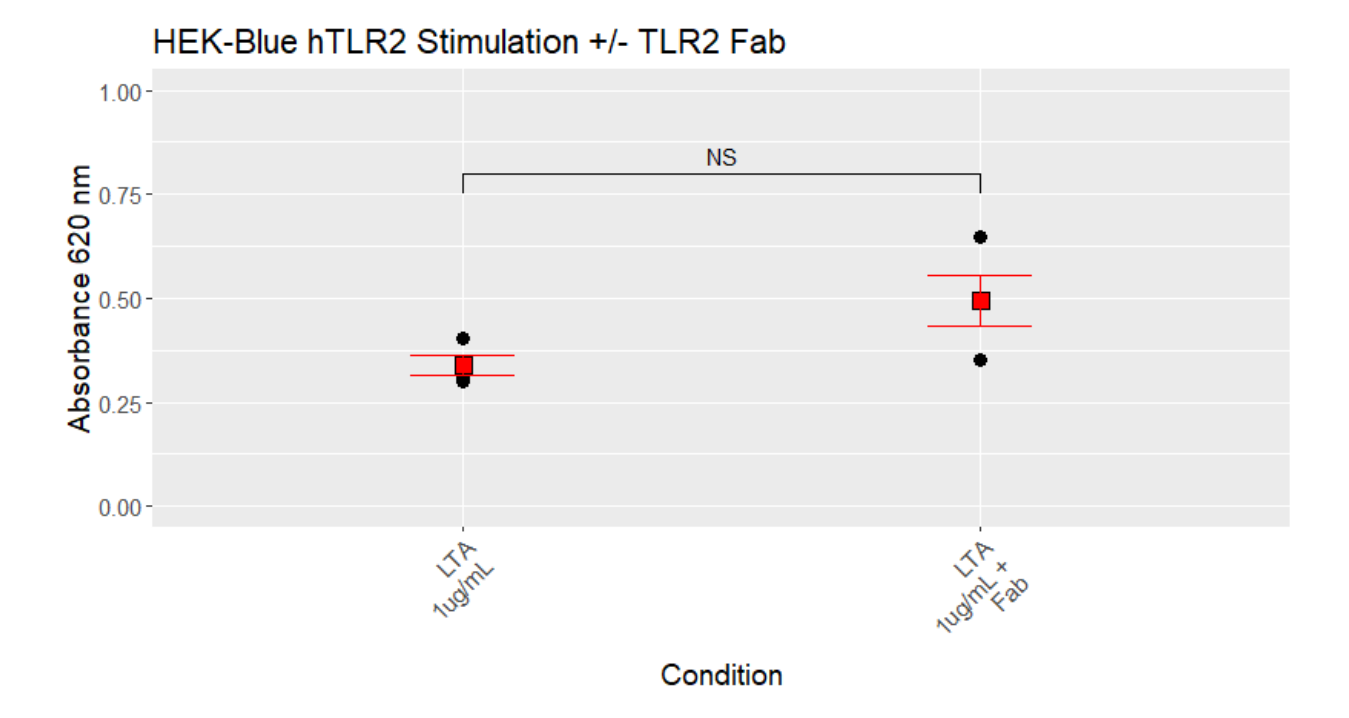


Figure 3.3. Assessing TLR2 function in the presence of TLR2 Fab fragment. TLR2-bearing HEK-Blue NFκB-SEAP reporter cells were dosed with 1 μ g/mL LTA overnight. SEAP secretion linked to NFκB transcription was measured the next day using a Quanti-Blue colorimetric assay. Mean absorbance at 620 nm between the samples are compared with a two-tailed t-test. NS p > 0.05.

To visualize the TLRs using LLSM, we immunolabeled TLR2 on RAW 264.7 macrophages with the AF647-conjugated-αTLR2 Fab fragment. We recorded 2-minute videos of cells with 100 z-stacks, 0.2 μm step size, 63x magnification, and 3 seconds per cell volume. Each resulting video contains ~3-6 cells, which amounts to ~60-300 labeled TLR2 clusters per video (**Figure 3.4**). After image processing, we then tracked the receptors in each video using Arivis Vision 4D software. Our analysis yielded 18 tracked 4D parameters for each receptor (**Table A.4.1**). For each experimental condition, we combined three different experiments' worth of tracked data for analysis. We then used R to further process the track data to reduce noise before comparing mean values for each parameter between resting and stimulated cell images using a two-sided Student's t-test. Parameters that highlighted significant TLR2

biophysics changes between stimulation regimens included track speed, track displacement, track area, and number of collisions between receptors (**Figure 3.4**).

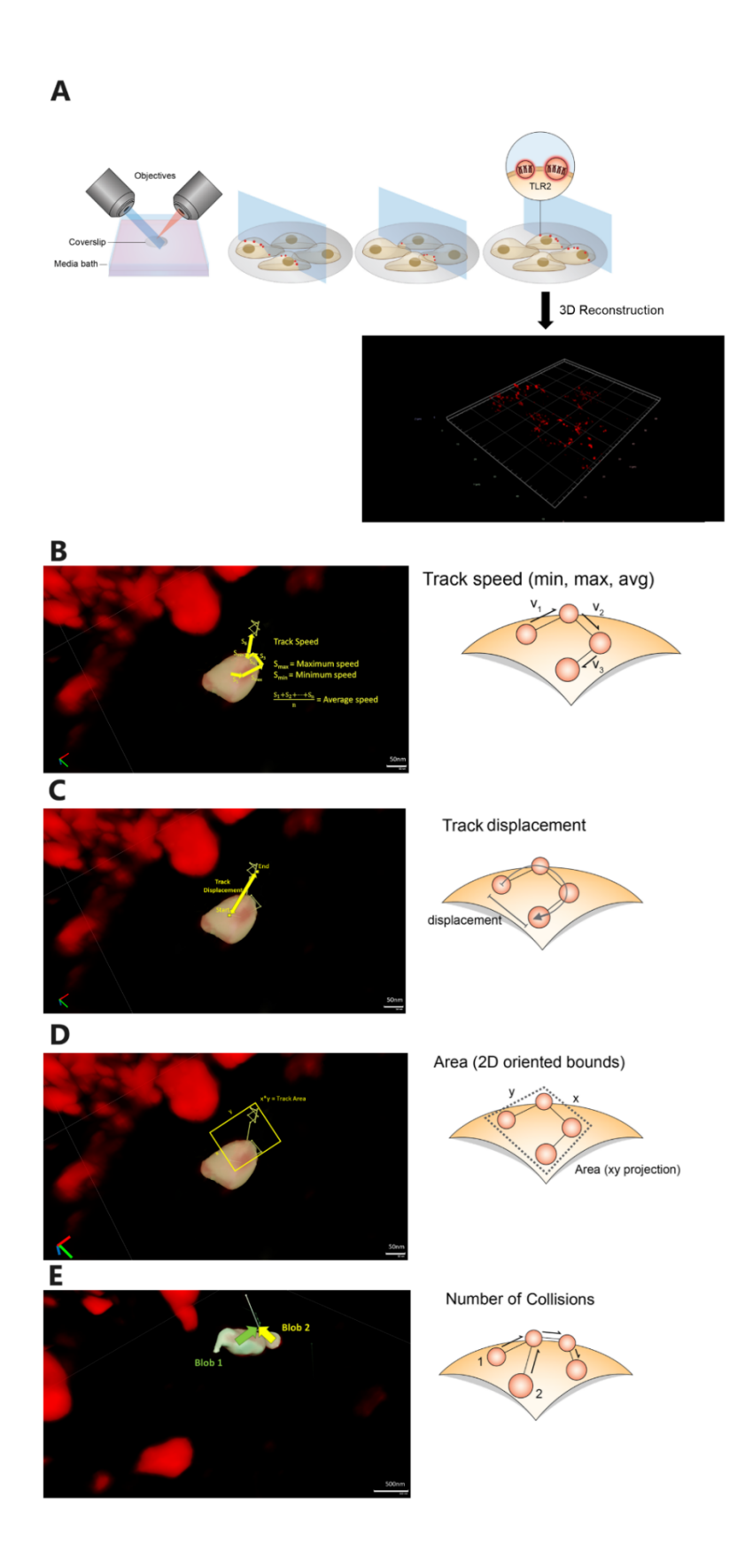


Figure 3.4. LLSM imaging of TLR2 on RAW 264.7 macrophages. (A) Diagram of lattice light sheet microscope imaging. Briefly, cells are placed on a coverslip immersed in a medium bath between the emission and collection objectives, then the light sheet is scanned through the sample. 3D reconstruction is carried out using ImageJ and Arivis 4D. Boxes in the reconstructed image are 10μm by 10μm. (B) Diagram of track speed metrics: Arivis measures the speed of each frame-to-frame segment of motion for each track and outputs the average speed, maximum speed, and minimum speed over the entire video. (C) Diagram of track displacement metric: Arivis computes the distance between the first position of the track and the final position of the track. (D) Diagram of track area metric: Arivis takes the area of the x and y components of motion for each track (i.e. in the plane of the coverslip). (E) Diagram of number of collisions: Arivis counts the number of times two blobs come together to form a new "fused" object. These objects may travel together for multiple frames and/or may split apart again.

3.5 Discussion

There is much evidence that studying receptor biophysics and dynamics can impart vital understanding of the way biological systems operate, and microscopy offers a clear lens through which to view and quantify these essential functions. Here, we develop and characterize a Fab fragment-based TLR2 label that can be used to image TLR2 dynamics on macrophages with high-speed live imaging techniques. We have demonstrated that the label is specific for TLR2, does not bind to Gram-positive bacteria that might be used as stimulants, and is minimally invasive in terms of TLR2-dependent NF κ B activation.

Our label has a few major advantages: namely, it is easy to make and use, and its monovalence allows for an ideal tracking scenario where receptors are not bound together by the label. It is worth noting, however, that we are unable to assess any molecular perturbation to the TLR2-macrophage system as a result of attaching a fluorescent dye to it. At about 50 kDa, the Fab fragment is around half of the size of a single TLR2 (~95 kDa¹⁵). One might imagine that attaching a Fab to the TLR could impact the receptor's motion or sterics. Indeed, labeling perturbations on biological systems is a subject of some discourse in the microscopy field^{16,17}. On the other hand, it is currently standard in the field to use Fabs or whole antibodies for labeling given, for example, methods in recent biological tracking studies in T cells^{18,19,20,21}.

Additionally, multiple studies have been conducted on the mechanical adhesion and tether forces in macrophage membranes that report on the order of piconewton forces exerted by the cells^{22,23}. These forces are several orders of magnitude larger than conservative estimates of drag forces on a Fab fragment in aqueous space, which indicates that the Fab fragment likely has minimal impact the membrane-induced motion of TLRs. Still, future development work might be aimed at further minimizing the impacts of the TLR label on the biological environment by using smaller labels or developing label-free methodology for tracking these receptors.

3.6 References

- 1. Bunnell, S. C., Hong, D. I., Kardon, J. R., Yamazaki, T., McGlade, C. J., Barr, V. A., & Samelson, L. E. (2002). T cell receptor ligation induces the formation of dynamically regulated signaling assemblies. *The Journal of cell biology*, *158*(7), 1263–1275. https://doi.org/10.1083/jcb.200203043
- 2. Saito, T., & Yokosuka, T. (2006). Immunological synapse and microclusters: the site for recognition and activation of T cells. *Current opinion in immunology*, *18*(3), 305–313. https://doi.org/10.1016/j.coi.2006.03.014
- 3. Yokosuka, T., & Saito, T. (2010). The immunological synapse, TCR microclusters, and T cell activation. *Current topics in microbiology and immunology*, *340*, 81–107. https://doi.org/10.1007/978-3-642-03858-7_5
- 4. Campi, G., Varma, R., & Dustin, M. L. (2005). Actin and agonist MHC-peptide complex-dependent T cell receptor microclusters as scaffolds for signaling. *The Journal of experimental medicine*, 202(8), 1031–1036. https://doi.org/10.1084/jem.20051182
- 5. Huang, J., Brameshuber, M., Zeng, X., Xie, J., Li, Q. J., Chien, Y. H., Valitutti, S., & Davis, M. M. (2013). A single peptide-major histocompatibility complex ligand triggers digital cytokine secretion in CD4(+) T cells. *Immunity*, *39*(5), 846–857. https://doi.org/10.1016/j.immuni.2013.08.036
- 6. DeMond, A. L., Mossman, K. D., Starr, T., Dustin, M. L., & Groves, J. T. (2008). T cell receptor microcluster transport through molecular mazes reveals mechanism of translocation. *Biophysical journal*, *94*(8), 3286–3292. https://doi.org/10.1529/biophysj.107.119099
 7. Crites, T. J., Padhan, K., Muller, J., Krogsgaard, M., Gudla, P. R., Lockett, S. J., & Varma, R. (2014). TCP, Microclusters are exist and contain melecules processory for TCP, signal.
- (2014). TCR Microclusters pre-exist and contain molecules necessary for TCR signal transduction. *Journal of immunology (Baltimore, Md. : 1950)*, *193*(1), 56–67. https://doi.org/10.4049/jimmunol.1400315
- 8. Inoue, M., & Shinohara, M. L. (2014). Clustering of pattern recognition receptors for fungal detection. *PLoS pathogens*, 10(2), e1003873. https://doi.org/10.1371/journal.ppat.1003873
- 9. Aaron, J. S., Carson, B. D., & Timlin, J. A. (2012). Characterization of differential Toll-like receptor responses below the optical diffraction limit. *Small (Weinheim an der Bergstrasse, Germany)*, 8(19), 3041–3049. https://doi.org/10.1002/smll.201200106
- 10. Li, M., Wang, H., Li, W., Xu, X. G., & Yu, Y. (2020). Macrophage activation on "phagocytic synapse" arrays: Spacing of nanoclustered ligands directs TLR1/2 signaling with an intrinsic limit. *Science advances*, 6(49), eabc8482. https://doi.org/10.1126/sciadv.abc8482
- 11. Li, M., & Yu, Y. (2021). Innate immune receptor clustering and its role in immune regulation. *Journal of cell science*, *134*(4), jcs249318. https://doi.org/10.1242/jcs.249318

- 12. Guven-Maiorov, E., Keskin, O., Gursoy, A., VanWaes, C., Chen, Z., Tsai, C. J., & Nussinov, R. (2015). The Architecture of the TIR Domain Signalosome in the Toll-like Receptor-4 Signaling Pathway. *Scientific reports*, 5, 13128. https://doi.org/10.1038/srep13128
- 13. Rosenberg, J., Cao, G., Borja-Prieto, F., & Huang, J. (2020). Lattice Light-Sheet Microscopy Multi-dimensional Analyses (LaMDA) of T-Cell Receptor Dynamics Predict T-Cell Signaling States. *Cell systems*, *10*(5), 433–444.e5. https://doi.org/10.1016/j.cels.2020.04.006
- 14. Nimmerjahn, F., & Ravetch, J. V. (2008). Fcgamma receptors as regulators of immune responses. *Nature reviews. Immunology*, 8(1), 34–47. https://doi.org/10.1038/nri2206
- 15. Shi, M., Yue, Y., Ma, C., Dong, L., & Chen, F. (2022). Pasteurized *Akkermansia muciniphila* Ameliorate the LPS-Induced Intestinal Barrier Dysfunction via Modulating AMPK and NF-κB through TLR2 in Caco-2 Cells. *Nutrients*, *14*(4), 764. https://doi.org/10.3390/nu14040764
- 16. Ghosh, B., & Agarwal, K. (2023). Viewing life without labels under optical microscopes. *Communications biology*, *6*(1), 559. https://doi.org/10.1038/s42003-023-04934-8
- 17. Grimm, J. B., & Lavis, L. D. (2022). Caveat fluorophore: an insiders' guide to small-molecule fluorescent labels. *Nature methods*, 19(2), 149–158. https://doi.org/10.1038/s41592-021-01338-6
- 18. Chang, V. T., Fernandes, R. A., Ganzinger, K. A., Lee, S. F., Siebold, C., McColl, J., Jönsson, P., Palayret, M., Harlos, K., Coles, C. H., Jones, E. Y., Lui, Y., Huang, E., Gilbert, R. J. C., Klenerman, D., Aricescu, A. R., & Davis, S. J. (2016). Initiation of T cell signaling by CD45 segregation at 'close contacts'. *Nature immunology*, *17*(5), 574–582. https://doi.org/10.1038/ni.3392
- 19. Ghosh, S., Di Bartolo, V., Tubul, L., Shimoni, E., Kartvelishvily, E., Dadosh, T., Feigelson, S. W., Alon, R., Alcover, A., & Haran, G. (2020). ERM-Dependent Assembly of T Cell Receptor Signaling and Co-stimulatory Molecules on Microvilli prior to Activation. *Cell reports*, *30*(10), 3434–3447.e6. https://doi.org/10.1016/j.celrep.2020.02.069
- 20. Velas, L., Brameshuber, M., Huppa, J. B., Kurz, E., Dustin, M. L., Zelger, P., Jesacher, A., & Schütz, G. J. (2021). Three-Dimensional Single Molecule Localization Microscopy Reveals the Topography of the Immunological Synapse at Isotropic Precision below 15 nm. *Nano letters*, 21(21), 9247–9255. https://doi.org/10.1021/acs.nanolett.1c03160
- 21. Brameshuber, M., Kellner, F., Rossboth, B. K., Ta, H., Alge, K., Sevcsik, E., Göhring, J., Axmann, M., Baumgart, F., Gascoigne, N. R. J., Davis, S. J., Stockinger, H., Schütz, G. J., & Huppa, J. B. (2018). Monomeric TCRs drive T cell antigen recognition. *Nature immunology*, *19*(5), 487–496. https://doi.org/10.1038/s41590-018-0092-4

- 22. Zhao, Y., Mahajan, G., Kothapalli, C. R., & Sun, X. L. (2019). Sialylation status and mechanical properties of THP-1 macrophages upon LPS stimulation. *Biochemical and biophysical research communications*, *518*(3), 573–578. https://doi.org/10.1016/j.bbrc.2019.08.089
- 23. Winer, B. Y., Settle, A. H., Yakimov, A. M., Jeronimo, C., Lazarov, T., Tipping, M., Saoi, M., Sawh, A., Sepp, A. L., Galiano, M., Wong, Y. Y., Perry, J. S. A., Geissmann, F., Cross, J., Zhou, T., Kam, L. C., Pasoli, H. A., Hohl, T., Cyster, J. G., Weiner, O. D., ... Huse, M. (2023). Plasma membrane abundance dictates phagocytic capacity and functional crosstalk in myeloid cells. *bioRxiv: the preprint server for biology*, 2023.09.12.556572. https://doi.org/10.1101/2023.09.12.556572

CHAPTER 4: LATTICE LIGHT SHEET MICROSCOPY REVEALS A ROLE OF BIOPHYSICAL STIMULANT DIVERSITY ON MACROPHAGE TLR2 RESPONSES

4.1 Summary

Macrophages are an essential early immune cell subset that physically interface with pathogens and their environment using pattern recognition receptors to sense threats. There is growing evidence that the physical organization and dynamics of macrophage receptors in space informs downstream cellular activation and the immune response; however, the biophysical behaviors of immune cells upon first contact with stimuli are poorly understood due to lack of direct observation of these receptors. Here, we used lattice light sheet microscopy to image macrophages with Fab-fragment-labeled TLR2 and track the receptors' motion on the cell membrane. We observed that TLR2 speed increases upon single-ligand LTA stimulation and decreases upon Gram-positive bacterial stimulation in a TLR2-dependent manner, and these changes alter the cells' cytokine secretion resulting from stimulation with different bacteria. Our findings highlight that macrophages differentiate between different stimuli and accordingly coordinate their biophysical response, which helps inform understanding about the innate immune response and novel stimulus design.

4.2 Introduction

Macrophages are a first line of immune defense that are responsible for pathogen detection, targeted response, and communication with other effectors for protection^{11,12}. For many of these functions, macrophage receptors physically contact pathogen-associated ligands¹³, the extracellular matrix¹⁴, and other immune cells¹⁵. Prior work in our lab and others shows that the physical basis and geometry of these contacts is important for robust activation of cells¹⁶ and

for informing the immune response when there are multiple signals present. For example, organizing multiple Toll-like receptor (TLR) agonists in space via covalent linkages or segregating them on beads causes macrophages to integrate and process signals from those agonists differently from if they are left free in solution 17,18. We have also found using agonist-coated microparticles that different densities and numbers of agonists bound on a core structure cause different profiles in intensity of immune activation in macrophages 19. Prior work has also shown that bacterial biophysics (e.g. motility) and ligand structure impacts intensity of macrophage responses, cluster size of responding receptors, phagocytic capacity, and bacterial infectivity 20,21,22. However, despite the wealth of evidence that the biophysical context of macrophage stimulation informs immune responsiveness, the biophysics of macrophage receptor activity upon ligand contact remains poorly understood due to limited direct observation of receptor dynamics.

Here we use lattice light sheet microscopy (LLSM) to directly observe macrophage TLR2 in macrophages responding to molecular LTA and bacterial stimuli with different shapes and biophysical properties. LLSM utilizes a structured light sheet to illuminate a sample while collecting imaging data perpendicular to the light sheet²³. The result of this imaging strategy is rapid image acquisition with high axial resolution, high speed, low photobleaching, whole volume imaging that is especially optimized for live biological applications^{1,23,24}. Using LLSM, we collected videos of TLR2 on live macrophages resting or post-stimulation and then computationally characterized their physical behavior and how these behaviors changed upon activation with stimulants of varied biophysical characteristics. Our imaging reveals that macrophage TLR2 speed increases while responding to molecular LTA and decreases while responding to bacteria in a TLR2-dependent manner and that these speed changes cause changes

in the immunological response. These results indicate that macrophages coordinate their biophysical responses as one way to respond differentially to different types of stimuli.

4.3 Materials and Methods

TLR2 Antibody Digestion

Whole anti-TLR2 antibodies (clone 6C2, eBioscience) were digested via papain digestion using a Pierce Fab Preparation Kit (Thermo Scientific). 600 µg of antibody was spin concentrated in 10 kDa MWCO microcentrifuge spin filters (Millipore). The concentrated sample was brought up to 500 µL in the cystine-HCl Fab digestion buffer provided with the Fab preparation kit. This sample was desalted using the kit spin desalting column protocol and then incubated with the kit immobilized papain resin for four hours at 37°C with end-over-end mixing. The digested sample was spun out of the column and stored for downstream purification. Digestion was confirmed using SDS-PAGE gel electrophoresis.

TLR2 Fab Purification

Fab purification was carried out using an AminoLink Plus Immobilization Kit (Thermo Scientific) conjugated with anti-Rat IgG Fc antibodies (Sigma-Aldritch). Conjugation was accomplished following the kit protocol with pH 10 Coupling Buffer and overnight incubations where relevant. Affinity purification was also carried out per protocol with the digested antibody sample being incubated in the affinity column for 45 minutes. Purification was confirmed using SDS-PAGE gel electrophoresis.

TLR2 Fab Fragment AlexaFluor 647 Labeling

The purified Fab fragments were spin filtered and brought up to 1 mg/mL concentration in PBS via NanoDrop (ND-2000c, Thermo Scientific) reading. The Fabs were then labeled

using an Alexa Fluor 647 Microscale Labeling Kit per kit instructions with MR = 15, MW = 50,000 Da, and a 30-minute incubation in with end-over-end mixing in the AF 647 reaction mixture. Degree of labeling was assessed using NanoDrop measurements per kit instructions. The Fabs were finally passed through a $0.22~\mu m$ syringe filter to sterilize them after the cutting and labeling procedure.

Immortalized Cell Culture

RAW 264.7, RAW 264.7 G9 clone³, and HEK-Blue hTLR2 (Invivogen) cells were all maintained in DMEM (Life Technologies) supplemented with 10% fetal bovine serum (FBS) (Life Technologies) and 1% antibiotic-antimycotic (Life Technologies) at 37°C and 5% CO₂ in T75 cell culture flasks.

Bacterial Culture

B. subtilis was maintained in tryptic soy broth (BD Bacto, Fisher Scientific) in an incubator at 37°C shaking at 225 RPM. *S. griseus* was maintained in tryptic soy broth in an incubator at 28°C shaking at 225 RPM.

BMDM Differentiation

Monocytes were harvested from the femurs of C57BL/6 mice (Jackson Laboratory) and were differentiated into macrophages by incubating them in supplemented culture medium: RPMI 1640 (Life Technologies), 10% heat inactivated fetal bovine serum (HI-FBS), 2×10^{-3} M L-glutamine (Life Technologies), antibiotic-antimycotic (1×) (Life Technologies), and 10% MCSF (mycoplasma free L929 supernatant) for 5 days at 37°C and 5% CO₂.

Cell Preparation for LLSM

RAW 264.7 cells were scraped from their flasks and resuspended in DMEM supplemented with 10% HI-FBS and 1% antibiotic-antimycotic. This suspension was beaded in

 $20~\mu L$ droplets on top of #1.5 5mm round German glass coverslips (World Precision Instruments) in individual wells of a 48 well plate. The beads were left to incubate at 37°C and 5% CO_2 for at least 15 minutes before filling the wells of the 48 well tray with 200 μL medium and letting incubate overnight.

The next day, the medium was aspirated from the wells and replaced with $100~\mu L$ of CO_2 independent medium (Gibco, Thermo Fisher) supplemented with 10% HI-FBS (LLSM medium). If relevant, OxPAPC resuspended in LLSM medium to a final concentration of $111~\mu g/mL$ was added to the wells and let to incubate for 1 hour at $37^{\circ}C$ on an orbital rocker. After (or instead) of this step, the OxPAPC was aspirated and a 1:50 dilution of labeled Fab fragments in $100~\mu L$ of LLSM medium was added to the cells and let to incubate for 1 hour at $37^{\circ}C$ on an orbital rocker. The Fab medium was then aspirated and replaced with fresh LLSM medium.

Stimulant Preparation for LLSM

LTA isolated from *B. subtilis* (LTA-BS, Invivogen) was resuspended in LLSM medium to a concentration of 100 ng/mL in 6 mL total.

The optical density of the *B. subtilis* and *S. griseus* were measured at 600 nm (OD_{600}) using the NanoDrop. 1-2 mL of each culture was transferred to a 15 mL centrifuge tube and diluted to a final volume x OD_{600} of 0.6. BactoView Live Green stain (Biotium) was added to each at 1:500. The bacteria were incubated at 37°C with end-over-end mixing for 1 hour. The bacteria were then pelleted at 9000 x g for 15 minutes, and the supernatant was removed and replaced with LLSM medium. This centrifugation was repeated two more times, and the final volume of LLSM medium added was 6 mL for a OD_{600} of 0.1.

LLSM Procedure

LLSM was carried out on a 3i Lattice LightSheet Microscope with acquisition in 3i's SlideBook software. The LLSM medium bath was filled with LLSM media warmed to 37°C. A coverslip with labeled RAW 264.7 cells was adhered to the LLSM's sample holder using vacuum grease and then placed on the LLSM. The resting cells were imaged at 20 ms exposure time and 10 mW/50 percent 647 laser power with 100 z-stacks and 0.2 µm step size for a 20 acquisition time series. The LLSM medium bath was then aspirated and medium supplemented with stimulants as described above was added. The cells were incubated for 30 minutes with the stimulants before the imaging experiment was repeated. This procedure was repeated for three coverslips per experiment.

LLSM Image Processing

Each image stack was deskewed using SlideBook's batch deskewing function and exported as .TIFFs. Images were then imported and stacked in Fiji, Gaussian blurred with r = 0.7, despeckled, and background subtracted using a rolling ball radius of 100 pixels. Images were then deconvolved using a Fiji implementation of Brian Northan's YacuDecu GPU deconvolution algorithm with a theoretical PSF calculated using the Richardson-Lucy algorithm²⁶. The deconvolved images were then rotated in Fiji to place the coverslip in the xy-plane.

Deconvolved and rotated images were then imported into Arivis Vision4D software for tracking. Briefly, the tracking algorithm consists of a Blob Finder step that identifies spots and a Tracking step that calculates trajectories from an expected Brownian Motion motion type and computationally derived max distance. The Tracker also tracks fusions and automatically deletes tracks that do not have more than one blob in them across the time series and then tracks with

relevant track parameters are exported to a spreadsheet. All tracked parameters are in Table A.3.1.

R Analysis

After export from Arivis Vision4D, track spreadsheets were imported to R. All the track data were filtered to remove columns with missing and 0 values then filtered again to only include tracks present for the whole time series to avoid artifacts. All data tables for conditions were bound together, and Student's t-tests for each parameter were carried out between resting vs. stimulated data sets for each stimulus. The resulting p-values were corrected for multiple hypotheses via a Benjamini-Hochberg correction.

HEK-Blue hTLR2 Assay

HEK-Blue hTLR2 cells (Invivogen) were scraped from their flasks and resuspended in DMEM supplemented with 10% HI-FBS and 1% antibiotic-antimycotic. 50,000 HEK-Blue hTLR2 cells per well were added to a 96 well plate at 200 µL per well and let to incubate overnight at 37°C and 5% CO₂.

The next day, *B. subtilis* and *S. griseus* cultures were mixed with DMEM + 10% HI-FBS to desired concentrations. The medium in the HEK-Blue cells was aspirated and replaced with 200 µL per well of bacterial supplemented medium and left to incubate for 2 hours at 37°C and 5% CO₂. After incubation, the HEK-Blue cells were washed four times with 200µL DMEM + 10% HI-FBS + 1% Antibiotic-antimycotic medium and left to incubate overnight at 37°C and 5% CO₂.

The next day, the cells were tested for SEAP activity in the supernatant using a QUANTI-Blue (InvivoGen) assay per protocol with absorbance measured at 620 nm using a Multiskan FC plate reader (Thermo Scientific).

IL-6 and TNFα ELISAs

Primary BMDMs were scraped from their dishes using 5×10^{-3} m EDTA in PBS and resuspended in RPMI 1640 (Life Techologies) with 10% HI-FBS and 1% antibiotic-antimycotic. The cells were replated at 100,000 cells per well in a 96 well plate with 200 μ L per well and let to incubate overnight at 37°C and 5% CO₂.

The next day, *B. subtilis* and *S. griseus* cultures were mixed with RPMI + 10% HI-FBS to desired concentrations. The medium in the BMDMs was aspirated and replaced with 200 μL per well of bacterial supplemented medium and left to incubate for 2 hours at 37°C and 5% CO₂. After incubation, the BMDMs were washed four times with 200μL RPMI + 10% HI-FBS + 1% antibiotic-antimycotic medium and left to incubate overnight at 37°C and 5% CO₂.

The next day, the cells were tested for cytokine secretion in the supernatant using ELISA MAX Mouse Cytokine ELISA kits (BioLegend) per protocol with absorbance measured at 450 nm using a Multiskan FC plate reader (Thermo Scientific). Statistical analysis of the ELISA results was performed in R by fitting a 4-parameter logistic model to the standard curve data to interpret the experimental cytokine levels.

Mathematical Analysis of Physical Contributions of TLR2

Suppose the total secretion of a particular cytokine by a cell due to agonist stimulation can be expressed as:

$$S_{Ag} = NonTLR2/4_{Ag} + TLR2/4_{Ag} + TLR2/4_{Phys,Ag}$$
 (1)

Where S_{Ag} is the cytokine level, $NonTLR2/4_{Ag}$ is the cytokine secretion due to non-TLR2 or TLR4 sources, $TLR2/4_{Ag}$ is the cytokine secretion due to traditional activation of the TLR2 and TLR4 pathway due to binding the agonist, and $TLR2/4_{Phys,Ag}$ is the cytokine secretion due to physical changes of TLR2 and TLR4 due to the agonist.

OxPAPC is known to block agonist binding to TLR2/4, and our LLSM experiments show ablation of TLR2 physical changes due to agonist stimulation. Therefore, we suppose cytokine levels while stimulating a cell dosed with OxPAPC can be expressed as:

$$S_{Aq,OxPAPC} = NonTLR2/4_{Aq} \tag{2}$$

Suppose we then select a concentration of *B. subtilis* (BS) and *S. griseus* (SG) to have equal TLR2/4 signaling through traditional receptor ligation (e.g. by using HEK TLR2 reporter cells to measure cellular activation due to both stimulus), i.e.:

$$HEK TLR2/4_{BS} = HEK TLR2/4_{SG} = TLR2/4$$
(3)

Where $HEK\ TLR2/4_{BS}$ is the reporter cell activation level due to B. subtilis stimulation and $HEK\ TLR2/4_{SG}$ is the reporter cell activation level due to S. griseus stimulation. Since the level of activation through the receptors is dependent only on the number of agonist/receptor interactions on the cell, we expect that these two quantities will be equal as long as two cells of the same type are stimulated with these concentrations of agonists because the number of agonists and number of receptors should be the conserved in the comparison.

Given this assumption, for the above selected concentrations of BS and SG, we may rewrite eq (1) as:

$$S_{BS} = NonTLR2/4_{BS} + TLR2/4 + TLR2/4_{Phys,BS}$$
 (4)

$$S_{SG} = NonTLR2/4_{SG} + TLR2/4 + TLR2/4_{Phys,SG}$$
 (5)

Substituting eq (2) into these and subtracting the two yields the following form:

$$S_{BS} - S_{SG} = S_{BS,Ox} + TLR2/4 + TLR2/4_{Phys,BS} - S_{SG,Ox} - TLR2/4 - TLR2/4_{Phys,SG}$$
 (6)

Finally, canceling the *TLR*2/4 term and rearranging gives an expression for the difference in TLR2/4 physical contributions from the two different bacteria on cytokine signaling:

$$S_{BS} - S_{SG} - S_{BS,Ox} + S_{SG,Ox} = TLR2/4_{Phys,BS} - TLR2/4_{Phys,SG}$$
 (7)

This form implies that if the left-hand side calculated value is non-zero, then the physical effect on TLR2/4 signaling is different for the two bacteria.

4.4 Results

4.4.1 Single Ligand Stimulation Causes a Speed Increase in TLR2 Tracks

To assess how TLR2 motion changes in a stimulated macrophage versus a resting one, we used LLSM to image a macrophage that was stimulated with lipoteichoic acid (LTA)—a TLR2 agonist isolated from gram-positive bacteria². After taking an image of the cells at rest, we swapped the culture medium in the LLSM bath for medium supplemented with 100ng/mL LTA. The cells incubated in this medium for 30 minutes before we imaged again. We confirmed that this stimulation activates cells in a separate LLSM imaging experiment using a RAW 264.7 mutant cell line with GFP-tagged NFκB (RAW G9 cells)³. Under the described stimulation regimen, we saw robust nuclear translocation of NFκB at 30 minutes (Figure A.4.1).

After stimulating with LTA, we saw an increase of 9.07 ± 2.14 % in the average speed of TLR2 tracks relative to resting average track speeds (**Figure 4.1**). We also saw maximum track speeds increase in the stimulated cells by 16.7 ± 5.02 % while there was no significant change in minimum track speeds versus resting. Additionally, we found that track displacement increased 25.6 ± 6.57 % in cells post-stimulation. There were no significant differences between stimulated and resting for track area and number of collisions. Because LTA only activates TLR2 in the cells²⁵, we hypothesized that any changes in TLR2 dynamics are a direct consequence of TLR2 activation. To confirm this, we treated the cells with a 111 μ g/mL dose of oxidized PAPC (oxPAPC), a competitive TLR2 inhibitor, for one hour before imaging⁴. After blocking TLR2 signals, we saw no differences in track speeds, displacement, area, or collisions post-stimulation

with LTA (**Figure 4.1**). Taken together, these results indicate that single-molecule LTA stimulation causes macrophages' TLR2 to move faster in a TLR2 signaling-dependent manner.

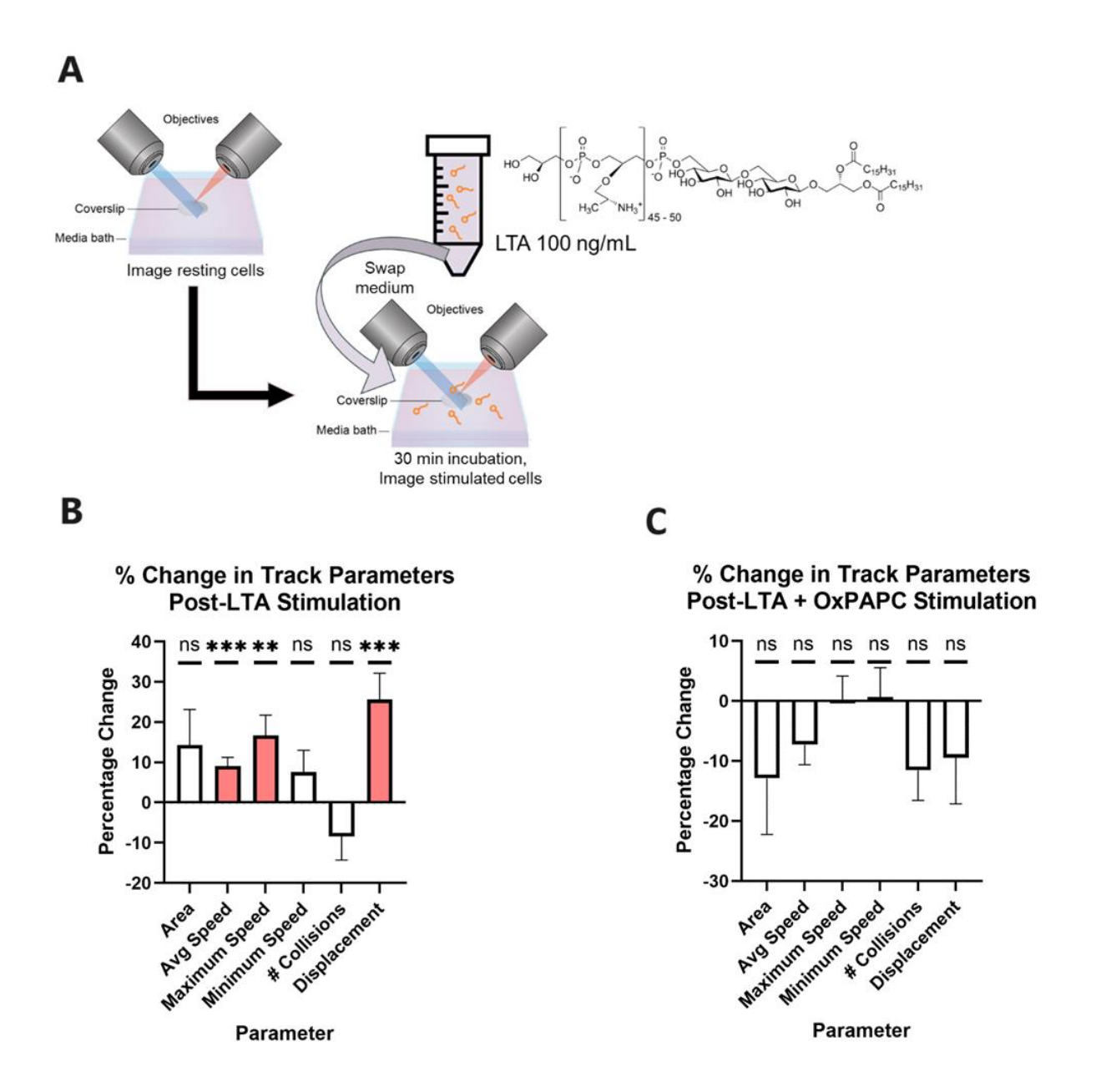


Figure 4.1. Percentage changes in track metrics from resting after stimulating with LTA. (A) Three groups of cells were imaged at rest before being dosed on the microscope with 100 ng/mL LTA for 30 minutes, then the same coverslip (but three different groups of cells) was imaged again. (B) Percentage change in mean track parameters after LTA stimulation when compared to resting. (C) The same experiment was performed with a 1 hour pre-treatment of the macrophages with 111 ng/mL OxPAPC before imaging. Means for each parameter in resting vs. stimulated cells are compared with a two-tailed t-test. NS p > 0.05, ** p < 0.01, *** p < 0.001

4.4.2 Bacterial Stimulation Causes a Speed Decrease in TLR2 Tracks

We then sought to assay a more biologically relevant stimulus by using live grampositive bacteria to stimulate the macrophages instead of soluble LTA. Among many other innate immune receptor signals from gram-positive bacteria, TLR2 plays a role recognizing bacterial cell wall components such as LTA and peptidoglycans⁵. We selected two bacteria with very different physical properties to see how TLR2 dynamics might be affected by size, shape, and motility. *B. subtilis* is a small, rod-shaped cell (2-6µm long, ~1µm diameter) that moves via flagellar motor^{6,7}. *S. griseus*, on the other hand, is a large, segmented filamentous bacterium (10+ µm long, ~1 µm diameter) that does not have intrinsic motility⁸. After imaging resting cells, we dosed the cells for 30 minutes with medium containing either bacterium (0.1 optical density measured at 600 nm), then imaged the stimulated cells. We again confirmed activation of the macrophages at these doses of bacteria using a separate G9 cell experiment (Figure A.4.1).

Unlike with the LTA stimulation, after *B. subtilis* stimulation we saw a decrease of $6.77 \pm 2.29\%$ in the average speed of TLR2 tracks relative to resting (**Figure 4.2**). We also saw minimum track speed reduction of $19.3 \pm 5.19\%$ for *B. subtilis* post-stimulation although we saw no maximum track speed change when dosing with these bacteria. Additionally, we found that track area decreased $33.9 \pm 6.91\%$, and the number of collisions of TLR2 tracks decreased $28.9 \pm 5.73\%$ post-stimulation. There was no significant difference between stimulated and resting for track displacement. We, again, confirmed that OxPAPC dosage ablates these changes (**Figure 4.2**). These data suggest that bacterial stimulation—specifically with *B. subtilis*—cause TLR2 behaviors associated with decreased speed and motion and that these changes depend on TLR2 activation. Importantly, the OxPAPC experiment shows that these speed changes require TLR2

activation even in contexts where the macrophage receives other, non-TLR2 stimulatory signaling from bacteria.

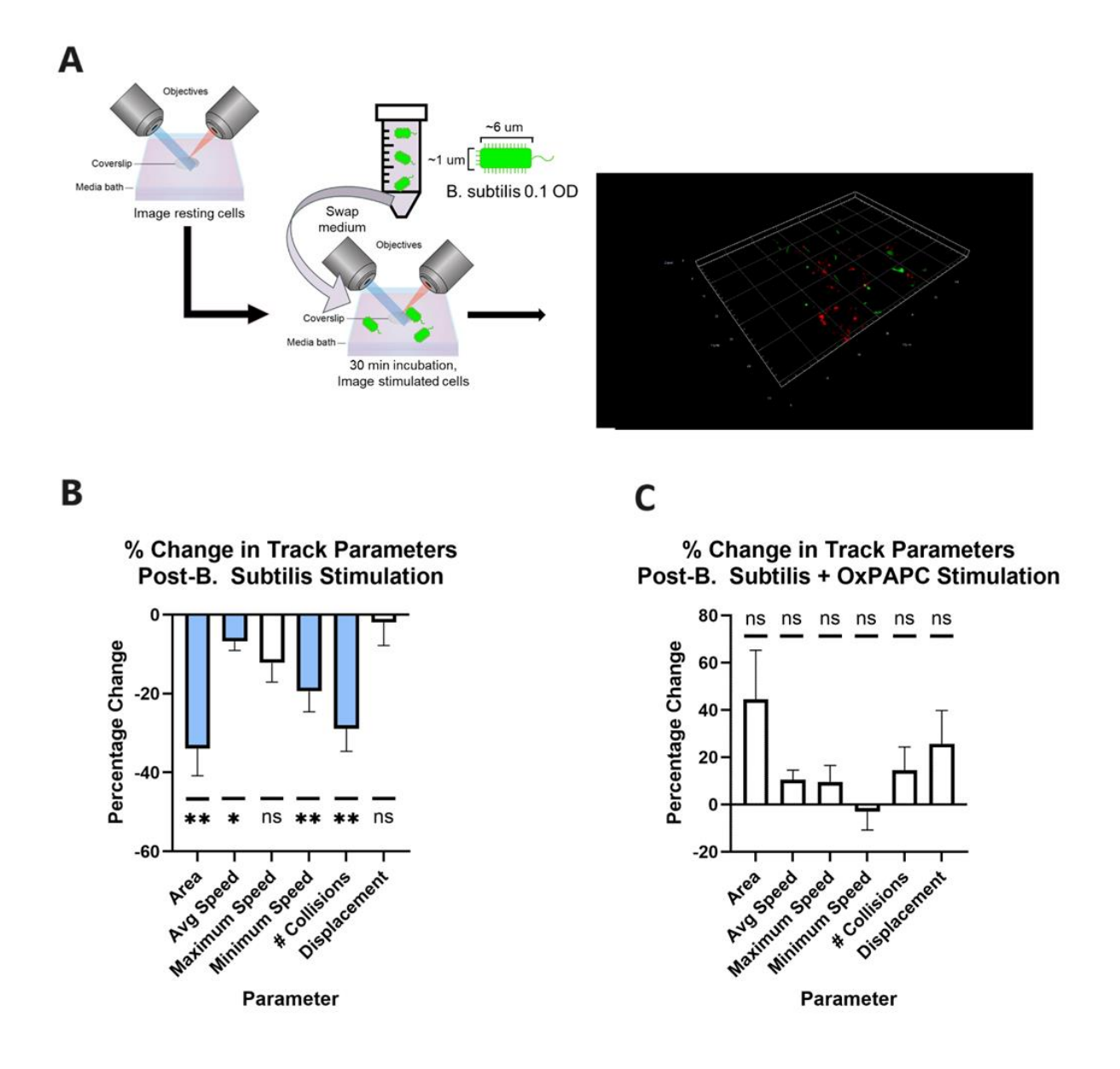


Figure 4.2. Percentage changes in track metrics from resting after stimulating with 0.1 OD *B. subtilis*. (A) Three groups of cells were imaged at rest before being dosed on the microscope with 0.1 OD *B. subtilis* for 30 minutes, then the same coverslip (but three different groups of cells) was imaged again. (B) Percentage change in mean track parameters after *B. subtilis* stimulation when compared to resting. (C) The same experiment was performed with a 1 hour pre-treatment of the macrophages with 111 ng/mL OxPAPC before imaging. Means for each parameter in resting vs. stimulated cells are compared with a two-tailed t-test. NS p > 0.05, ** p < 0.01, *** p < 0.001

When we stimulated with *S. griseus*, we also saw TLR2 behaviors associated with decreased speeds. Average TLR2 track speed decreased by $13.1 \pm 2.80\%$ compared to resting cells; minimum track speed decreased $15.8\% \pm 5.05\%$, and maximum speed decreased by $11.3 \pm 5.09\%$ (**Figure 4.3**). Additionally, TLR2 track displacement decreased by $23.7\% \pm 7.57\%$; track area decreased by $32.3\% \pm 7.33\%$, and number of track collisions decreased by $27.3\% \pm 4.25\%$. Our OxPAPC experiments indicated that these decreases were also TLR2 signaling-dependent (**Figure 4.3**). Taken together, the results from our bacterial stimulation experiments indicate that, contrary to the speed up seen with LTA stimulation, gram-positive bacterial stimulation causes macrophage activation that slows down the cells' TLR2.

We wondered whether the behavioral changes due to bacterial stimulation were driven by TLRs that bound the bacteria. To test this, we labeled the bacteria with Bactoview Live Green stain and took two-color images of both the bacteria and the receptors. We then added a distance measurement between each receptor and the nearest bacterium to our analysis and subset the data by receptors that contacted a bacterium during the imaging period and those that did not. We found no differences between the track parameter means of the two groups of tracks, which indicates that dynamic differences are not due to receptors touching the bacteria during the imaging period (**Tables A.4.2-3**).

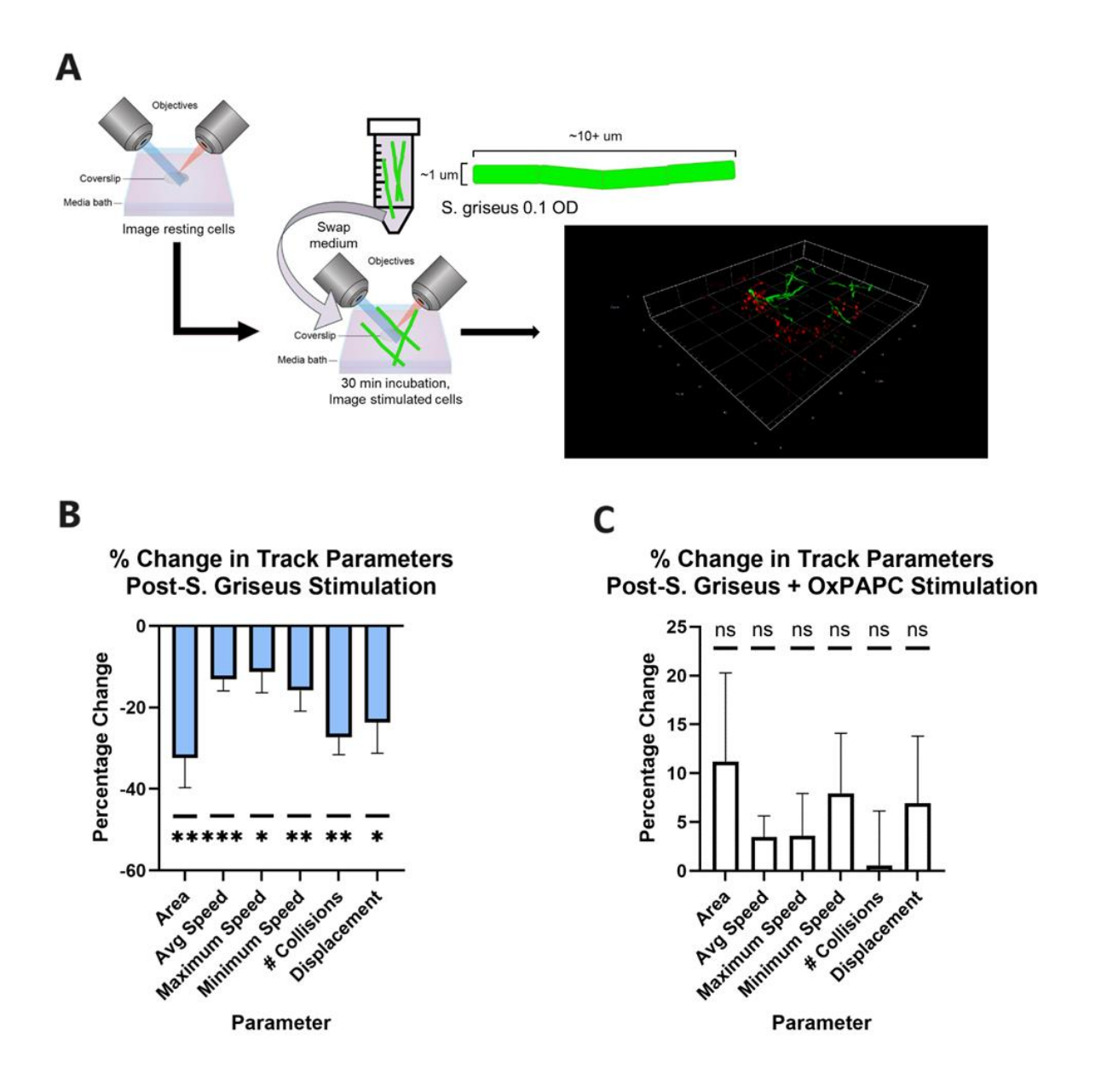


Figure 4.3. Percentage changes in track metrics from resting after stimulating with 0.1 OD *S. griseus*. (A) Three groups of cells were imaged at rest before being dosed on the microscope with 0.1 OD *S. griseus* for 30 minutes, then the same coverslip (but three different groups of cells) was imaged again. (B) Percentage change in mean track parameters after *S. griseus* stimulation when compared to resting. (C) The same experiment was performed with a 1 hour pre-treatment of the macrophages with 111 ng/mL OxPAPC before imaging. Means for each parameter in resting vs. stimulated cells are compared with a two-tailed t-test. NS p > 0.05, ** p < 0.01, *** p < 0.001

4.4.4 TLR Speed Changes Due to Different Bacteria Cause Distinct Functional Changes in Macrophages

Finally, given the biophysical differences in TLR2 signaling we saw for different stimulation regimens using LLSM, we sought to establish that these differences inform the cells' immune responses to different stimuli in terms of IL-6 and TNF α production after stimulation. The fact that OxPAPC blocks both TLR2 signaling and TLR2 dynamic changes—as seen in our LLSM experiments—allowed us to mathematically evaluate the difference between how much bacteria-induced TLR2 dynamic changes contributed to cytokine secretion (Figure 4.4, Materials and Methods) To do this, we first used HEK-BlueTM hTLR2 cells to determine concentrations of both bacteria that would activate TLR2 signaling to the same level after a two hour stimulation (0.05 OD600 B. subtilis, 0.25 OD600 S. griseus, Figure 5B). Then, we dosed mouse bone marrow derived macrophage with these concentrations of bacteria with or without one hour pretreatment with 111 µg/mL OxPAPC for two hours. We then washed the cells to remove the stimulus, let the activated cells secrete cytokines overnight, and used the resulting supernatant for ELISA assays to determine levels of cytokine secretion. For TNF α , we observed a difference between TLR2_{phys, BS} and TLR2_{phys, SG} of -563.58 pg/mL with a 95% confidence interval of [-1112.96, -14.20] pg/mL (Figure 5C). For IL-6, we observed a difference between TLR2_{phys, BS} and TLR2_{phys, SG} of -5244.72 pg/mL with a 95% confidence interval of [-1112.96, -14.20] pg/mL (**Figure 4.4**). These results indicates that the dynamic changes in TLR2 caused by the two bacteria affect both macrophage TNFα and IL-6 secretion levels differently and that the S. griseus TLR2 dynamic changes affect the macrophages more than the B. subtilis changes.

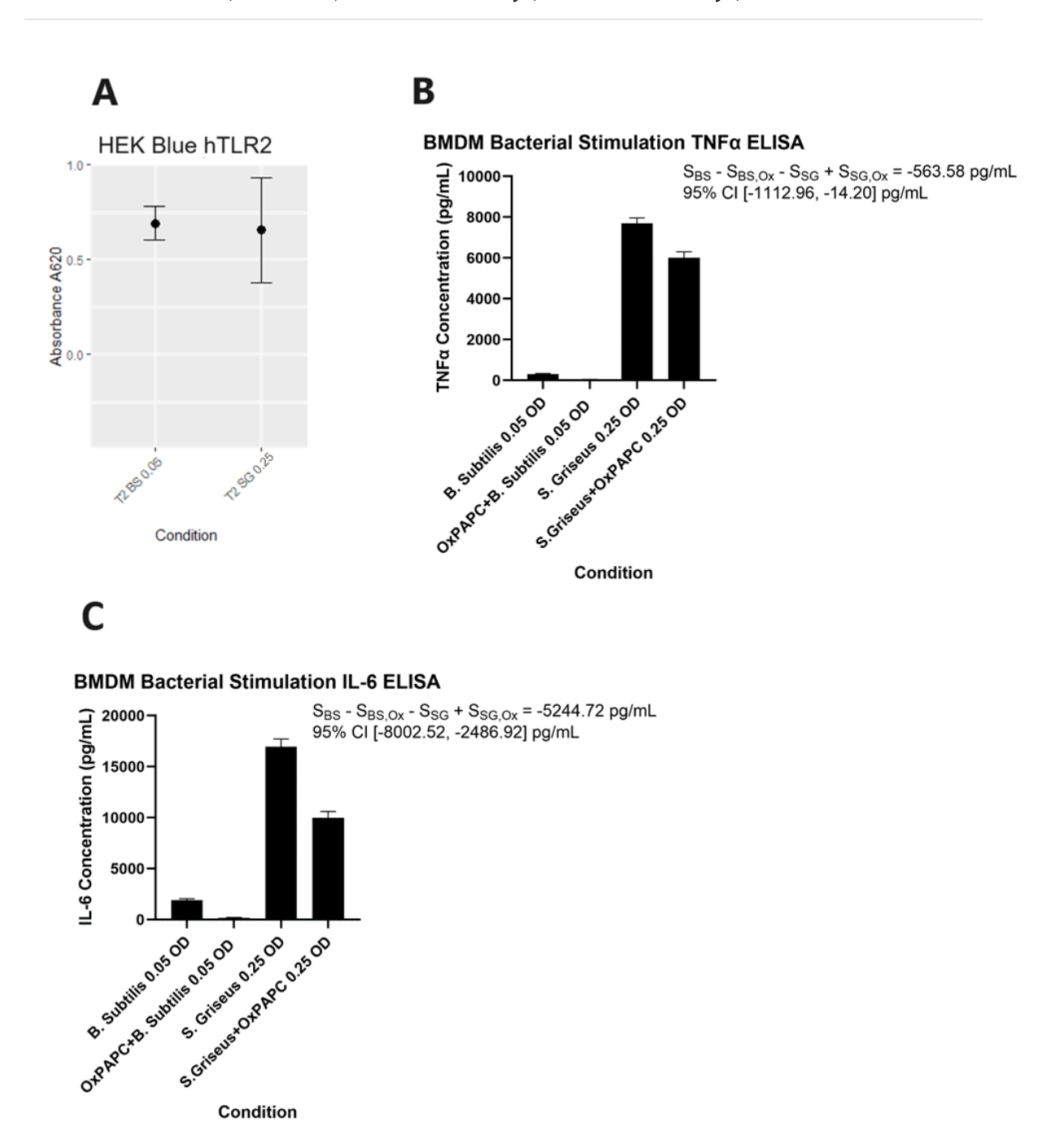


Figure 4.4. Effect of TLR2 physical changes on cytokine secretion in primary macrophages. (A) An expression to quantify the effects of stimulation-induced changes in TLR2/4 physics on macrophage cytokine signaling. S_{BS} = cytokine secretion from B. subtilis stimulation, S_{SG} = cytokine secretion from S. griseus stimulation, $S_{BS, Ox}$ = cytokine secretion from B. subtilis stimulation after OxPAPC treatment, S_{SG} ,

 $_{\rm Ox}$ = cytokine secretion from S. griseus stimulation after OxPAPC treatment, TLR2/4_{Phys, BS} = The effect of B. subtilis-induced changes in TLR2/4 physics on macrophage cytokine secretion, TLR2/4_{Phys, SG} = The effect of S. griseus-induced changes in TLR2/4 physics on macrophage cytokine secretion (B) HEK-BlueTM hTLR2 cells only expressing TLR2 were used to determine a dose of bacteria for which TLR2 activation is the same. Cells were treated with the indicated dosages for two hours then washed three times and let to produce cytokines overnight before quantification with Quanti-BlueTM. (C-D) The same dosages of bacteria were used to treat activate mouse bone marrow derived macrophages with or without one hour pretreatment with 111µg/mL OxPAPC. Cells were incubated for two hours, washed three times and let to produce cytokines overnight before quantification with ELISA. The resulting values were used to calculate that difference between how much bacteria-induced TLR2 physical changes contributed to cytokine secretion (95% CI shown).

4.5 Discussion

Herein, we developed a method to track TLR2 dynamics on RAW 264.7 cells using LLSM and show that macrophages respond to TLR2 signaling by altering their biophysics in a stimulus-dependent manner. We found that single-molecule LTA stimulation caused TLR2 tracks to speed up and move farther while stimulation with gram-positive bacteria caused TLR2 tracks to exhibit behaviors associated with slowing down. We also found that dynamic differences are dependent on TLR2 signaling. Moreover, our results show that macrophages can differentiate between physically distinct stimuli during ligand contact and accordingly coordinate biophysical behaviors which inform biological responses through differential IL-6 and TNFα activation.

We believe that our observations are relevant for synthetic stimulus design where programming certain macrophage behaviors may be beneficial. However, to design stimulants that faithfully mimic relevant biological contexts, we must more precisely characterize the mechanisms through which macrophages distinguish between different stimuli. For example, macrophages might distinguish between bacteria and single ligands because bacteria have a high density of ligand in the same space. The number of different ligands in the bacteria, their distinct patterning on the receptor, and the types and arrangement of responding PRRs could also play a

role encoding information to the macrophage. Further experiments using more engineered ligand systems will help us more rigorously test different arrangements and combinations of stimulants to help correlate PRR behavior in LLSM and macrophage response with specific stimulant physics.

Additionally, there are outstanding questions as to the functional consequences of the macrophage's dynamic changes post-stimulation. We hypothesize that the macrophages speed up due to single-ligand stimulation because single ligands in a biological context would indicate presence of pathogen. Therefore, increased motility would be useful in finding the threat or potentially being more responsive to chemotactic signals. Conversely, if the macrophage senses a whole bacterium, slowing down would keep the macrophage at the relevant site of infection. More spatially regulated experiments with, for example, by using microfluidic devices to create gradients of ligands or motility signals, could clarify physical consequences of our observed TLR2 behaviors.

The TLR2 behaviors might also be caused in part by actin remodeling driven by the activation response, so more investigation into the actin cytoskeleton and phagocytosis regulators such as the Arp2/3 complex and the SCAR/WAVE complex could indicate that cells are preparing for downstream responses to physically different stimuli in biophysically distinctive ways⁹. It has also been hypothesized that actin remodeling can be used to amplify immune signal in low ligand density environments by increased receptor motility on the cell surface, which may be driving TLR2 speed increases in the single-ligand stimulation environment¹⁰. Uncovering more details about the cells' actin responses will afford better understanding about macrophage behaviors and what biophysical responses are advantageous in what situation, which may in turn inform novel stimulant design and macrophage programming.

4.6 References

- 1. Rosenberg, J., & Huang, J. (2020). Visualizing Surface T-Cell Receptor Dynamics Four-Dimensionally Using Lattice Light-Sheet Microscopy. *Journal of visualized experiments : JoVE*, (155), 10.3791/59914. https://doi.org/10.3791/59914
- 2. Ginsburg I. (2002). Role of lipoteichoic acid in infection and inflammation. *The Lancet. Infectious diseases*, 2(3), 171–179. https://doi.org/10.1016/s1473-3099(02)00226-8
- 3. Li, N., Sun, J., Benet, Z. L., Wang, Z., Al-Khodor, S., John, S. P., Lin, B., Sung, M. H., & Fraser, I. D. (2015). Development of a cell system for siRNA screening of pathogen responses in human and mouse macrophages. *Scientific reports*, *5*, 9559. https://doi.org/10.1038/srep09559
- 4. Erridge, C., Kennedy, S., Spickett, C. M., & Webb, D. J. (2008). Oxidized phospholipid inhibition of toll-like receptor (TLR) signaling is restricted to TLR2 and TLR4: roles for CD14, LPS-binding protein, and MD2 as targets for specificity of inhibition. *The Journal of biological chemistry*, 283(36), 24748–24759. https://doi.org/10.1074/jbc.M800352200
- 5. Elson, G., Dunn-Siegrist, I., Daubeuf, B., & Pugin, J. (2007). Contribution of Toll-like receptors to the innate immune response to Gram-negative and Gram-positive bacteria. *Blood*, *109*(4), 1574–1583. https://doi.org/10.1182/blood-2006-06-032961
- 6. Errington, J., & Aart, L. T. V. (2020). Microbe Profile: *Bacillus subtilis*: model organism for cellular development, and industrial workhorse. *Microbiology (Reading, England)*, 166(5), 425–427. https://doi.org/10.1099/mic.0.000922
- 7. Mukherjee, S., & Kearns, D. B. (2014). The structure and regulation of flagella in Bacillus subtilis. *Annual review of genetics*, 48, 319–340. https://doi.org/10.1146/annurev-genet-120213-092406
- 8. Chater, K. F. (1984). Morphological and Physiological Differentiation in Streptomyces. Cold Spring Harbor Monograph Archive, 16(0), 89–115. https://doi.org/10.1101/0.89-115
- 9. Davidson, A. J., & Insall, R. H. (2013). SCAR/WAVE: A complex issue. *Communicative & integrative biology*, 6(6), e27033. https://doi.org/10.4161/cib.27033
- 10. Li, M., & Yu, Y. (2021). Innate immune receptor clustering and its role in immune regulation. *Journal of cell science*, *134*(4), jcs249318. https://doi.org/10.1242/jcs.249318
- 11. Zhang, C., Yang, M., & Ericsson, A. C. (2021). Function of Macrophages in Disease: Current Understanding on Molecular Mechanisms. *Frontiers in immunology*, *12*, 620510. https://doi.org/10.3389/fimmu.2021.620510
- 12. Ross, E. A., Devitt, A., & Johnson, J. R. (2021). Macrophages: The Good, the Bad, and the Gluttony. *Frontiers in immunology*, *12*, 708186. https://doi.org/10.3389/fimmu.2021.708186

- 13. Tang, D., Kang, R., Coyne, C. B., Zeh, H. J., & Lotze, M. T. (2012). PAMPs and DAMPs: signal 0s that spur autophagy and immunity. *Immunological reviews*, 249(1), 158–175. https://doi.org/10.1111/j.1600-065X.2012.01146.x
- 14. Danen EHJ. Integrins: An Overview of Structural and Functional Aspects. In: Madame Curie Bioscience Database [Internet]. Austin (TX): Landes Bioscience; 2000-2013. Available from: https://www.ncbi.nlm.nih.gov/books/NBK6259/
- 15. Watanabe, S., Alexander, M., Misharin, A. V., & Budinger, G. R. S. (2019). The role of macrophages in the resolution of inflammation. *The Journal of clinical investigation*, 129(7), 2619–2628. https://doi.org/10.1172/JCI124615
- 16. Billack B. (2006). Macrophage activation: role of toll-like receptors, nitric oxide, and nuclear factor kappa B. *American journal of pharmaceutical education*, 70(5), 102. https://doi.org/10.5688/aj7005102
- 17. Kimani, F. W., Ajit, J., Galluppi, A., Manna, S., Howitz, W. J., Tang, S., & Esser-Kahn, A. P. (2021). Receptor-Ligand Kinetics Influence the Mechanism of Action of Covalently Linked TLR Ligands. *ACS chemical biology*, *16*(2), 380–388. https://doi.org/10.1021/acschembio.0c00924
- 18. Li, W., Li, M., Anthony, S. M., & Yu, Y. (2021). Spatial organization of FcγR and TLR2/1 on phagosome membranes differentially regulates their synergistic and inhibitory receptor crosstalk. *Scientific reports*, *11*(1), 13430. https://doi.org/10.1038/s41598-021-92910-9
- 19. Deak, P., Kimani, F., Cassaidy, B., & Esser-Kahn, A. (2020). Determining Whether Agonist Density or Agonist Number Is More Important for Immune Activation via Micoparticle Based Assay. *Frontiers in immunology*, 11, 642. https://doi.org/10.3389/fimmu.2020.00642
- 20. Lovewell, R. R., Collins, R. M., Acker, J. L., O'Toole, G. A., Wargo, M. J., & Berwin, B. (2011). Step-wise loss of bacterial flagellar torsion confers progressive phagocytic evasion. *PLoS pathogens*, 7(9), e1002253. https://doi.org/10.1371/journal.ppat.1002253
- 21. Otte, S., Ipiña, E. P., Pontier-Bres, R., Czerucka, D., & Peruani, F. (2021). Statistics of pathogenic bacteria in the search of host cells. *Nature communications*, *12*(1), 1990. https://doi.org/10.1038/s41467-021-22156-6
- 22. Aaron, J. S., Carson, B. D., & Timlin, J. A. (2012). Characterization of differential Toll-like receptor responses below the optical diffraction limit. *Small (Weinheim an der Bergstrasse, Germany)*, 8(19), 3041–3049. https://doi.org/10.1002/smll.201200106
- 23. Chen, B. C., Legant, W. R., Wang, K., Shao, L., Milkie, D. E., Davidson, M. W., Janetopoulos, C., Wu, X. S., Hammer, J. A., 3rd, Liu, Z., English, B. P., Mimori-Kiyosue, Y., Romero, D. P., Ritter, A. T., Lippincott-Schwartz, J., Fritz-Laylin, L., Mullins, R. D., Mitchell, D. M., Bembenek, J. N., Reymann, A. C., ... Betzig, E. (2014). Lattice light-sheet microscopy:

- imaging molecules to embryos at high spatiotemporal resolution. *Science (New York, N.Y.)*, 346(6208), 1257998. https://doi.org/10.1126/science.1257998
- 24. Rosenberg, J., Cao, G., Borja-Prieto, F., & Huang, J. (2020). Lattice Light-Sheet Microscopy Multi-dimensional Analyses (LaMDA) of T-Cell Receptor Dynamics Predict T-Cell Signaling States. *Cell systems*, *10*(5), 433–444.e5. https://doi.org/10.1016/j.cels.2020.04.006
- 25. Schwandner, R., Dziarski, R., Wesche, H., Rothe, M., & Kirschning, C. J. (1999). Peptidoglycan- and lipoteichoic acid-induced cell activation is mediated by toll-like receptor 2. *The Journal of biological chemistry*, 274(25), 17406–17409. https://doi.org/10.1074/jbc.274.25.17406
- 26. Rueden, C. T., Schindelin, J., Hiner, M. C., DeZonia, B. E., Walter, A. E., Arena, E. T., & Eliceiri, K. W. (2017). ImageJ2: ImageJ for the next generation of scientific image data. *BMC bioinformatics*, 18(1), 529. https://doi.org/10.1186/s12859-017-1934-z

CHAPTER 5: INVESTIGATING KEY PHYSICAL PARAMETERS DURING BACTERIAL STIMULATION OF MACROPHAGES USING FLUIDIC FORCE MICROSCOPY

Parts of this chapter have been reproduced with permission from Liza Mulder and Sara Hoggatt.

5.1 Summary

Macrophages use physical ligand-receptor interactions through PRRs to sense when a pathogen is present and prime for immune activation and clearance of the pathogen.

Accordingly, the biophysics of the contact between macrophages and pathogens is an important consideration when studying macrophage activation. Here, we use fluidic force microscopy (FluidFM) to precisely control the exposure of *b. subtilis* to fluorescent reporter macrophages and vary the biophysics of the stimulus. We find that, surprisingly, single *b. subtilis* do not robustly activate short-term macrophage responses and that two or more bacteria are required to see a response during 30 minutes of pathogen contact with the macrophage. Additionally, we see that increasing the approach speed of the contact and programming dynamic tapping action during contact do not improve the single *b. subtilis* ability to activate the macrophage. We conclude that higher levels of ligand exposure than a single bacterium provides is essential for activation in the context of our experiments. These studies lend more nuanced understanding of the context cues macrophages sense *in vitro* and pave the way to use FluidFM to robustly study single host-pathogen interactions in contexts where biophysics are relevant.

5.2 Introduction

When macrophages sense pathogens through PRRs, they physically interface with the pathogen to bind their cell surface receptors, capture the pathogen, and prepare for downstream responses such as endocytosis. Recent evidence shows that the host cells and PRRs undergo

coordinated organization and dynamical changes to effect immune responses in response to pathogen exposure^{1,2,3}; however, less is known about how the biophysics of the pathogen affect the host cell's response. Some research suggests, for example, that the structure of the pathogen and arrangement in space of ligands causes differential immune responses in responding macrophages⁴. Additionally, it has been shown that knocking out flagellar motor rotation in bacteria causes them to be more efficient at phagocytic evasion⁴, that the number of encounters between host cells and bacteria depends on the diffusivity of the bacteria⁵, and that bacterial search behaviors can depend on morphological variation within bacterial species⁶. Despite this work, however, it has been challenging to adequately assay the types and magnitudes of pathogen biophysical parameters that most impact innate immune detection—in part because it is difficult to precisely and accurately control the physics of pathogen presentation to immune cells.

Here, we utilize fluidic force microscopy (FluidFM) to exert exact control over *B. subtilis* bacterial presentation to fluorescent NFkB reporter macrophages to monitor the immune response while varying exposure parameters. We have begun a preliminary analysis that varies number of contacts, contact duration, approach speed, and bacterial health to determine parameters that impact immune sensing. Our results show that single bacteria alone struggle to activate macrophages and that the exposure time for a single bacterium required to efficiently activate the cell may be much higher than the typical duration of single pathogen exposures under uncontrolled conditions. Higher bacteria counts—at least two or more—seem more effective for stimulating a macrophage response toward the stimulus.

5.3 Materials and Methods

Immortalized Cell Culture

RAW 264.7 G9 clone⁷ cells were all maintained in DMEM (Life Technologies) supplemented with 10% fetal bovine serum (FBS) (Life Technologies) and 1% antibioticantimycotic (Life Technologies) at 37°C and 5% CO₂ in T75 cell culture flasks.

Bacterial Culture

B. subtilis was maintained in tryptic soy broth (BD Bacto, Fisher Scientific) in an incubator at 37°C shaking at 225 RPM. In frozen conditions, bacteria were used directly from frozen stocks made with 50% glycerol.

Cell Preparation for FluidFM

Raw 264.7 G9 cells were detached from the culture flask using warm HBSS (Gibco) and replated in a 50mm microscopy dish (TedPella 14027-200) in DMEM + 10% heat-inactivated FBS (HI-FBS, Life Technologies) at 500,000 cells/plate density and left to incubate overnight at 37°C and 5% CO₂.

One hour before the experiment, medium was changed to 10% HI-FBS in CO2-Independent medium (Fisher Scientific) with 2% L-glutamine. The cells were then incubated 30-60 min at 37°C and atmospheric CO₂ on the microscope, stained with 100 ng/mL Hoechst 33342 nuclear stain (Fisher Scientific), and incubated a further 15-30 min. Cells were kept in a heated box surrounding the FluidFM microscope (Cytosurge) at 37°C for the duration of the experiment.

B. Subtilis Preparation for FluidFM

Roughly 50 μ L of the *B. subtilis* culture was added to fresh tryptic soy broth to a total volume of 500 μ L. 1 μ L of BactoView Live Red stain (Biotium) was added to the culture and the mixture was incubated at 37°C with end-over-end mixing for 1 hour. The bacteria were then pelleted at 9000 x g for 10 minutes, and the supernatant was removed and replaced with fresh

broth. The labeled *B. subtilis* solution was then put into a 50mm microscopy dish with 2 mL of broth and kept covered at 37°C in the heated microscope box until ready for use.

Bacterial Stimulation with the FluidFM

The dish with the labeled bacteria was placed under the FluidFM probe and the probe was lowered to the bottom of the dish using a 200 mV deflection. The probe was then raised by 2 µm and centered over a bacterium in the dish. -200 mbar of pressure was exerted at the probe tip, and the probe was lowered again on top of the bacterium until the bacterium stuck to the probe. Sticking was confirmed by moving the probe and seeing the bacterium move with it.

The probe was then lifted 100 μ m and the bacteria dish was replaced with a coverslip. The probe with bacterium was then washed by pipetting a 750 μ L drop of water onto the coverslip, letting the probe sit in the water, and repeating this wash three additional times.

The washing coverslip was then replaced with the dish of RAW 264.7 G9 cells, and the probe was lowered to the bottom of the dish in an empty region next to a cell of interest. The probe was then raised 5 μ m and an image stack of the resting cell was acquired. The probe was then centered over the cell and the approach setpoint was set to ~30-40 mV before lowering the probe and bacterium to contact the macrophage. Image stacks were acquired after contact at 5-minute intervals. After the desired contact time, the probe was lifted 100 μ m and image acquisition continued until the end of the experiment.

Image Analysis

Image quantification was carried out in CellProfiler as previously described⁸. Briefly, each nucleus in the Hoechst stain was outlined, and then the outlines were slightly shrunken and expanded. In the GFP image, the area between the expanded and original outlines was taken to

be cytoplasmic GFP signal, and the area inside the shrunken outline was taken to be nuclear GFP signal. The ratios of these numbers determined cellular activation for each cell.

Microscopy

Imaging was performed using a Zeiss Axio Observer 7 inverted optical microscope, Hamamatsu ORCA-Flash4.0 V3 sCMOS camera (Hamamatsu C13440-20CU-KIT), Spectra-X Light Engine, and Zeiss Zen Pro software. Microscope equipped with Pecon live cell incubation box, Zeiss Heating Unit XL S, and Zeiss TempModule S to maintain temperature at 37°C when imaging live cells. RAW 264.7 G9 cells stimulated with the FluidFM were imaged at the same location before and after treatment using a 40x (Zeiss 441350-9970-000) air objective. Channels: hoechst33342 nuclear stain (Ex/Em 350/461) and GFP reporter (Ex/Em 488/507).

5.4 Results

5.4.1 FluidFM Stimulation of Macrophages with *B. Subtilis*

The FluidFM is a combination of atomic force microscope (AFM) and micropipette capable of fine-grained manipulation of single cells *in vitro*. The AFM cantilever has a pressure-controlled channel for nanoliter-scale liquid handling while offering sensitive force detection using laser deflection off its surface¹⁰. We used this instrument to present *B. subtilis* bacteria by labeling the bacteria and applying negative pressure to stick bacteria to the FluidFM probe. We then lowered the bacteria down onto RAW 264.7 G9 macrophages⁷, which stably express GFP-tagged p65 subunits of NFκB. Together with a nuclear Hoechst 33342 stain, we can image and track NFκB nuclear localization in the stimulated cell to assay its immune activation (**Figure** 5.1). We can then vary physical parameters of the contact—such as number of bacteria, contact

speed, and number of contacts—to determine which features might be most important for optimal pathogen sensing.

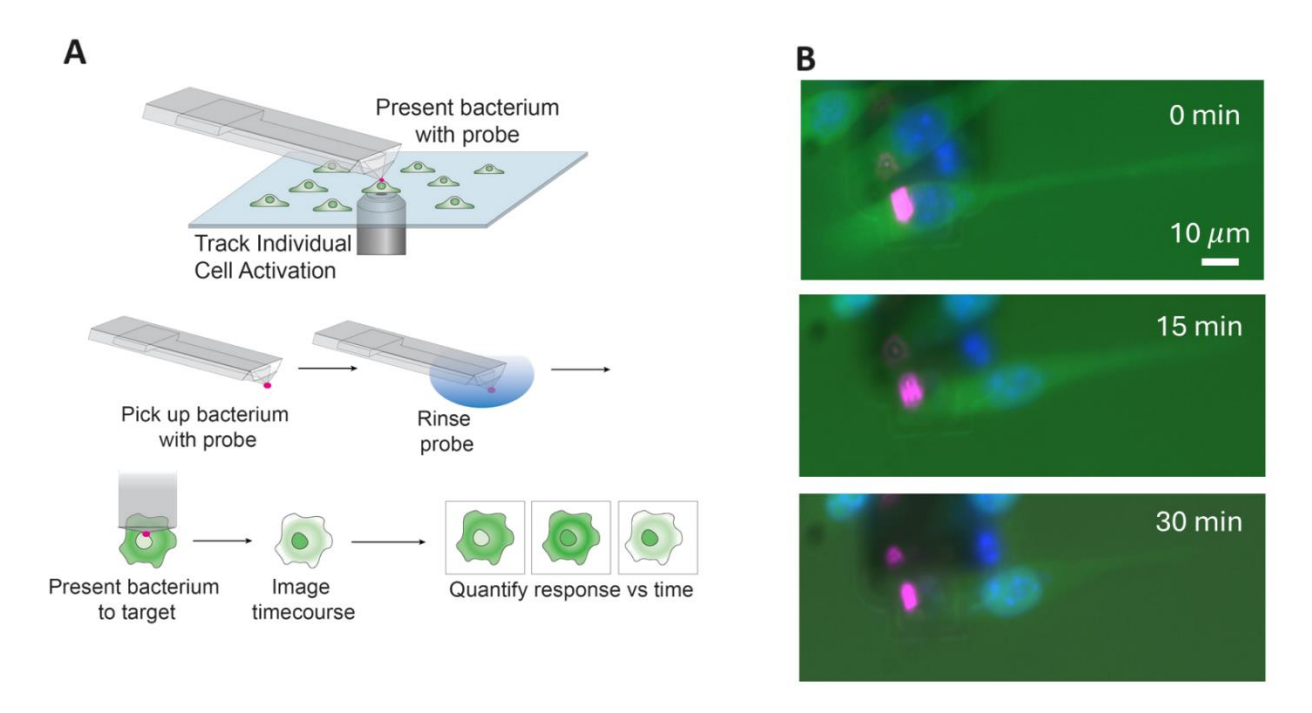


Figure 5.1. Representative FluidFM stimulation with *B. subtilis*. (A) Diagram of the experimental proctocol. Labeled bacteria are picked up using suction from the probe, washed in a bead of water four times, then presented to a fluorescent reporter macrophage with labeled NFκB. As the experiment proceeds, the nuclear localization of NFκB is tracked to determine level of immune activation. (B) Representative microscopy imaging of an activated macrophage. Pink: labeled bacterium (BactoView Live Red), green: NFκB-GFP, blue: nuclear Hoescht 33342.

5.4.2 More Than One *B. subtilis* is Required to Activate Macrophages During Short-Term FluidFM Stimulation

In our initial experiments, we used the FluidFM to present RAW 264.7 G9 macrophages with single *B. subtilis* stained with Bactoview Live Red stain directly after thawing from -80°C glycerol stocks. We used the nuclear-to-cytoplasmic ratio of the GFP-labeled NFκB in these cells to assay cellular activation via microscopy. Surprisingly, after 30 minutes of continuous bacteria-macrophage contact, we saw that freshly thawed bacteria did not activate the macrophages any better than the negative controls of blank polystyrene beads (**Figure 5.2**). We

then tested with bacteria that had been grown and passaged at least once before exposure and found similar results.

We then tested stimulation with clumps of bacteria to see if higher source ligands would activate macrophages better. While using visual quantitation of number of bacteria in the clump, we achieved significant macrophage activation when stimulating with clumps of 2-10 *B. subtilis* (**Figure 5.2**). These results suggest that there is a critical mass of bacteria beyond a single bacterium that is required to activate a macrophage *in vitro*.

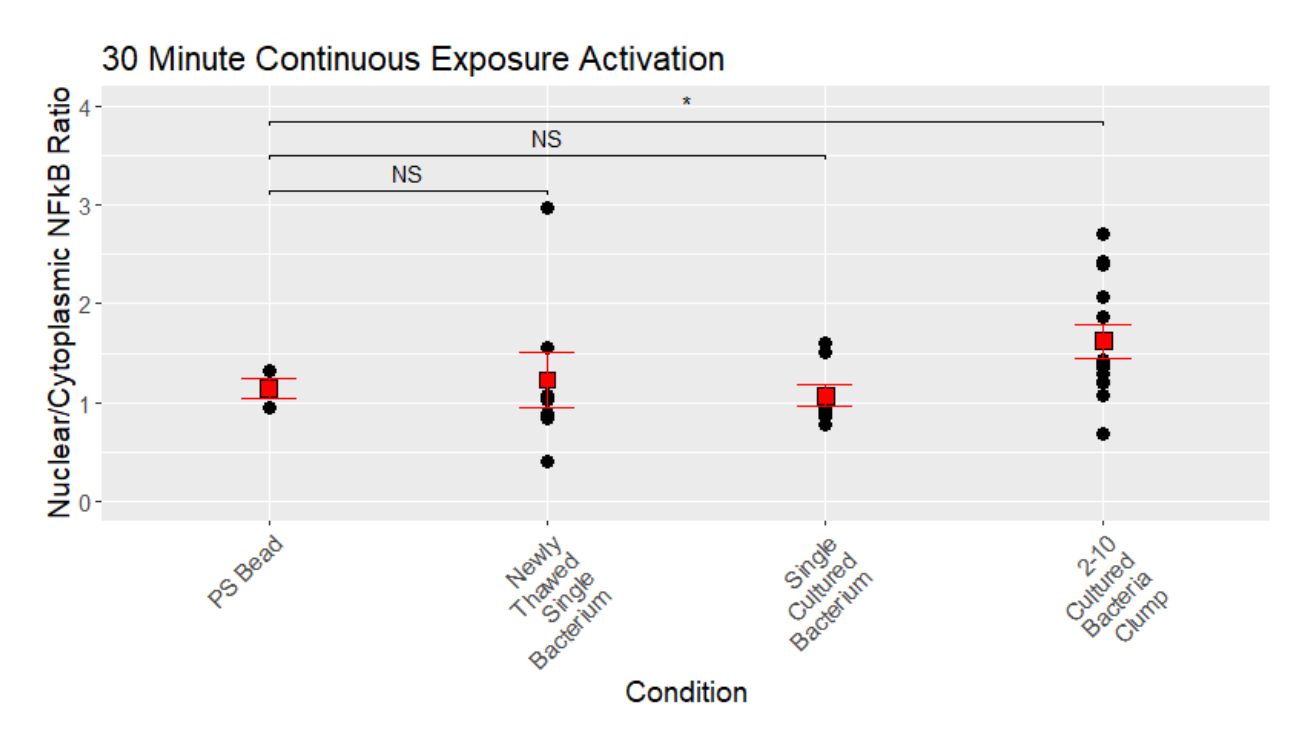


Figure 5.2. Multiple *B. subtilis* are required for efficient macrophage stimulation. Single *B. subtilis* or clumps of *B. subtilis* numbering 2-10 bacteria were presented to macrophages for 30 minutes. Cells were assessed for nuclear/cytoplasmic NF κ B ratio at 30 minutes. Means for each group are compared with a two-tailed t-test. NS p > 0.05, * p < 0.05.

5.4.3 Increased Approach Speed of Single *B. Subtilis* Does Not Improve Macrophage Responses

Prior work shows that bacterial speed is related to macrophage detection and phagocytosis: for example, that phagocytosis increases with increasing centrifugal force of

bacteria on a monolayer of macrophages⁹, or that phagocytosis can decrease when motility of bacteria is suppressed⁴. We therefore tested whether bacteria could be sensed better by increasing the approach speed of the FluidFM-mediated contact between *B. subtilis* and macrophages.

When we compared typical experimental approach speeds of 2 μ m/s to approach speeds of 12.9 μ m/s during a 30-minute stimulation, we found no significant difference in the ability of single bacteria to stimulate the macrophage, and they did not stimulate above the level of 2 μ m/s negative controls (**Figure 5.3**). This result suggests that, while higher approach speeds might inform higher stimulation efficiency in bulk scenarios, stimulation with more than one bacterium is still required to effectively activate the cell even with high speeds.

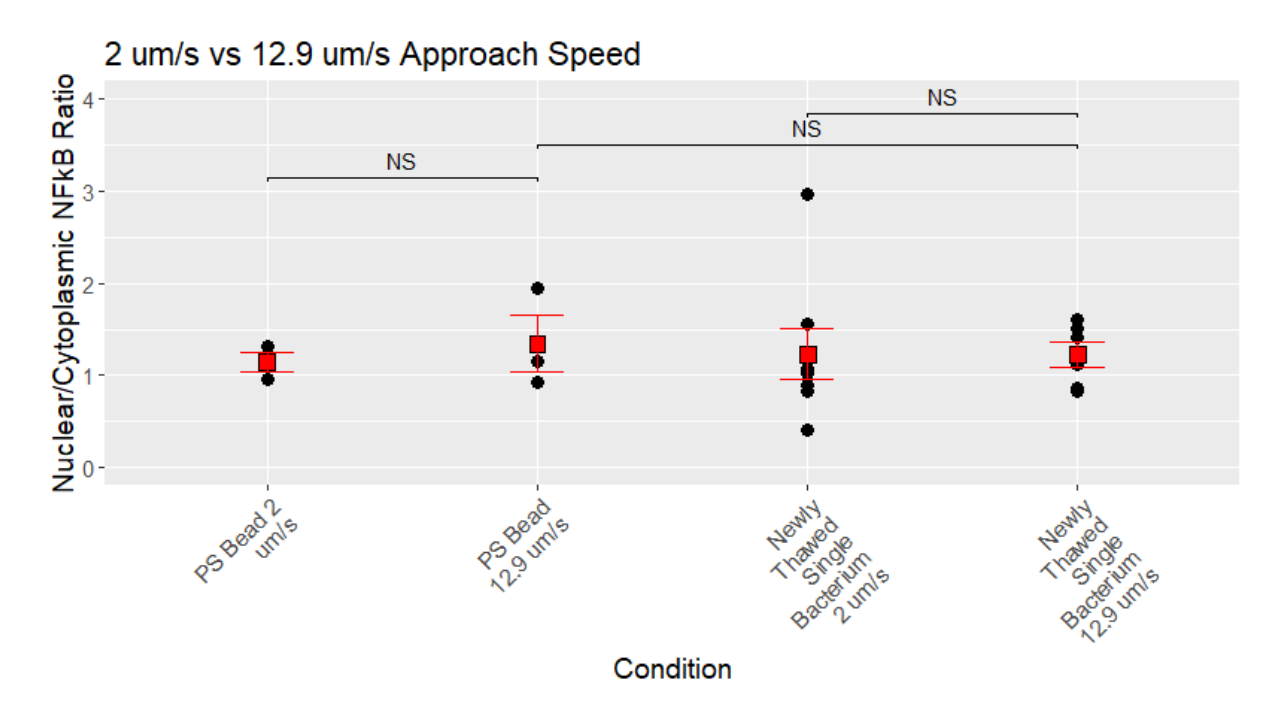


Figure 5.3. High *B. subtilis* approach speeds do not improve macrophage stimulation. Single *B. subtilis* were presented to macrophages for 30 minutes with an approach speed during the contact of 2 μ m/s or 12.9 μ m/s. Cells were assessed for nuclear/cytoplasmic NF κ B ratio at 30 minutes. Means for each group are shown in red and compared with a two-tailed t-test. NS p > 0.05.

5.4.4 Dynamic Tapping of Single *B. Subtilis* on the Macrophage Does Not Improve Macrophage Responses

We also considered whether dynamic exposure of the bacterium to the macrophage over the experimental window would improve the macrophage's response. This type of exposure is perhaps more faithful to freely moving pathogens, as we have seen some *B. subtilis* exhibiting short duration contacts of around 10 seconds or fewer using lattice light sheet microscopy and others note similar contact times during *Salmonella* infection¹¹. We therefore used the FluidFM to tap the bacteria on the macrophage during the exposure. We either tapped 10 times for 1 second each or 10 times for 18 seconds each before a final holding of the bacterium onto the macrophage for the rest of the 30-minute experimental window. After these stimulations, we saw no difference in the ability of single *B. subtilis* to activate the macrophages (**Figure 5.4**). These results suggest that a dynamic initial stimulus, while perhaps more biologically relevant, is not enough to have a macrophage respond to a single bacterium.

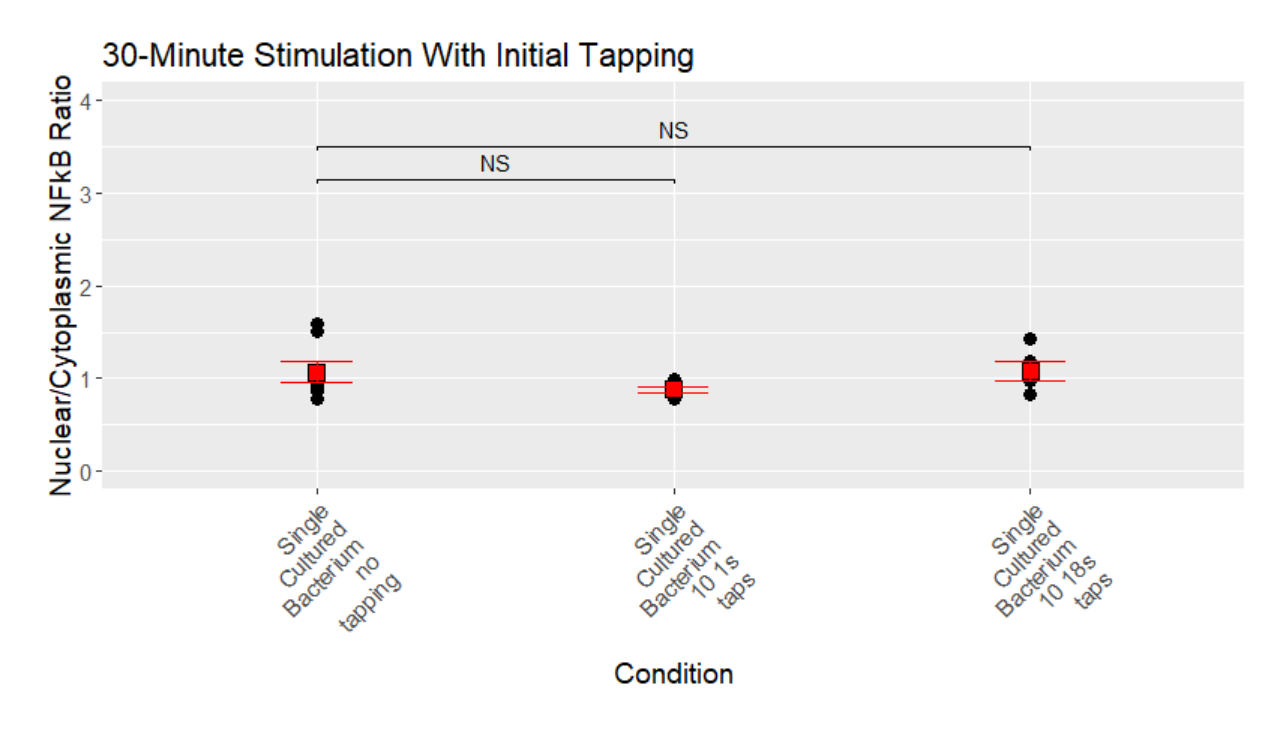


Figure 5.4. Tapping during initial *B. subtilis* contact does not impact macrophage response. Single *B. subtilis* were presented to macrophages for 30 minutes without tapping, with 10 1 second taps before maintain contact for the rest of the 30 minutes or with 10 18s taps before maintaining contact for the rest of the 30 minutes. Cells were assessed for nuclear/cytoplasmic NF κ B ratio at 30 minutes. Means for each group are shown in red and compared with a two-tailed t-test. NS p > 0.05.

5.5 Discussion

In this study, we presented individual *b. subtilis* to macrophages using FluidFM to quantitatively assess activation of the macrophages toward sparse bacterial stimulus. Due to the FluidFM methodology, we had precise control over the physics of this interaction, and we varied approach speed and dynamics of the interaction to simulate certain parameters we hypothesized would modulate activation based on prior work. Our results indicate that, surprisingly, it takes more than one bacterium to robustly activate a single macrophage, and that the activation due to a single bacterium was not improved by increased approach speeds or dynamic tapping of the bacterium during exposure.

It is unclear exactly why single bacteria do not activate the macrophage; however, we hypothesize that it might relate to a mechanism by which macrophages regulate low-dose responses. It has been shown that NFkB signaling is modular depending on the strength of the stimulus—that high, sustained stimulus leads to rapid and uniform cellular activation and that low, sustained stimulus leads to heterogeneous response probability and delayed activation timing¹². This principle is sensible in terms of the broad immune landscape: if cells were always rapidly and strongly responsive to small signals, it might lead to significant immune-related damage, so some tolerance of low signals is appropriate. We might be seeing some form of this tolerance in single *b. subtilis* exposures; however, further research is required to understand the precise nature of the tolerance of low bacterial ligand ligation by PRRs.

We are also interested in more detailed probing of the parameters that cause effective macrophage activation. We saw no changes in single-bacterium activation due to variance in approach speed or tapping; however, it does not mean these parameters are uninformative in higher dose stimulation cases. Further work using bacterial clumps or other controllable activating stimuli (e.g. ligand-coated microparticles) is required to adequately characterize the effects of biophysical contact variation on macrophage activation.

Finally, we are continuing to consider the biological environment and ramifications of our findings on host-pathogen interactions *in vivo*. We respect that there is significant biological context missing from our experiments that macrophages would experience *in vivo* that could inform the system, e.g. macrophage polarization signals¹³ and responses from neighboring cells¹⁴. It is possible to simulate certain of these environments *in vitro* by pretreating the macrophages with growth factors, supplementing the medium with cytokines, or by activating neighboring cells using the FluidFM. We are particularly interested in what signals might prime macrophages to activate more robustly toward single bacteria or be more responsive to changes in the biophysical environment of the cell. Additionally, we are considering what low activation due to single pathogens might mean therapeutically. Further work is needed to determine if we can, for example, introduce compounds that prime the macrophage to activate against lower pathogen signals to enhance clearance without over-activating against non-invasive signals, or if we can increase bacterial signaling by causing bacteria to clump into higher-dose ligands assemblies.

5.6 References

- 1. Inoue, M., & Shinohara, M. L. (2014). Clustering of pattern recognition receptors for fungal detection. *PLoS pathogens*, *10*(2), e1003873. https://doi.org/10.1371/journal.ppat.1003873
- 2. Neumann, J., , Ziegler, K., , Gelléri, M., , Fröhlich-Nowoisky, J., , Liu, F., , Bellinghausen, I., , Schuppan, D., , Birk, U., , Pöschl, U., , Cremer, C., , & Lucas, K., (2019). Nanoscale distribution of TLR4 on primary human macrophages stimulated with LPS and ATI. *Nanoscale*, *11*(19), 9769–9779. https://doi.org/10.1039/c9nr00943d
- 3. Li, M., & Yu, Y. (2021). Innate immune receptor clustering and its role in immune regulation. *Journal of cell science*, *134*(4), jcs249318. https://doi.org/10.1242/jcs.249318
- 4. Lovewell, R. R., Collins, R. M., Acker, J. L., O'Toole, G. A., Wargo, M. J., & Berwin, B. (2011). Step-wise loss of bacterial flagellar torsion confers progressive phagocytic evasion. *PLoS pathogens*, 7(9), e1002253. https://doi.org/10.1371/journal.ppat.1002253
- 5. Otte, S., Ipiña, E. P., Pontier-Bres, R., Czerucka, D., & Peruani, F. (2021). Statistics of pathogenic bacteria in the search of host cells. Nature communications, 12(1), 1990. https://doi.org/10.1038/s41467-021-22156-6
- 6. Ek, V., Fattinger, S. A., Florbrant, A., Hardt, W. D., Di Martino, M. L., Eriksson, J., & Sellin, M. E. (2022). A motile doublet form of Salmonella Typhimurium diversifies target search behavior at the epithelial surface. *Molecular microbiology*, *117*(5), 1156–1172. https://doi.org/10.1111/mmi.14898
- 7. Li, N., Sun, J., Benet, Z. L., Wang, Z., Al-Khodor, S., John, S. P., Lin, B., Sung, M. H., & Fraser, I. D. (2015). Development of a cell system for siRNA screening of pathogen responses in human and mouse macrophages. *Scientific reports*, *5*, 9559. https://doi.org/10.1038/srep09559
- 8. Mulder, E. J., Moser, B., Delgado, J., Steinhardt, R., & Esser-Kahn, A. P. (2024). Protocol for localized macrophage stimulation with small-molecule TLR agonist via fluidic force microscopy. *STAR protocols*, *5*(1), 102873. https://doi.org/10.1016/j.xpro.2024.102873
- 9. Tomita, T., & Kanegasaki, S. (1982). Enhanced phagocytic response of macrophages to bacteria by physical impact caused by bacterial motility or centrifugation. *Infection and immunity*, *38*(3), 865–870. https://doi.org/10.1128/iai.38.3.865-870.1982
- 10. Li, M., Liu, L. & Zambelli, T. FluidFM for single-cell biophysics. *Nano Res.* **15**, 773–786 (2022). https://doi.org/10.1007/s12274-021-3573-y
- 11. Achouri, S., Wright, J. A., Evans, L., Macleod, C., Fraser, G., Cicuta, P., & Bryant, C. E. (2015). The frequency and duration of Salmonella-macrophage adhesion events determines infection efficiency. *Philosophical transactions of the Royal Society of London. Series B*, *Biological sciences*, *370*(1661), 20140033. https://doi.org/10.1098/rstb.2014.0033

- 12. Kellogg, R. A., Tian, C., Lipniacki, T., Quake, S. R., & Tay, S. (2015). Digital signaling decouples activation probability and population heterogeneity. *eLife*, *4*, e08931. https://doi.org/10.7554/eLife.08931
- 13. Singh, A., Sen, S., Iter, M., Adelaja, A., Luecke, S., Guo, X., & Hoffmann, A. (2024). Stimulus-response signaling dynamics characterize macrophage polarization states. *Cell systems*, *15*(6), 563–577.e6. https://doi.org/10.1016/j.cels.2024.05.002
- 14. Mulder, E. J., Moser, B., Delgado, J., Steinhardt, R. C., & Esser-Kahn, A. P. (2024). Evidence of collective influence in innate sensing using fluidic force microscopy. *Frontiers in immunology*, *15*, 1340384. https://doi.org/10.3389/fimmu.2024.1340384

CHAPTER 6: CONCLUSIONS AND FUTURE DIRECTIONS

6.1 Research Summary

In this thesis, we have interrogated the spatial and temporal biophysics of innate immune activation in a variety of novel ways. Firstly, we used spatially organized TLR agonists to stimulate unique kinetic and functional NFkB responses relative to unorganized agonist mixtures. We then used LLSM to track labeled TLR2 after stimulation with single-molecule TLR2 agonists or Gram-positive bacteria and found different modes of stimulation caused biophysical changes to the TLR2. Generally, single-molecule agonists caused behaviors associated with increases in TLR2 speed and bacteria caused behaviors associated with decreased TLR2 speed, and these changes had functional consequences for the cell. Finally, we used FluidFM to precisely control the physics of contact between a bacterium and an NFkB reporter macrophage and found that single B. subtilis bacteria are unable to stimulate short-term activation in macrophages, and increased approach speed or dynamic tapping in the contact do not improve immunogenicity. Our techniques have provided us with the ability to probe the small- and fast-scale interactions of the innate immune system with unprecedented specificity, throughput, and control and lead us to new understanding about the physical immune world and new directions for further research.

6.2 Multi-Molecule Ligands as a Therapeutic Frontier

PRRs afford the immune system a robust way to recognize a wide range of signals associated with pathogens. The nature of PRR signaling is by necessity a cooperative one: since pathogens contain many PAMPs simultaneously, a given pathogen exposure will see many PRRs activating toward the same pathogen. Indeed, the synergies and antagonisms between different

PRRs is the subject of much discourse in the field. Many studies have evaluated receptor pairs and noted that combinatorial activation of certain receptors leads to enhanced immune responses in certain contexts (e.g. TLR3/TLR7 synergy in porcine reproductive and respiratory virus response¹, dectin-1/TLR2/4 synergy for TNFα production², and TLR9/STING synergy for antitumor activity³). Additionally, studies have shown PRR crosstalk must be tightly regulated, as certain agonist combinations are implicated in inflammatory disease⁴. The mechanisms for crosstalk between different PRRs are not always clear; however, since many of these receptors share pathways, adaptors, kinases, and downstream effectors, there are many opportunities for synergy on a molecular level to provide uniquely programmed responses to combinatorial agonists.

We hope to take advantage of these synergies to exert control over immune responses. We have shown that, by developing new molecules that combine different ligand cues in structured ways, we can ensure relevant signals are being displayed to the cell in spatial arrangements that program the kinetics of the immune response in specific ways. Again, the precise mechanisms of this programming require further study and depend largely on the agonists being combined. It is possible, for instance, that combinatorial surface TLR agonists allow for efficient crosslinking of MyD88 at the receptor TIR domains, which we could assess through MyD88 cluster microscopy. It is also possible that the chemical interactions between receptor and ligand play a role—e.g. if a high affinity ligand could help chaperone a lower affinity ligand to its receptor; further binding studies with specific ligand pairs may help illustrate this principle.

There are many possible applications for which multi-ligand stimulation may be beneficial. For example, innate immune training can be achieved through multiple different

PRRs by stimulation with specific training molecules⁵. One might imagine a multi-PRR agonist that co-delivers training and supplemental stimuli for efficient or programmable training. We also do not have to stop at merely linking PRR agonists together. Other non-PRR receptors have shown important crosstalk with PRRs—e.g. macrophage scavenger receptor 1 crosstalk with TLR4 for fungal clearance⁶. Finally, our lab has discovered small molecular immunomodulators that promote or suppress specific immune programming⁷, which might be of benefit to co-administer using a linked-ligand approach with stimulatory compounds, for example, in vaccines to program effective protective responses while minimizing side effects.

6.3 Probing TLR Activation Through Microscopy

Even though microscopy has improved tremendously for live biological imaging applications in recent years, live microscopy of TLR activation is still limited. Nonetheless, our research shows that TLR tracking can offer a compelling window into the cell's behavior toward stimulants during activation. In showing that the biophysical response of TLR2 changes toward differently sized and shaped stimuli, we have highlighted that the cell is somehow able to differentiate between stimulants and modify its physical and functional response accordingly, although the mechanism behind this discernment is unclear.

We hypothesize that the physical and functional differences are related to the needs of the cell given the stimulus: if a cell senses a single molecule or low-density stimulus, it might need to increase motility both to heighten sensing and receptor-receptor interactions and to move to the source of that stimulus (i.e. a pathogen). Whereas if the cell senses a pathogen, it decreases motility and prepares energy for other functions like phagocytosis. Further research is required to determine if or which pieces of this hypothesis are correct, and microscopy is an ideal avenue

to continue to track the cellular behavior. For example, gradient-based microscopy with a transwell assay⁸ or microfluidic microscopy⁹ would help give a sense of directionality of TLR2-mediated macrophage motility and whether the cells migrate preferentially toward a ligand source or are especially responsive to chemotactic gradients that might be present in an *in vivo* environment. We are also currently working on LLSM tracking of unrelated, non-immune receptors (e.g. Sphingosine-1-Phosphate Receptor and CD45) to see if the physical behavior changes are on the whole-cell cell membrane level or are specific to TLR2.

In terms of microscopic tracking of PRRs themselves, there are also many future directions to build from our work. One limitation to our LLSM approach is a lack of single-molecule resolution. LLSM has no higher resolution than more conventional techniques; therefore, we were not able to confidently track single TLRs while they became activated. If we move to a super-resolution system ideal for fast tracking of single molecules (e.g. dSTORM¹⁰), we will be able to probe more specific questions about the nature of the TLR activity. For example, we could use a labeled single-molecule ligand and track differences between bound and unbound single receptors to understand how a receptor's biophysics changes upon ligation.

It would also be of considerable interest to develop labels for other PRRs and do twocolor super-resolution tracking of multiple PRRs in the same cell. In this way, we could
establish the physical nature of receptor synergy and crosstalk between PRRs. Prior work has
suggested that there is a physical component to receptor synergy and that synergy depends on the
organization of ligands in space¹¹. Using two-color tracking, we could use structured and
unstructured combinatorial stimuli that engage PRRs in synergistic ways and see how they colocalize with each other as part of that activity.

6.4 Biophysical Manipulation of Host-Pathogen Interactions

Our work using FluidFM to manipulate single bacterium-macrophage interactions is quite preliminary. Nonetheless, it highlights our ability to use FluidFM for high levels of characterization in innate immune biophysics. At best, stimulation of single macrophages by single bacteria has been carried out in microfluidic droplets¹⁷; however, this is, to our knowledge, the first study to exert such finely tuned control over host-pathogen interactions—where we can adjust number of contacts between the pathogen and the immune cell, the speed, frequency, and location of those contacts, and can do so on a single-pathogen level. Already our findings have shown the result that one *B. subtilis* is unable to activate a macrophage with 30 minutes of direct contact *in vitro*. This result seems unintuitive because pathogen detection is essential for clearance; however, it also highlights apparent mechanisms for macrophage temperance in the presence of low amounts of stimulation.

The mechanisms of this temperance and how it translates to *in vivo* contexts are unclear because most of our intuition of bacterium-macrophage interactions come from bulk stimulation experiments. Signal information is encoded to cells in terms of duration and strength, and it is known in adaptive immune cells that both contact time and ligand dose modulate the responses of these cells "—and even that weak, sustained signaling is a primary motivator for selection of these cells during development." Additionally, it has been shown that macrophages are not robust to weak signaling and that the probability of their activation is very sensitive at low ligand doses. and these responses are time delayed on the order of an hour or more, possibly as a protective measure against consistently strong immune responses. Further work, therefore, is warranted to determine whether there is a threshold of time at which a single *B. subtilis* does activate a macrophage, as it may be longer than the 30-minute trials we completed. If that is the

case, further research is also needed to determine what the long single-bacterium exposure times required to activate a macrophage mean *in vivo*. Our LLSM experiments show *B. subtilis* contacts with macrophages on the order of seconds or less when freely swimming with cells, and adaptive immune responses can be triggered by fewer than 100 ligand-receptor interactions in a matter of seconds¹⁵, so the relative difficulty of a single bacterium to activate a macrophage is striking. It might be that there are other contextual factors that help guide activation in a very metered way toward pathogens—from macrophage polarization to cell-cell interactions—that would be of interest to elucidate. We could, for example, supplement the macrophage medium with IFNγ while doing our single *B. subtilis* stimulations to see the effect conventional macrophage priming has on sensing ability to quantify the role of such signals for sensing in low stimulus environments.

Additionally, the manipulation of exposure biophysics in the innate immune response allows us to understand what physical parameters are most important for effective immune activation. Our studies were limited in this arm as we did not see robust activation from single bacteria; however, by using a stronger stimulus, we could characterize the innate immune response from a biophysical perspective. Bacterial motility in particular has been cited as important in pathogen sensing: studies have shown that highly motile bacteria are more likely to be phagocytosed. For example, using centrifugation to increase the collision speed of bacteria onto a bed of macrophages caused greater uptake of the bacteria 16 . Collision speeds in these experiments were as high as $2.5~\mu m/s$; however, this speed is much lower than that of a typical motile bacterium (~20-50 μ m/s). The FluidFM can increase collision speed much higher than centrifugation with lower risk of damage to the bacterium, so it is easier to study this phenomenon using our method.

The FluidFM's movement capability also allows us to simulate searching behaviors of motile bacteria. Studies have shown intuitively that bacterial infectivity is proportional to how many encounters with host cells they have and have modeled this phenomenon in terms of diffusivity of the bacterium¹⁸. Additional research has shown that *in vitro* bacteria typically make 1-3 contacts per minute with host cells that last less than 10 seconds¹⁹. It is straightforward with the FluidFM to model these parameters in a collection of macrophages to see how number of contacts and contact duration affect the macrophage response. In our preliminary tapping experiments, we simulated 10 second contacts to see if a single bacterium would activate the cell with typical motile-like behaviors given that motile bacteria are typically more phagocytosed. While we did not see activation in our experiments, it is possible we would see greater activation if we better simulated the biological environment by tapping the bacterium on different parts of the cell. Perhaps PRR ligation in multiple areas of the cell could lead to higher levels of activation; however, more research is needed to confirm this possibility.

Finally, we are interested in a recent hypothesis that the innate immune system is primed to sense pathogen material due to biochemical errors from the pathogen's perspective that might result in damage or aberrant stimulus exposure²⁰. If this were the case, we could use the FluidFM to assay activation due to intact versus chemically damaged bacteria to see if the increased ligand exposure due to bacterial damage does drive innate immunity. We have begun experimenting with the idea of antibiotic or alcohol treatments to disrupt bacteria; however, physical disruption might also be possible using the FluidFM probe tip or pressure, and more research is needed to determine the ideal approach.

All told, using the FluidFM to manipulate single host-pathogen interactions can afford unique opportunities to learn about optimal sensing in the innate immune system. One eventual

goal might be to drive therapeutic development with novel findings. For example, with our current results, we might consider development of a therapeutic that sticks bacteria together, so they are more immunogenic than single bacteria alone. In the future, if we determine how contact must occur between the pathogen and the macrophage for ideal activation, we might develop compounds that help to stimulate such an environment.

6.5 References

- 1. Hu, Y., Cong, X., Chen, L., Qi, J., Wu, X., Zhou, M., Yoo, D., Li, F., Sun, W., Wu, J., Zhao, X., Chen, Z., Yu, J., Du, Y., & Wang, J. (2016). Synergy of TLR3 and 7 ligands significantly enhances function of DCs to present inactivated PRRSV antigen through TRIF/MyD88-NF-κB signaling pathway. *Scientific reports*, *6*, 23977. https://doi.org/10.1038/srep23977
- 2. Ferwerda, G., Meyer-Wentrup, F., Kullberg, B. J., Netea, M. G., & Adema, G. J. (2008). Dectin-1 synergizes with TLR2 and TLR4 for cytokine production in human primary monocytes and macrophages. *Cellular microbiology*, *10*(10), 2058–2066. https://doi.org/10.1111/j.1462-5822.2008.01188.x
- 3. Temizoz, B., Hioki, K., Kobari, S., Jounai, N., Kusakabe, T., Lee, M. S. J., Coban, C., Kuroda, E., & Ishii, K. J. (2022). Anti-tumor immunity by transcriptional synergy between TLR9 and STING activation. *International immunology*, *34*(7), 353–364. https://doi.org/10.1093/intimm/dxac012
- 4. Root-Bernstein R. (2020). Synergistic Activation of Toll-Like and NOD Receptors by Complementary Antigens as Facilitators of Autoimmune Disease: Review, Model and Novel Predictions. *International journal of molecular sciences*, 21(13), 4645. https://doi.org/10.3390/ijms21134645
- 5. Netea, M. G., Domínguez-Andrés, J., Barreiro, L. B., Chavakis, T., Divangahi, M., Fuchs, E., Joosten, L. A. B., van der Meer, J. W. M., Mhlanga, M. M., Mulder, W. J. M., Riksen, N. P., Schlitzer, A., Schultze, J. L., Stabell Benn, C., Sun, J. C., Xavier, R. J., & Latz, E. (2020). Defining trained immunity and its role in health and disease. *Nature reviews. Immunology*, 20(6), 375–388. https://doi.org/10.1038/s41577-020-0285-6
- 6. Onyishi, C. U., Desanti, G. E., Wilkinson, A. L., Lara-Reyna, S., Frickel, E. M., Fejer, G., Christophe, O. D., Bryant, C. E., Mukhopadhyay, S., Gordon, S., & May, R. C. (2023). Toll-like receptor 4 and macrophage scavenger receptor 1 crosstalk regulates phagocytosis of a fungal pathogen. *Nature communications*, *14*(1), 4895. https://doi.org/10.1038/s41467-023-40635-w
- 7. Kim, J. Y., Rosenberger, M. G., Chen, S., Ip, C. K., Bahmani, A., Chen, Q., Shen, J., Tang, Y., Wang, A., Kenna, E., Son, M., Tay, S., Ferguson, A. L., & Esser-Kahn, A. P. (2023). Discovery of New States of Immunomodulation for Vaccine Adjuvants via High Throughput Screening: Expanding Innate Responses to PRRs. *ACS central science*, *9*(3), 427–439. https://doi.org/10.1021/acscentsci.2c01351
- 8. Justus, C. R., Marie, M. A., Sanderlin, E. J., & Yang, L. V. (2023). Transwell In Vitro Cell Migration and Invasion Assays. *Methods in molecular biology (Clifton, N.J.)*, 2644, 349–359. https://doi.org/10.1007/978-1-0716-3052-5_22
- 9. Samandari, M., Rafiee, L., Alipanah, F., Sanati-Nezhad, A., & Javanmard, S. H. (2021). A simple, low cost and reusable microfluidic gradient strategy and its application in modeling cancer invasion. *Scientific reports*, *11*(1), 10310. https://doi.org/10.1038/s41598-021-89635-0

- 10. Endesfelder, U., & Heilemann, M. (2015). Direct stochastic optical reconstruction microscopy (dSTORM). *Methods in molecular biology (Clifton, N.J.)*, *1251*, 263–276. https://doi.org/10.1007/978-1-4939-2080-8_14
- 11. Li, W., Li, M., Anthony, S. M., & Yu, Y. (2021). Spatial organization of FcγR and TLR2/1 on phagosome membranes differentially regulates their synergistic and inhibitory receptor crosstalk. *Scientific reports*, *11*(1), 13430. https://doi.org/10.1038/s41598-021-92910-9
- 12. Miskov-Zivanov, N., Turner, M. S., Kane, L. P., Morel, P. A., & Faeder, J. R. (2013). The duration of T cell stimulation is a critical determinant of cell fate and plasticity. *Science signaling*, 6(300), ra97. https://doi.org/10.1126/scisignal.2004217
- 13. Iezzi, G., Karjalainen, K., & Lanzavecchia, A. (1998). The duration of antigenic stimulation determines the fate of naive and effector T cells. *Immunity*, 8(1), 89–95. https://doi.org/10.1016/s1074-7613(00)80461-6
- 14. Kellogg, R. A., Tian, C., Lipniacki, T., Quake, S. R., & Tay, S. (2015). Digital signaling decouples activation probability and population heterogeneity. *eLife*, *4*, e08931. https://doi.org/10.7554/eLife.08931
- 15. Altan-Bonnet, G., & Germain, R. N. (2005). Modeling T cell antigen discrimination based on feedback control of digital ERK responses. *PLoS biology*, *3*(11), e356. https://doi.org/10.1371/journal.pbio.0030356
- 16. Tomita, T., & Kanegasaki, S. (1982). Enhanced phagocytic response of macrophages to bacteria by physical impact caused by bacterial motility or centrifugation. *Infection and immunity*, *38*(3), 865–870. https://doi.org/10.1128/iai.38.3.865-870.1982
- 17. Jiang, Z., Liu, S., Xiao, X., Jiang, G., Qu, Q., Miao, X., Wu, R., Shi, R., Guo, R., & Liu, J. (2022). High-throughput probing macrophage-bacteria interactions at the single cell level with microdroplets. *Lab on a chip*, 22(16), 2944–2953. https://doi.org/10.1039/d2lc00516f
- 18. Otte, S., Ipiña, E. P., Pontier-Bres, R., Czerucka, D., & Peruani, F. (2021). Statistics of pathogenic bacteria in the search of host cells. Nature communications, 12(1), 1990. https://doi.org/10.1038/s41467-021-22156-6
- 19. Achouri, S., Wright, J. A., Evans, L., Macleod, C., Fraser, G., Cicuta, P., & Bryant, C. E. (2015). The frequency and duration of Salmonella-macrophage adhesion events determines infection efficiency. *Philosophical transactions of the Royal Society of London. Series B, Biological sciences*, *370*(1661), 20140033. https://doi.org/10.1098/rstb.2014.0033
- 20. Kagan J. C. (2023). Infection infidelities drive innate immunity. *Science (New York, N.Y.)*, 379(6630), 333–335. https://doi.org/10.1126/science.ade9733

APPENDIX: SUPPLEMENTAL DATA

A.2 Data Supporting Chapter 2

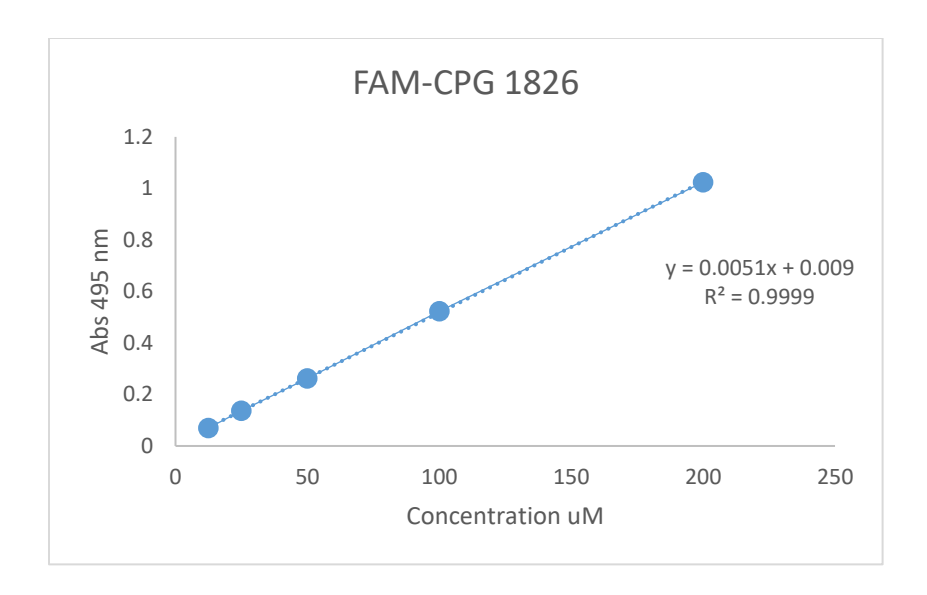


Figure A.2.1. Standard curve to quantify CPG dimers relative to FAM absorbance at 495 nm.

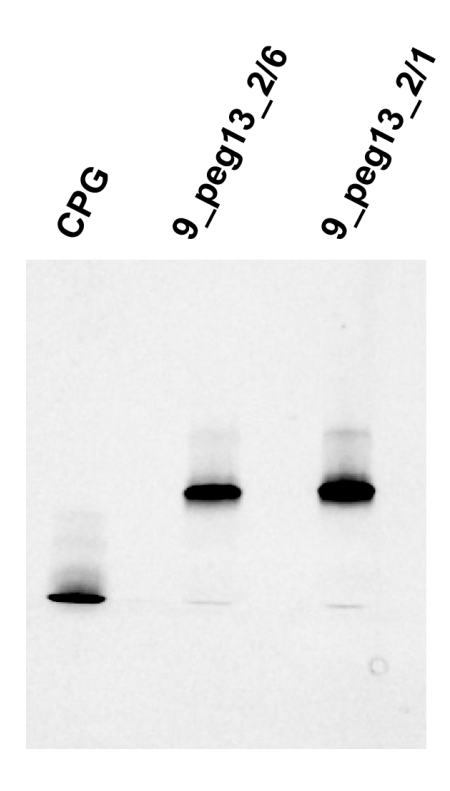


Figure A.2.2. Gel electrophoresis of FAM labeled CpG_1826, and FAM labeled Pam_PEG ₁₃ _CpG compounds visualized by 6 fluorescein amidite tag (495 nm laser excitation).

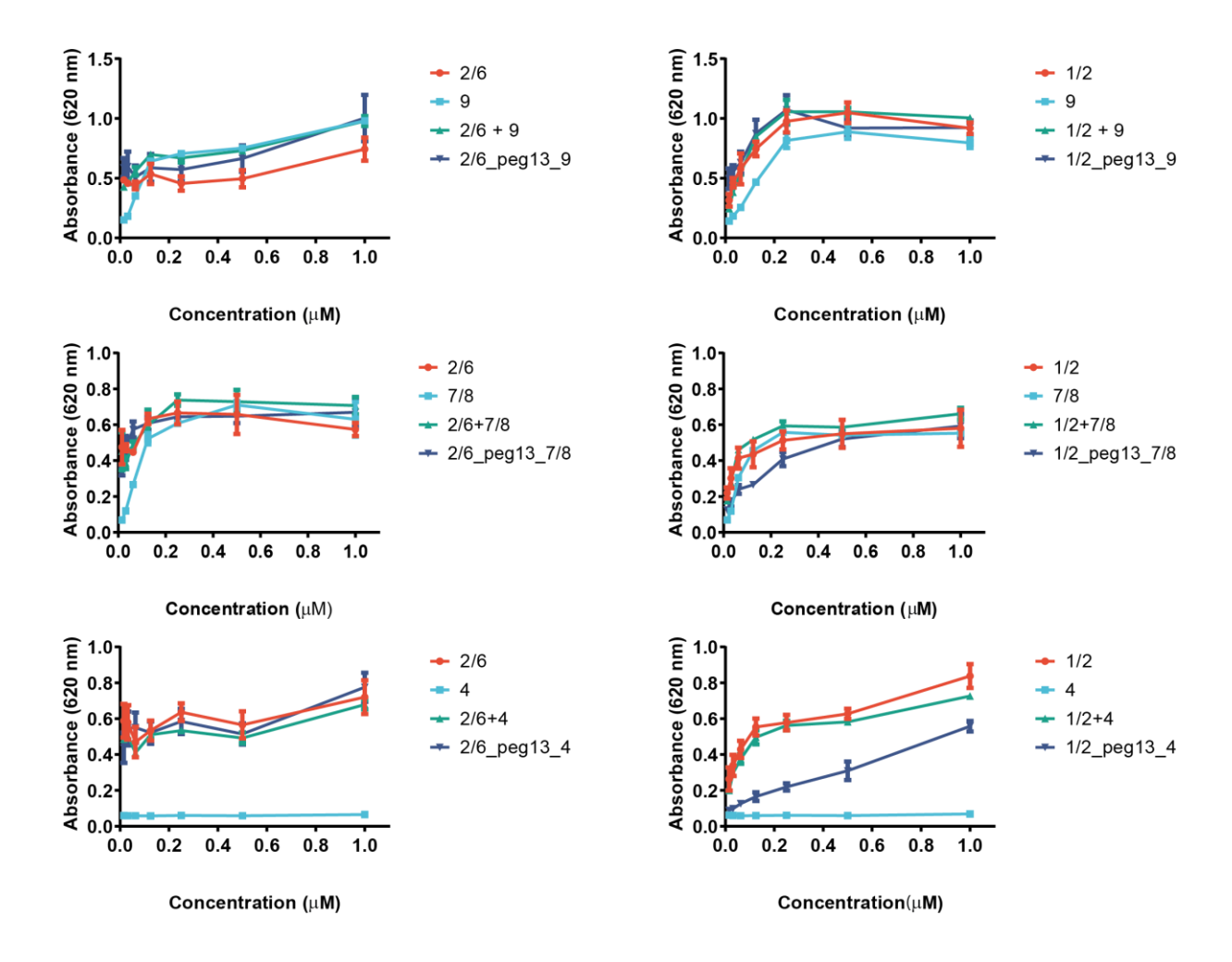


Figure A.2.3. Concentration scan of Pam2CSK4 (2/6), Pam3CSK4 (2/1), CpG_1826 (9) indole (4) and imidazoquinoline (7/8), corresponding equimolar mixtures and linked agonists measured by RAW-Blue activation after 24 h incubation at 37 °C.

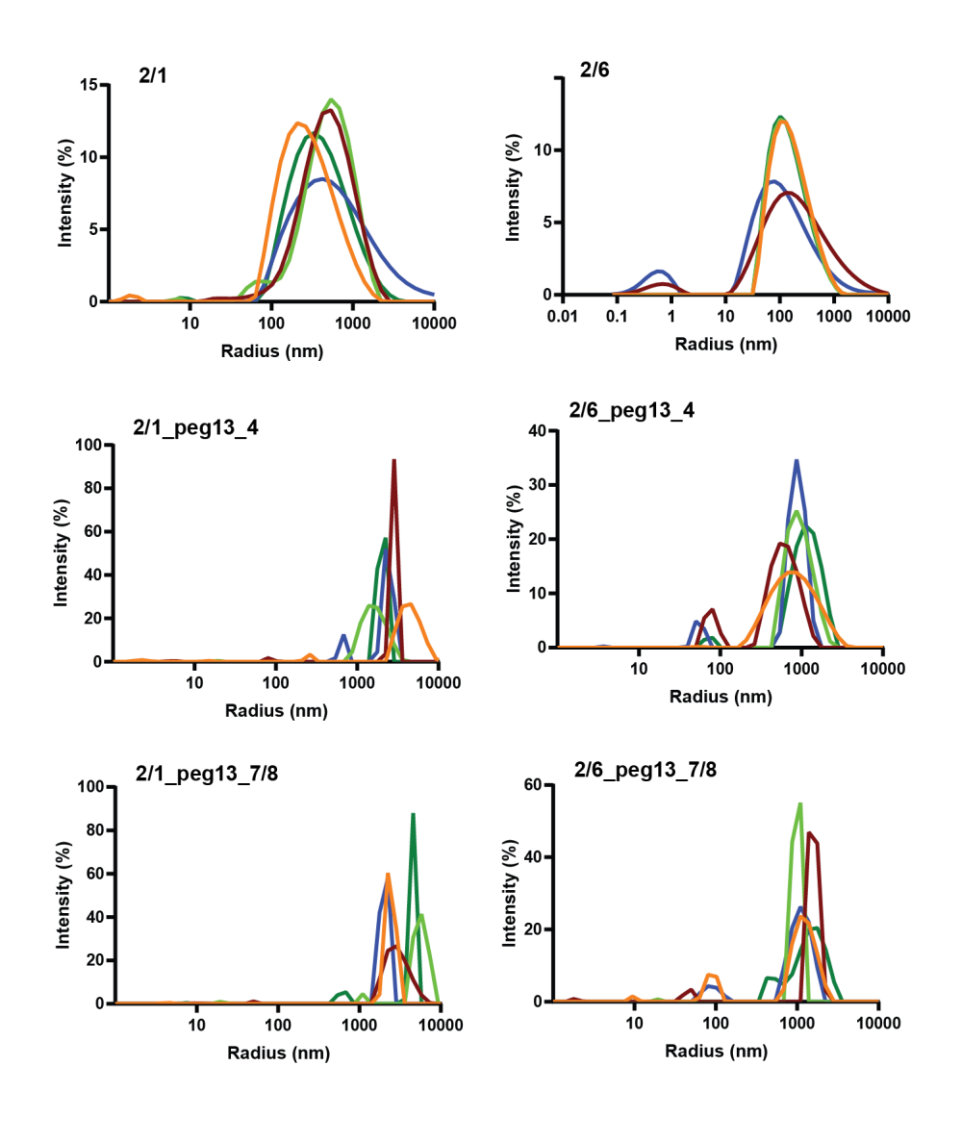


Figure A.2.4. Intensity vs particle size of lipopeptide and lipopeptide derive dimers measured by dynamic light scattering (DLS). Samples measured at 250 nM in PBS.

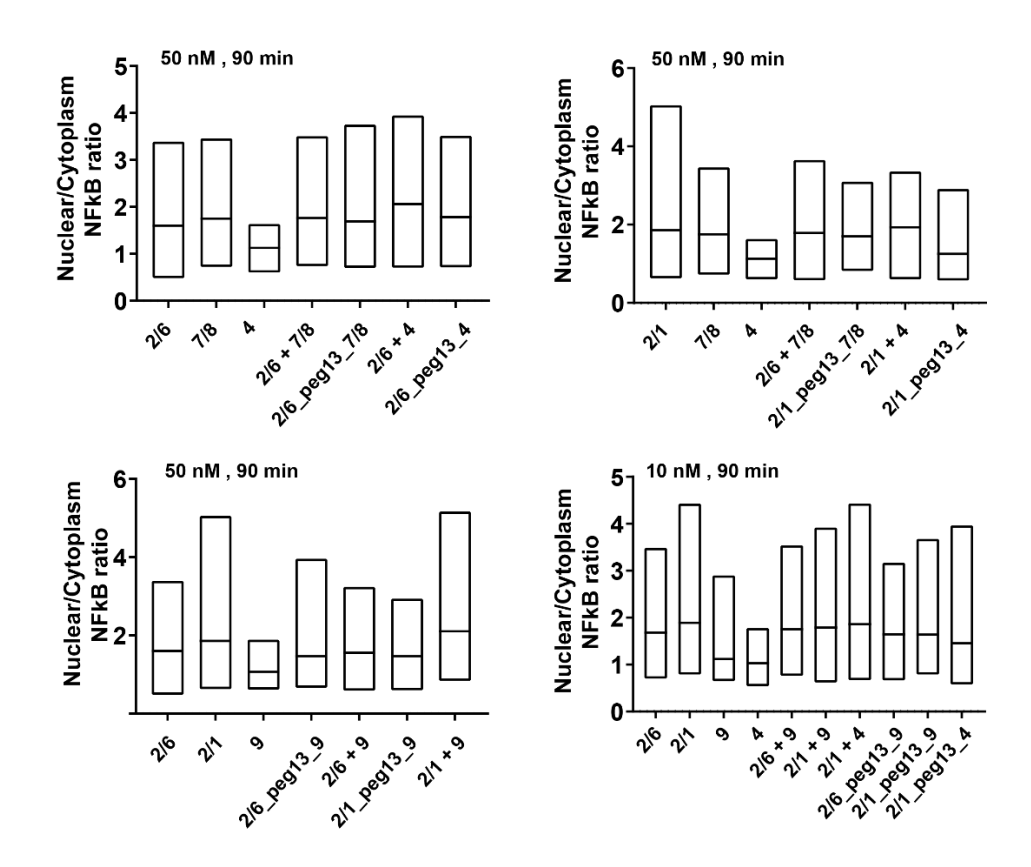


Figure A.2.5. Box graph showing distribution of single cells based on the nuclear/cytoplasm NF κ B ratio. Line representing mean.

A.4 Data Supporting Chapter 4

Track Parameter	Description		
Average Track Speed (um/s)	The average speed measured from all track segments		
Average, Track Speed (µm/s)	that make up the track		
Max, Track Speed (μm/s)	The highest speed measured from the track		
Max, Hack Speed (μπ/s)	segments that make up the track		
Min, Track Speed (μm/s)	The lowest speed measured from the track segments		
Mill, Track Speed (μπ/s)	that make up the track		
Length (max), Track Length (µm)	The highest distance traveled by a track segment in		
Length (max), frack Length (μm)	the track		
Length (sum), Track Length (μm)	The total length of all track segments in a track		
Area, 2D Oriented Bounds (µm²)	The area of a box projected onto the longest and		
	shortest dimension of motion of the track		
Side Ratio, 2D Oriented Bounds			
-	The ratio of the two side lengths for the above box		
Total Displacement,	The average of the squared distance traveled by all		
Track Mean Squared Displacement (µm²)	track segments		
X Displacement,	X-component of mean squared displacement		
Track Mean Squared Displacement (µm²)	A component of mean squared displacement		
Y Displacement,	Y-component of mean squared displacement		
Track Mean Squared Displacement (µm²)			
Z Displacement,	Z-component of mean squared displacement		
Track Mean Squared Displacement (µm²)			
# Fusions, Track Lineage (advanced)	Number of times another segment was added to the		
- accord, react integral (automobile)	track via fusion onto the primary track		
# Children	The total number of tracked blobs that make up the		
Gilliaicii	track		
Length (min), Track Length (μm)	The lowest distance traveled by a track segment in		
	the track		
Straightness (max), Track Straightness	Calculated (max displacement/max length) for the		
, , , , , , , , , , , , , , , , , , ,	track		
Straightness (min), Track Straightness	Calculated (min displacement/min length) for the		
J = === (,, === == -g-====	track		

Table A.4.1. List of tracked parameters for TLR2.

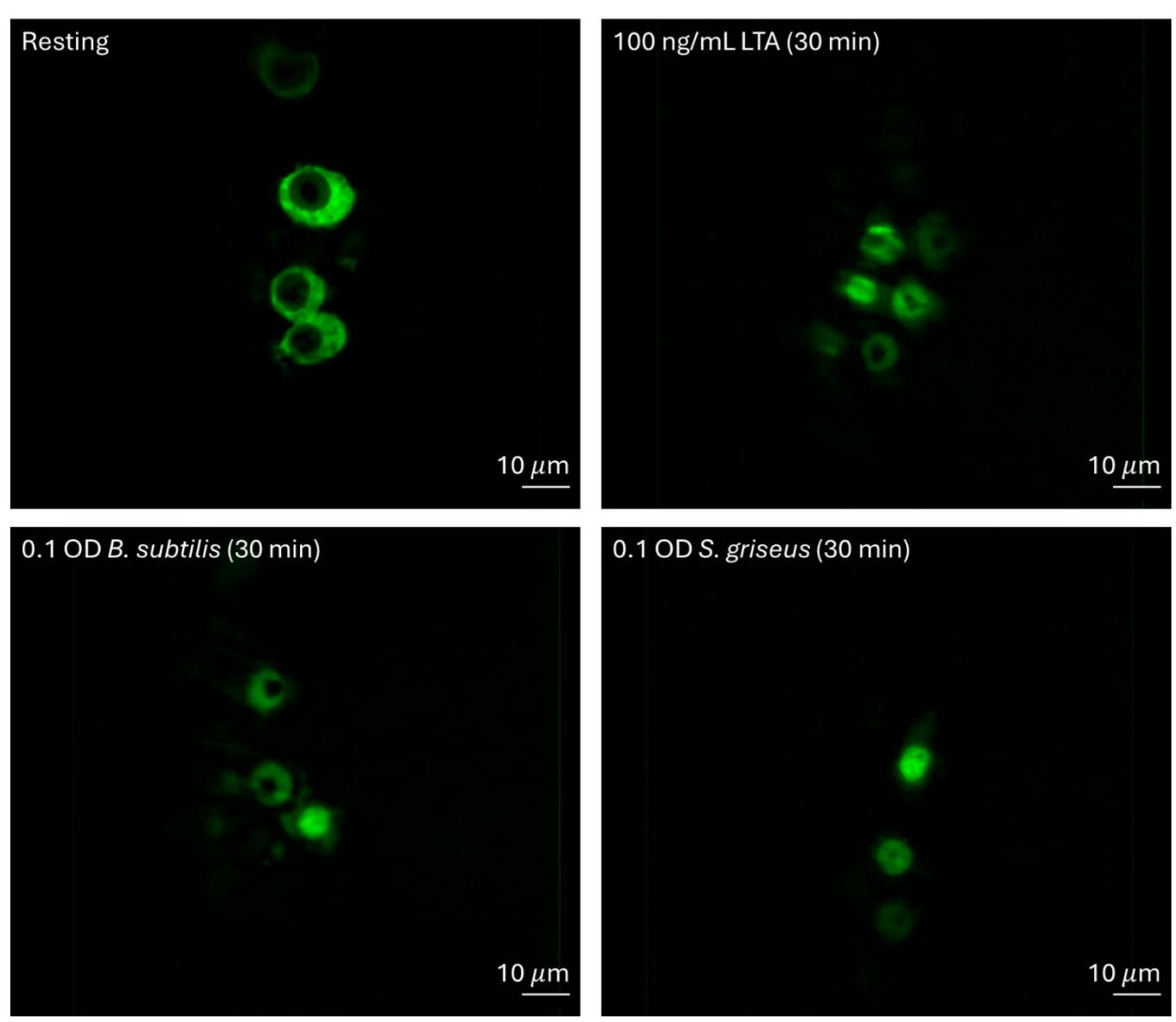


Figure A.4.1. Stimulation of RAW G9 macrophages on the LLSM. Cells were incubated with the indicated stimulus for 30 minutes, and activation caused fluorescently tagged NFκB to migrate to the nucleus.

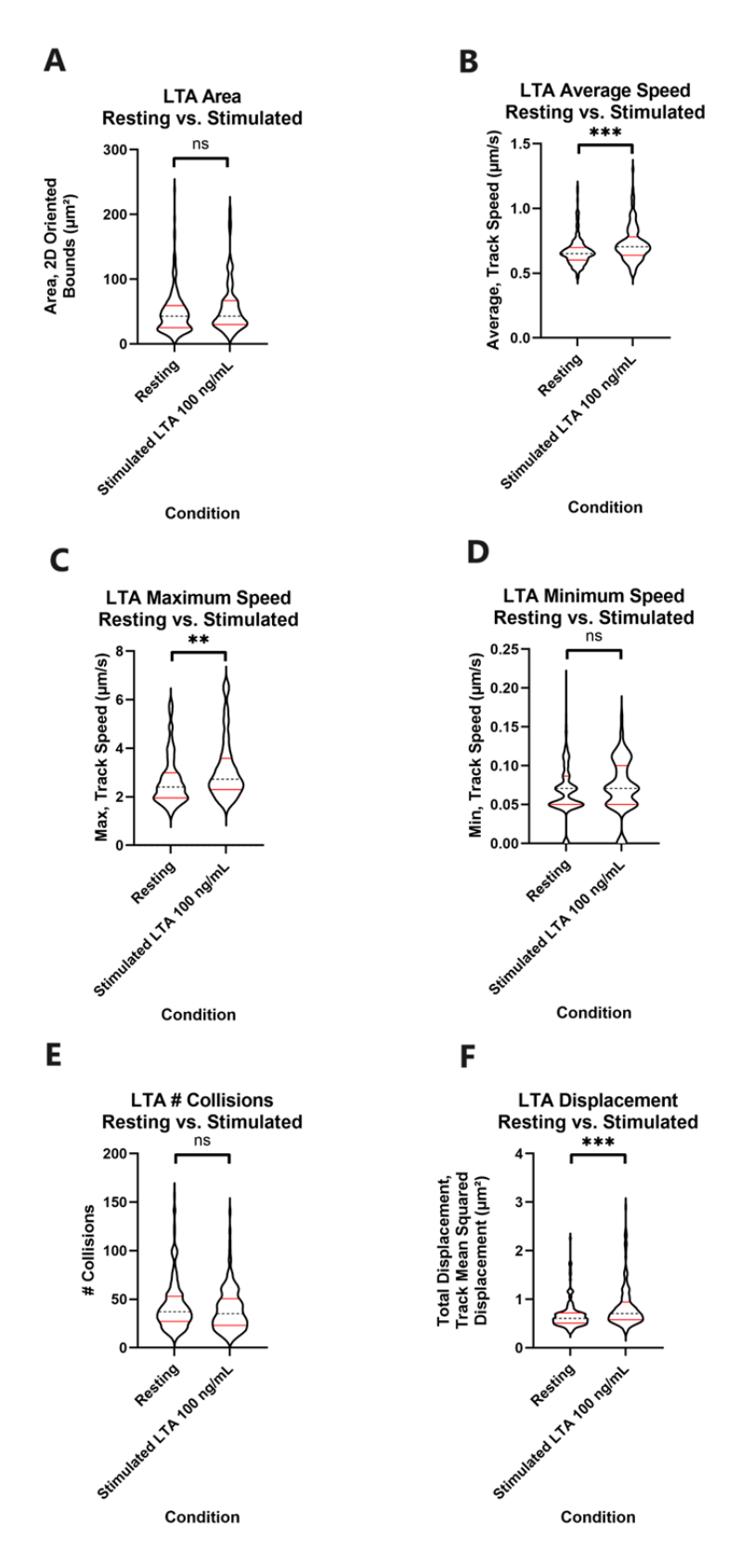


Figure A.4.2. Full distribution of LTA resting vs. stimulated data. Means compared with a two-tailed t-test. NS p > 0.05, ** p < 0.01, *** p < 0.001

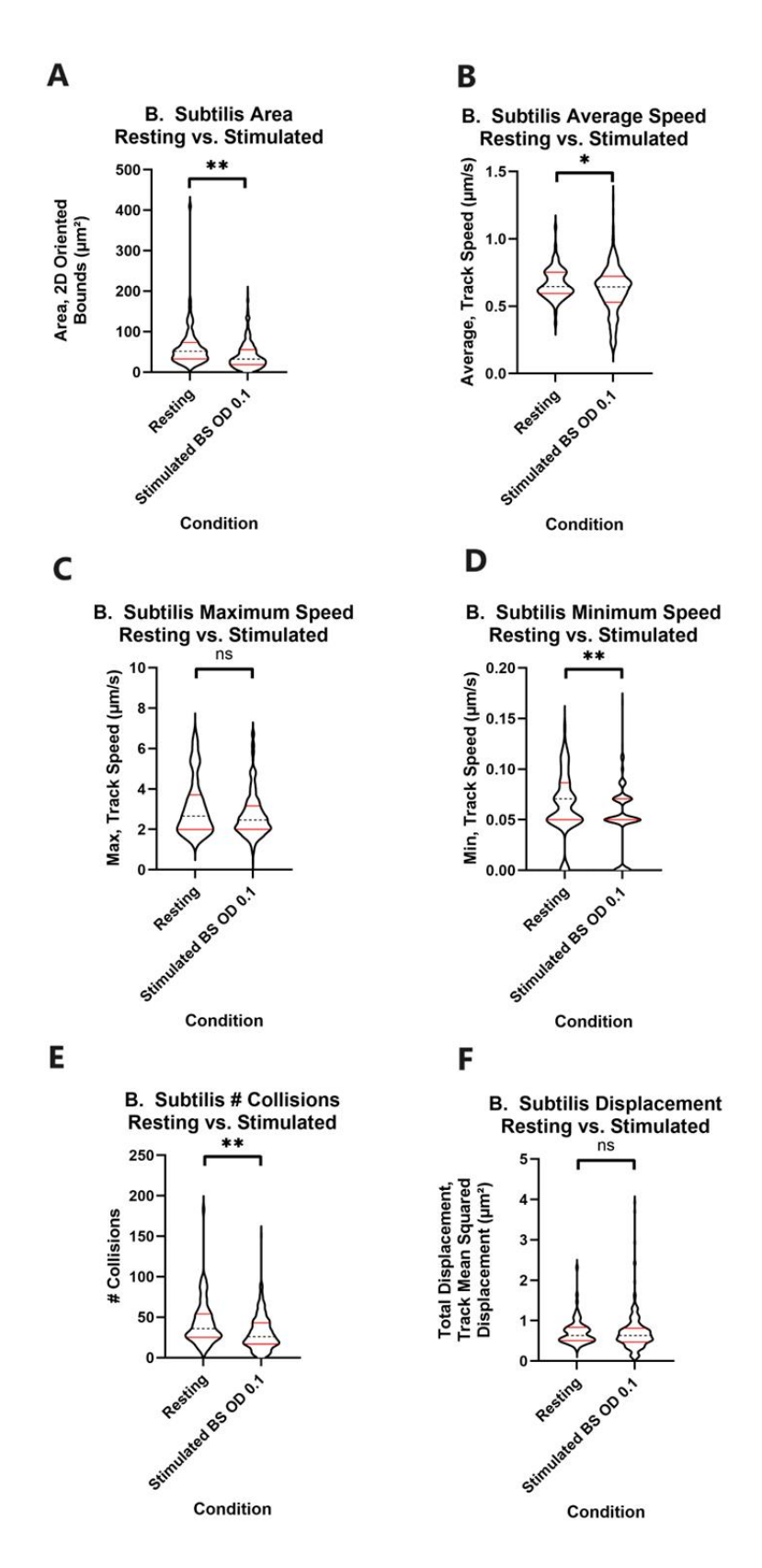


Figure A.4.3. Full distribution of *B. subtilis* resting vs. stimulated data. Means compared with a two-tailed t-test. NS p > 0.05, * p < 0.05, ** p < 0.01

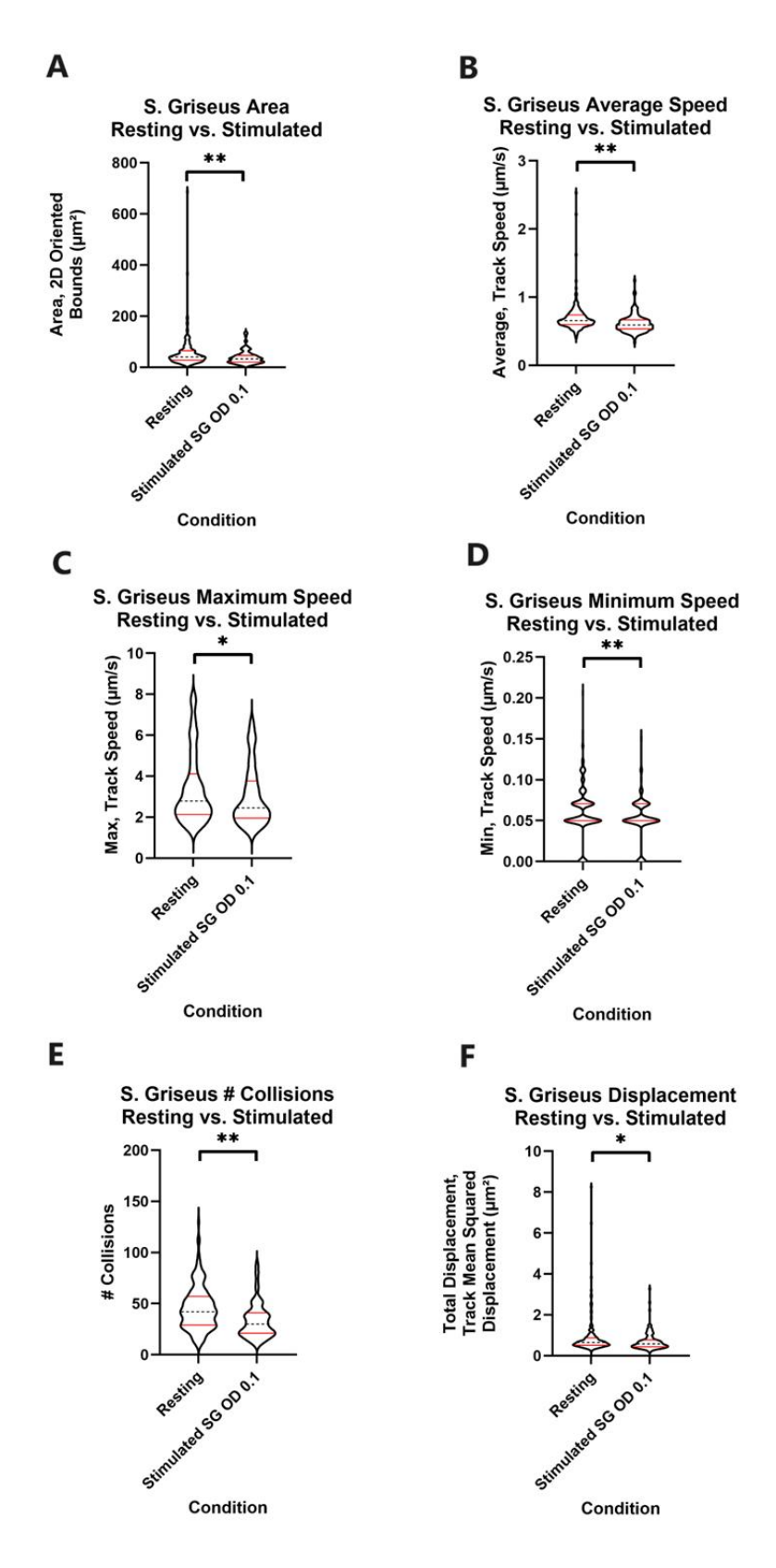


Figure A.4.4. Full distribution of *S. griseus* resting vs. stimulated data. Means compared with a two-tailed t-test. NS p > 0.05, * p < 0.05, ** p < 0.01, *** p < 0.001

Track Parameter	T-Test P- value	BH- Adjusted P-Value	Significance
Y Displacement, Track Mean Squared Displacement (µm²)	0.09522369	0.3792473	NS
Total Displacement, Track Mean Squared Displacement (µm²)	0.09805082	0.3792473	NS
Average, Track Speed (µm/s)	0.09875103	0.3792473	NS
Max, Track Speed (µm/s)	0.13470682	0.3792473	NS
Area, 2D Oriented Bounds (μm²)	0.13846319	0.3792473	NS
X Displacement, Track Mean Squared Displacement (μm²)	0.14221772	0.3792473	NS
Length (max), Track Length (μm)	0.1781235	0.4071394	NS
Straightness (max), Track Straightness	0.26489926	0.5297985	NS
Min, Track Speed (μm/s)	0.32405564	0.5467727	NS
Length (sum), Track Length (μm)	0.3496077	0.5467727	NS
# Fusions, Track Lineage (advanced)	0.37590622	0.5467727	NS
Straightness (min), Track Straightness	0.48600832	0.6480111	NS
Z Displacement, Track Mean Squared Displacement (µm²)	0.55457746	0.6825569	NS
Length (min), Track Length (μm)	0.76789866	0.8215822	NS
# Children	0.77023329	0.8215822	NS
Side Ratio, 2D Oriented Bounds	0.89609988	0.8960999	NS

Table A.4.2. Comparison of track parameters for tracks touching *B. subtilis* and those that do not. A "touching track" was defined as a track that contacts *B. subtilis* during the imaging time. Mean parameter values for those tracks were compared to mean values for all non-touching tracks in the same videos.

Track Parameter	T-Test P- value	BH- Adjusted P-Value	Significance
Average, Track Speed (μm/s)	0.07806482	0.5112069	NS
Length (max), Track Length (μm)	0.09195983	0.5112069	NS
Length (sum), Track Length (μm)	0.1819148	0.5112069	NS
Area, 2D Oriented Bounds (μm²)	0.22313719	0.5112069	NS
X Displacement, Track Mean Squared Displacement (μm²)	0.23796782	0.5112069	NS
Max, Track Speed (μm/s)	0.23848891	0.5112069	NS
Total Displacement, Track Mean Squared Displacement (µm²)	0.24562231	0.5112069	NS
# Fusions, Track Lineage (advanced)	0.32097736	0.5112069	NS
Y Displacement, Track Mean Squared Displacement (μm²)	0.32857042	0.5112069	NS
# Children	0.33488493	0.5112069	NS
Length (min), Track Length (μm)	0.37851323	0.5112069	NS
Min, Track Speed (μm/s)	0.38340519	0.5112069	NS
Straightness (max), Track Straightness	0.45331548	0.5388105	NS
Z Displacement, Track Mean Squared Displacement (µm²)	0.4714592	0.5388105	NS
Side Ratio, 2D Oriented Bounds	0.5994319	0.639394	NS
Straightness (min), Track Straightness	0.77104954	0.7710495	NS

Table A.4.3. Comparison of track parameters for tracks touching *S. griseus* and those that do not. A "touching track" was defined as a track that contacts *S. griseus* during the imaging time. Mean parameter values for those tracks were compared to mean values for all non-touching tracks in the same videos.